EUSKAL HERRIKO UNIBERTSITATEA

UNIVERSIDAD DEL PAÍS VASCO

MATERIAL AURRERATUAK: FISIKA, KIMIKA ETA TEKNOLOGIA SAILA

DEPARTAMENTO DE POLÍMEROS Y MATERIALES AVANZADOS: FÍSICA, QUÍMICA Y TECNOLOGÍA

Infrared nanoimaging and nanospectroscopy in liquid environment

PhD thesis within the doctoral program of

Physics of nanostructures and advanced materials

submitted by

Divya Virmani

under the supervision of

Prof. Dr. Rainer Hillenbrand

Donostia - San Sebastián, 2024

Infrared nanoimaging and nanospectroscopy in liquid environment

This PhD thesis has been carried out by

Divya Virmani

at

CIC nanoGUNE BRTA, San Sebastián, Spain

under the supervision of

Prof. Dr. Rainer Hillenbrand

Contents

1. Resumen

La espectroscopia Infrarroja de Transformada de Fourier (FTIR) es una de las herramientas analíticas que más se utiliza para la caracterización de todo tipo de materiales. La absorción infrarroja es una característica específica de la composición química y de la estructura de un material, y por este motivo, se emplea para la identificación y la caracterización inequívoca de la estructura de los materiales tanto en investigación como en aplicaciones industriales [1–5]. Sin embargo, como la mayoría de técnicas ópticas, la resolución espacial de la espectroscopia infrarroja (IR) está limitada por el límite de difracción alrededor de $\lambda/2$, en el caso de la luz IR, a escala micrométrica [6]. Esta limitación hace que las técnicas IR convencionales no sean adecuadas para la caracterización de objetos a escala nanométrica, los cuales son cruciales en muchas aplicaciones científicas modernas.

La microscopía óptica de barrido de campo cercano de tipo dispersivo (del inglés, scattering-type Scanning Near-Field Optical Microscopy, s-SNOM) [7–9] es una técnica bien establecida basada en la microscopía de fuerza atómica (AFM) que supera el límite de difracción, lo que permite obtener imágenes y espectros con resolución nanométrica en un amplio rango espectral, desde las frecuencias visibles hasta las sub-THz [10–12]. En el s-SNOM, una punta metálica de AFM se ilumina con un haz de luz monocromática. La punta actúa como una antena y focaliza la luz incidente generando una fuerte interacción óptica de campo cercano altamente confinada en su ápice. La extensión del campo cercano en el ápice de la punta determina la resolución espacial en el s-SNOM, que suele ser del orden del radio de la punta del ápice $R = 25\,\mathrm{nm}$ [13]. Al interactuar con la muestra, debido a las propiedades dieléctricas locales de la misma, el campo cercano generado modifica la luz dispersada. Esta luz dispersada por la punta se recoge mediante un sistema de detección interferométrico que permite la medición simultánea de la amplitud y la fase del campo disperso y, en última instancia, la reconstrucción de las propiedades dieléctricas locales de la muestra [14, 15]. Gracias a ello, es posible generar una imagen infrarroja de la muestra con resolución a escala nanométrica registrando la luz dispersada por la punta en función de su posición. También es posible, registrar un espectro infrarrojo por transformada de Fourier con resolución a escala nanométrica (nano-FTIR) de la muestra [16, 17] iluminando la punta del AFM con un láser infrarrojo de banda ancha y registrando la luz dispersada por la punta en función de la posición del espejo de referencia en una ubicación fija de la muestra (interferograma). Los

rangos espectrales de la muestra pueden obtenerse aplicando una transformada de Fourier al interferograma y normalizándolo posteriormente con respecto a un espectro de referencia registrado en una zona espectralmente plana de la muestra, como una superficie limpia de Si o Au.

Tanto el s-SNOM como el nano-FTIR son potentes técnicas ópticas que permiten la caracterización a escala nanométrica de diversos materiales en un amplio rango espectral. Estas técnicas se han aplicado ampliamente para la caracterización química de muestras orgánicas e inorgánicas [16,18–20], identificar la estructura secundaria de las proteínas [21,22], medidas de conductividad local [23,24], identificar el campo electromagnético cercano de nanoestructuras plasmónicas [25–29] y visualizar la propagación de polaritones plasmónicos y fonónicos en materiales 2D [30–34]. Por el momento, la mayoría de estas aplicaciones se han demostrado principalmente en el aire.

Sin embargo, cada vez es más necesario obtener imágenes y realizar espectroscopia infrarroja a escala nanométrica en entornos líquidos, especialmente en el estudio de muestras bioquímicas y sistemas polaritónicos. La fuerte absorción de luz IR por parte de los líquidos, en particular del agua (H_2O), y las dificultades para mantener estable el funcionamiento del AFM en modo de contacto intermitente o " tapping" en líquido, han supuesto importantes desafíos al desarrollo del s-SNOM y el nano-FTIR para el estudio de muestras totalmente sumergidas en líquidos. Para superar estos retos, los esfuerzos iniciales para aplicar el s-SNOM en el rango del IR medio a muestras en entornos líquidos, involucraron el uso de celdas líquidas delgadas basadas en membranas transparentes al IR. En este enfoque, las muestras, junto con el líquido, se encapsulan dentro de una membrana, como el nitruro de silicio (SiN), mientras que el s-SNOM opera en aire [35–40].

De forma alternativa y paralela al trabajo presentado en esta tesis, se han utilizado otros enfoques novedosos para el funcionamiento de s-SNOM en líquido, en los que tanto la punta de campo cercano como las muestras, están totalmente sumergidas en líquido [41,42]. Esta técnica permite obtener imágenes de las muestras sin necesidad de una preparación tan exhaustiva de las mismas y así mismo evita el escaneo de la muestra a través de la membrana que la cubre, lo que afecta a la resolución espacial. Sin embargo y a pesar de estos avances, las técnicas descritas aún no están bien establecidas y presentan diversos retos técnicos y científicos.

El objetivo principal de esta tesis fue desarrollar e implementar la instrumentación necesaria para hacer posible la nanoimagen y la espectroscopia nano-FTIR basadas en s-SNOM del IR medio en entornos líquidos. Para ello, centramos nuestra atención principalmente en el desarrollo de técnicas de instrumentación para el mapeo s-SNOM in situ y la nanoespectroscopía de polaritones. Los polaritones pueden potenciar las interacciones entre la luz y la materia, y desempeñan un papel crucial en el análisis

óptico de alta sensibilidad de sustancias y procesos (bio)químicos. La nanoimagen y la espectroscopia de los campos evanescentes de los polaritones son esenciales para identificar modos experimentalmente y para estudiar el confinamiento de campos.

Para ello, hemos desarrollado dos configuraciones de s-SNOM que funcionan con rayos gaussianos estándar en los que tanto la punta de AFM como la muestra están totalmente sumergidas en líquido. Este trabajo constituye un primer paso fundamental para llevar a cabo estudios a escala nanométrica utilizando el s-SNOM y el nano-FTIR, y allana el camino para una serie de aplicaciones, incluyendo estudios in situ de espectroscopia molecular mejorada por antenas, el acoplamiento fuerte ("strong coupling") entre polaritones y vibraciones moleculares o reacciones químicas en la superficie de materiales polaritónicos, ya sean naturales o funcionalizados.

Esta tesis está organizada de la siguiente manera:

En el Capítulo 2, se presenta un resumen de esta tesis en inglés.

En el Capítulo 3 se ofrece una breve introducción a los conceptos fundamentales del s-SNOM y de le espectroscopia nano-FTIR. Para ello, en primer lugar, se exponen los principios fundamentales del AFM, que sirven de base para el s-SNOM. Después se proporciona una descripción detallada del principio de funcionamiento del s-SNOM y de las estrategias para reducir el ruido de fondo, necesarias para aislar las señales de campo cercano de la luz dispersada por la punta. Además, se analizan los esquemas de detección interferométrica empleados en el s-SNOM para obtener nanoimágenes infrarrojas y nanoespectroscopía con resolución tanto de amplitud como de fase. Por último, se ofrece una visión general de un montaje experimental de s-SNOM y nano-FTIR, que sirve de base para el montaje experimental desarrollado en esta tesis.

En el Capítulo 4, se describe detalladamente el desarrollo e implementación de dos montajes experimentales innovadores que permiten obtener imágenes IR con el s-SNOM y realizar espectroscopia nano-FTIR de muestras en un entorno líquido. La iluminación lateral y el esquema de recolección de la luz empleados en experimentos s-SNOM típicos [13] no son adecuados para su uso en líquidos debido a la fuerte absorción de la radiación infrarroja por éstos, especialmente en el caso del H_2O. En este capítulo se presenta un esquema de iluminación y captación que minimiza la absorción de luz infrarroja en el líquido (véase la Figura 1.1). En la primera implementación, el haz incidente es normal a la punta (s-SNOM en transflección) y la luz retrodispersada se capta mediante un esquema de detección interferométrica. La geometría de transflectancia es una configuración ideal para el mapeo y la caracterización de polaritones de plasmón localizado en antenas metálicas tanto en aire como en líquidos. En la segunda implementación, la punta se ilumina con la luz que se refleja totalmente en el interior de una cuña de $ZnSe$ (s-SNOM basado en TIR (Reflexión Total Interna), véase la Figura 1.3). La luz retrodispersada se detecta interferométricamente como en el s-SNOM de

transflección. La configuración s-SNOM basada en TIR se ha aplicado para el mapeo e identificación química infrarroja a escala nanométrica en el aire y en un entorno líquido. Estos avances mejoran significativamente la capacidad del s-SNOM y del nano-FTIR para la caracterización in situ de materiales, abriendo nuevas vías para el estudio de procesos bioquímicos y la detección molecular en líquidos.

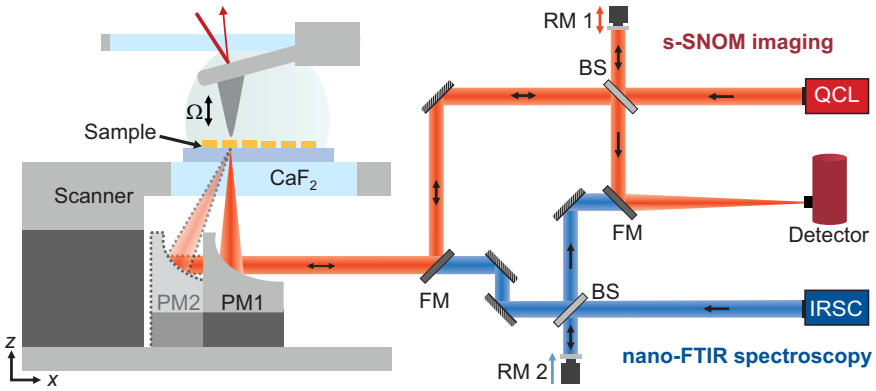

Figura 1.1.: **Representación esquemática del esquema de iluminación y detección de señal de fondo para nanoimagen IR s-SNOM (rojo) y nanoespectroscopia (azul) en líquidos.** Representación de los dos esquemas de iluminación y detección diseñados para s-SNOM con resolución de amplitud y fase (rojo) y nano-FTIR (azul) en medio líquido. En el primer esquema, la muestra se ilumina desde una fuente monocromática (rojo) o de banda ancha (azul) bajo incidencia normal mediante un espejo parabólico (PM1). En el segundo esquema, la muestra se ilumina con luz reflejada internamente desde una cuña de ZnSe (no mostrada aquí, ver Figura 1.3) con una fuente monocromática (roja) o de banda ancha (azul) utilizando un segundo espejo parabólico (PM2). BS: "Beam Splitter" o divisor de haz; FM: espejo giratorio; RM1: espejo vibratorio accionado por un piezo; RM2: QCL: láser de cascada cuántica sintonizable en frecuencia; IRSC: Láser Infrarrojo supercontinuo de banda ancha.

En el Capítulo 5, se aplica la configuración nano-FTIR de incidencia normal transflectiva a la espectroscopia infrarroja de antenas metálicas resonantes, tanto en aire como en líquidos. La obtención de imágenes y espectros de campos cercanos de las antenas a escala nanométrica en líquidos proporciona información clave para el diseño y la optimización de antenas metálicas infrarrojas y abre el camino para futuras aplicaciones en la detección molecular in situ. En el nano-FTIR de transmisión, una punta metálica de AFM se ilumina a través de los campos cercanos de la antena, y la luz retrodispersada de la antena se registra con un espectrómetro FTIR asimétrico. En la Figura 1.2 muestra un esquema del proceso de la iluminación de la punta. Este capítulo presenta una

metodología confiable para adquirir, referenciar y agrupar espectros nano-FTIR de transflección de antenas metálicas individuales tanto en aire como en líquido. En la Figura 1.2b se muestra un espectro de amplitud de transflección normalizado $s_3(\omega)$ de una antena de varilla metálica individual en aire (rojo) y en H_2O (azul). El impacto del H_2O en la resonancia de la antena puede verse claramente. Este trabajo establece una base fundamental para futuros estudios de nano-FTIR en transflección, enfocándose en la detección bio(química) mejorada por antenas, interacciones químicas y experimentos de acoplamiento vibracional fuerte.

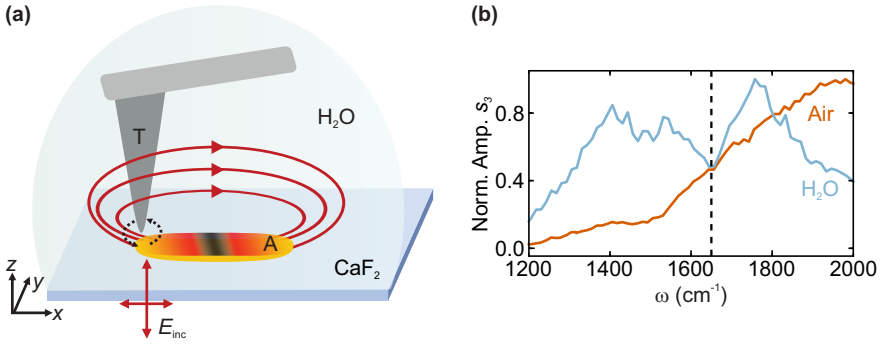

Figura 1.2.: **Imágenes de s-SNOM de transflección y espectroscopia nano-FTIR de nanoestructuras metálicas infrarrojas.** (a) Ilustración del proceso de dispersión de campo cercano. El campo incidente E_{inc} ilumina la antena (A). Los campos de la antena iluminan y polarizan la punta del AFM (T), que dispersa los campos cercanos a través de la antena hacia el campo lejano, donde se detecta mediante un esquema de detección interferométrica (no mostrado aquí). (b) Espectros de amplitud normalizados $s_3(\omega)$ de una antena de varilla metálica individual en aire (rojo) y en un entorno líquido (H_2O ; azul).

En Capítulo 6, se aplica la configuración s-SNOM basada en TIR para escanear polaritones de fonones ultraconfinados (PhPs) en láminas de nitruro de boro hexagonal (h-BN) en aire y en líquido. El mapeo de polaritones de fonones infrarrojos ultraconfinados en h-BN en un entorno líquido ofrece nuevas posibilidades para aprovechar las propiedades de los polaritones en dispositivos ultracompactos y altamente sensibles para la detección biomolecular en solución. La Figura 1.3a presenta el esquema de iluminación basado en TIR, en el que la punta metalizada del AFM se ilumina con la luz que se refleja totalmente en la superficie superior de una cuña de ZnSe. La punta se utiliza tanto para lanzar como para sondear los PhP. La nanoimagen (véase el recuadro de la Figura 1.3b) y la nanoespectroscopia de polaritones de fonones de h-BN ultraconfinados en líquido revelan que la presencia de líquido desplaza la dispersión de PhP a momentos más altos. En la Figura 1.3b se muestra una comparación de las dispersiones de PhP en aire

y en líquido. Este trabajo sienta las bases para futuros estudios s-SNOM y nano-FTIR mejorados por polaritones aplicables a una amplia gama de áreas, desde el estudio de interacciones bioquímicas hasta experimentos de acoplamiento fuerte en entornos líquidos.

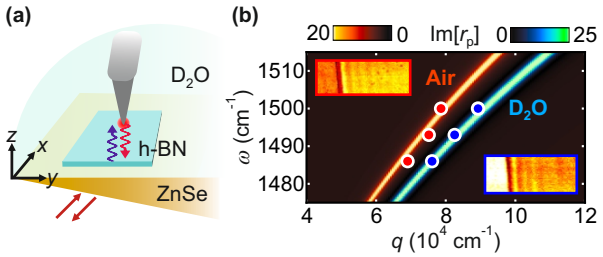

Figura 1.3.: **s-SNOM basado en TIR para el mapeo de polaritones fonónicos en un entorno líquido.** (a) Esquema del s-SNOM basado en TIR en líquido. (b) Dispersión de PhPs h-BN en líquido y en aire. Los símbolos muestran los momentos PhP medidos. El gráfico de colores indica la parte imaginaria calculada del coeficiente de reflexión de Fresnel dependiente del momento y de la frecuencia, $\mathrm{Im}\,[r_\mathrm{p}]$, de una lámina de h-BN de $90\,\mathrm{nm}$ de espesor sobre ZnSe en aire (rojo) y $\mathrm{D_2O}$ (azul). En el recuadro se muestran imágenes de amplitud de campo cercano de PhPs de h-BN lanzadas en aire (arriba a la izquierda) y en líquido (abajo a la derecha).

2. Summary

Infrared (IR) vibrational spectroscopy serves as a powerful, label-free characterization tool that is used in both research and industrial applications due to its chemical specificity and sensitivity to the chemical structure of the sample [1–5]. However, like most optical techniques, the spatial resolution of IR spectroscopy is limited by the diffraction limit to typically around $\lambda/2$ (i.e., at the micrometer length scale) [6]. This limitation makes conventional IR techniques unsuitable for the characterization of nanoscale objects that are crucial in many modern scientific applications.

Scattering type scanning near-field optical microscopy (s-SNOM) [7–9] is a well established technique based on atomic force microscopy (AFM) that circumvents the diffraction limit, enabling nanoscale resolved imaging and spectroscopy across a broad spectral range, from visible to sub-THz frequencies [10–12]. In s-SNOM, a metal-coated AFM tip is illuminated with monochromatic light. The tip acts as an antenna and focuses the incoming light to a highly confined and enhanced near field at its apex. The spatial extent of the near field at the tip apex determines the spatial resolution in s-SNOM, which is typically of the order of the tip apex radius $R = 25\,\mathrm{nm}$ [13]. The near fields generated at the tip apex interact with the sample, resulting in a modification of the scattered light influenced by the sample's local dielectric properties. This tip-scattered light is collected using an interferometric detection scheme that allows for the simultaneous measurement of both the amplitude and phase of the scattered field that ultimately allows for the reconstruction of the local dielectric properties of the sample [14, 15]. A nanoscale resolved infrared image of the sample can be generated by recording the tip-scattered light as a function of tip position. Alternatively, a nanoscale-resolved Fourier transform infrared (nano-FTIR) spectrum [16, 17] of the sample can be recorded by illuminating the AFM tip with a broadband infrared laser and recording the tip-scattered light as a function of the reference mirror position at a fixed sample location (interferogram). The sample spectra can then be obtained by applying a Fourier transform to the interferogram and subsequent normalization with respect to a reference spectrum recorded on a spectrally flat area on the sample, such as a clean Si or Au surface.

Both s-SNOM and nano-FTIR spectroscopy are powerful optical techniques that enable nanoscale-resolved characterization of various materials across a broad spectral range.

These techniques have been extensively applied for nanoscale-resolved chemical identification of organic and inorganic samples [16,18–20], mapping the secondary structure of proteins [21,22], local conductivity mapping [23,24], mapping the electromagnetic near field of plasmonic nanostructures [25–29], and visualization of propagating plasmon and phonon polaritons in 2D materials [30–34]. However, the majority of these applications have primarily been demonstrated in air.

There exists an increasing need for nanoscale-resolved infrared imaging and spectroscopy in liquid environments, particularly for various of (bio)chemical and polaritonic sample systems. The strong absorption of IR light by liquids, especially H_2O, and difficulties in maintaining stable tapping mode AFM operation in liquid, have posed significant challenges to the development of s-SNOM and nano-FTIR techniques for studying samples fully immersed in liquids. To overcome these challenges, initial efforts to apply mid-IR s-SNOM for samples in liquid environments involved the use of thin IR transparent membrane-based liquid cells. Here the samples along with the liquid are encapsulated within a membrane, such as SiN, while the s-SNOM is operated in air [35–40].

Alternately and parallel to the work presented in this thesis, novel approaches for s-SNOM operation in liquid were demonstrated, where both the near-field probe as well as the samples were fully submerged in liquid [41,42]. This technique may allow for imaging samples without the need for extensive sample preparation and avoiding near-field probing through the membrane covering the sample, which degrades the spatial resolution. Despite these advancements, the reported techniques are not well established yet and face various technical and scientific challenges.

The primary objective of the work presented in this thesis was to develop and implement the necessary instrumentation to enable mid-IR s-SNOM-based nanoimaging and nano-FTIR spectroscopy in liquid environments. We mainly focus the attention of our work to develop instrumentation techniques for in-situ s-SNOM based mapping and nanospectroscopy of polaritons. Polaritons are well known for their ability to enhance light-matter interactions and play a crucial role in highly sensitive optical analysis of (bio)chemical substances and process. Nanoimaging and spectroscopy of the polaritons' evanescent fields is essential for experimental mode identification and field confinement studies.

To this end, we developed two s-SNOM setups operating with standard Gaussian beams where both the AFM tip and the sample are fully immersed in a liquid environment. This work establishes a foundational first step toward realizing nanoscale resolved studies using s-SNOM and nano-FTIR, paving the way for a range of applications, including in-situ studies of antenna enhanced molecular spectroscopy, strong coupling between polaritons and molecular vibrations, and chemical reactions at the surface of polaritonic materials, whether bare or functionalized.

This thesis is organized as follows:

In Chapter 3, a brief introduction to the fundamental concepts of s-SNOM and nano-FTIR spectroscopy is provided. To this end, first the foundational principles of AFM, which serves as the base of s-SNOM, are described. This is followed by a detailed description of the working principle of s-SNOM and the background suppression strategies necessary for isolating near field signals from the tip-scattered field. Additionally, a discussion of the interferometric detection schemes employed in s-SNOM for achieving amplitude- and phase-resolved infrared nanoimaging and nanospectroscopy is provided. Finally, an overview of a standard s-SNOM and nano-FTIR experimental setup is presented, which serves as the foundation for the experimental setup developed during the course of this thesis.

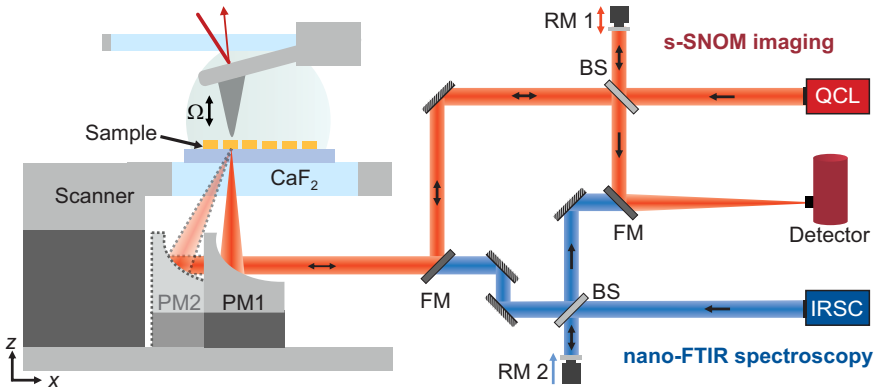

Figure 2.1.: **Schematic representation of the bottom illumination and detection scheme for IR s-SNOM nanoimaging (red) and nanospectroscopy (blue) in liquid.** A schematic of the two illumination and detection schemes designed for amplitude- and phase-resolved s-SNOM (red) and nano-FTIR (blue) in a liquid environment. In the first scheme, the sample is illuminated from either a monochromatic (red) or a broadband (blue) source under normal incidence using a parabolic mirror (PM1). In the second scheme, the sample is illuminated from either a monochromatic (red) or a broadband (blue) source with totally internally reflected light from a ZnSe wedge (not shown here, see Figure 2.3) using a second parabolic mirror (PM2). BS, beamsplitter; FM, flip mirror; RM1, piezo actuated vibrating mirror; RM2, piezo actuated translating mirror; QCL, frequency-tunable quantum cascade laser; IRSC, infrared supercontinuum broadband laser.

In Chapter 4, a detailed description of the development and implementation of two novel experimental setups to enable IR s-SNOM imaging and nano-FTIR spectroscopy of samples in a liquid environment is provided. Side illumination and collection scheme employed in typical s-SNOM experiments [13] is unsuitable for operation in liquid due to

the strong absorption of the infrared radiation by the liquid, especially H_2O. This chapter introduces a bottom illumination and collection scheme (see schematic in Figure 2.1) that minimizes infrared light absorption in liquid. In the first implementation, the tip is illuminated under normal incidence (transflection s-SNOM) and the backscattered light is collected via an interferometric detection scheme. The transflection geometry is an ideal setup for the mapping and characterization of localized plasmon polaritons in metal antennas in air and in a liquid environment. In the second implementation, the tip is illuminated with the totally internally reflected (TIR) light from a $ZnSe$ wedge (TIR-based s-SNOM, see Figure 2.3). The backscattered light is detected interferometrically as in transflection s-SNOM. The TIR based s-SNOM setup is then applied for nanoscale resolved infrared chemical mapping and identification in air and in a liquid environment. These advancements significantly enhance the capability of s-SNOM and nano-FTIR for in-situ, label-free characterization of materials, opening new avenues for studying bio-chemical processes and molecular sensing in liquids.

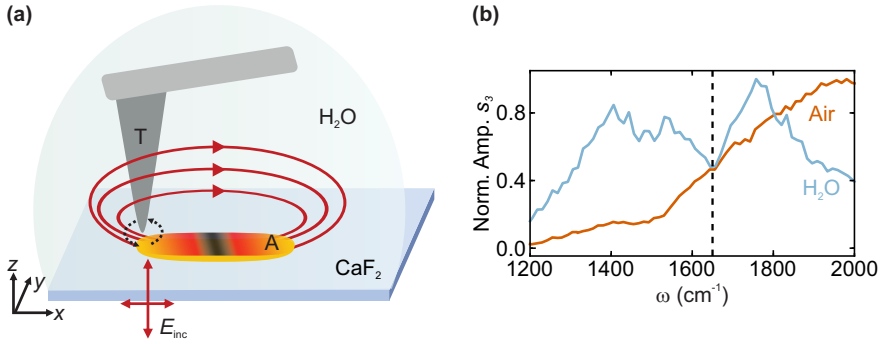

Figure 2.2.: **Transflection s-SNOM imaging and nano-FTIR spectroscopy of infrared metal nanostructures.** (a) Illustration of the near field scattering process. The incident field E_{inc} illuminates the antenna (A). The antenna fields illuminate and polarizes the AFM tip (T), which scatters the near fields via the antenna into the far field where it is detected via an interferometric detection scheme (not shown here). (b) Normalized amplitude spectra $s_3(\omega)$ of an individual metal rod antenna in air (red) and in a liquid environment (H_2O; blue).

In Chapter 5, the normal incidence transflection nano-FTIR setup is applied for infrared spectroscopy of resonant metal antennas both in air and liquid environments. Nanoscale-resolved imaging and spectroscopy of the antenna near fields in liquids provide critical insights for designing and optimizing infrared metal antennas, paving the way for future applications in in-situ molecular sensing. In transflection nano-FTIR, a metal coated AFM tip is illuminated via the antenna near fields and the backscattered light from the antenna is recorded with an asymmetric FTIR spectrometer. A schematic of the tip

illumination is shown in Figure 2.2. This chapter provides a reliable methodology for acquiring, referencing, and stitching of transflection nano-FTIR spectra of individual metal antennas in both air and liquid environments. A normalized transflection amplitude spectra $s_3(\omega)$ of an individual metal rod antenna recorded in air (red) and in H_2O (blue) is shown in Figure 2.2b. The impact of H_2O on the antenna resonance can be clearly seen in the Figure 2.2b. This work provides a foundational framework for future transflection nano-FTIR study of antenna enhanced (bio)chemical sensing, chemical interactions, and vibrational strong coupling experiments.

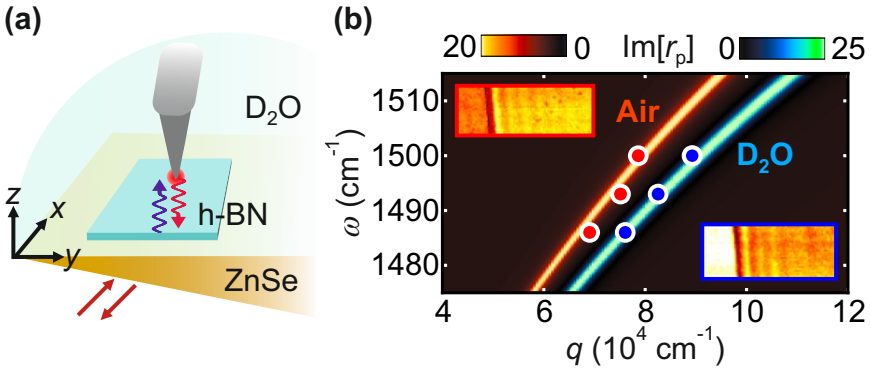

Figure 2.3.: **TIR based s-SNOM for phonon polariton mapping in a liquid environment.** (a) Schematic of TIR based s-SNOM in liquid. (b) Dispersion of h-BN PhPs in liquid and in air. Symbols show measured PhP momenta. The color plot indicates the calculated imaginary part of the momentum- and frequency-dependent Fresnel reflection coefficient, $\mathrm{Im}\,[r_\mathrm{p}]$, of a $90\,\mathrm{nm}$ thick h-BN flake on ZnSe in air (red) and D_2O (blue). Inset shows near-field amplitude images of h-BN PhPs launched in air (top left) and in liquid (bottom right).

In Chapter 6, the TIR-based s-SNOM setup is applied for probing ultraconfined phonon polaritons (PhPs) in hexagonal boron nitride (h-BN) flakes in air and liquid. Probing ultraconfined infrared phonon polaritons in h-BN in a liquid environment offers new possibilities for exploiting the properties of polaritons for ultracompact and highly sensitive devices for biomolecular sensing in liquid environments. A schematic of the TIR-based illumination scheme is shown in Figure 2.3a, where the metallized AFM tip is illuminated with the totally internally reflected light at the top surface of a ZnSe wedge. The tip is used for both launching and probing the PhPs. Nanoimaging (see inset to the Figure 2.3b) and nanospectroscopy of ultraconfined h-BN phonon polaritons in liquid reveals that the presence of liquid shifts the PhP dispersion to higher momenta. A comparison of the PhP dispersions in air and in liquid is shown in Figure 2.3b. This work establishes a strong foundation for future polariton enhanced s-SNOM and nano-FTIR studies for a plethora of applications ranging from studying (bio)chemical interactions

to strong coupling experiments in liquid environments.

3. Nanoscale-resolved infrared imaging and spectroscopy

Scattering-type scanning near-field optical microscopy (s-SNOM) and nanoscale-resolved Fourier transform infrared (nano-FTIR) spectroscopy are scanning probe microscopy techniques that enable optical characterization of diverse sample systems with nanoscale spatial resolution. The resolution in these techniques surpasses the diffraction limit by focusing incoming light onto the apex of an atomic force microscopy (AFM) tip and recording the tip-scattered light, which contains information on the local dielectric properties of the sample. These techniques have wide application potential, including direct visualization of surface plasmons and phonon polaritons, as well as nanoscale chemical characterization and identification of organic and inorganic materials. This chapter introduces the fundamental concepts and working principles of s-SNOM and nano-FTIR spectroscopy in air.

3.1. Introduction

Optical microscopy and spectroscopy serve as powerful tools for the visualization and characterization of samples across various scientific domains, including medicine, biology, chemistry, and material sciences [6,43,44]. Particularly noteworthy is the infrared (IR) region of the electromagnetic spectrum ($\omega \approx 400 - 4000\,\mathrm{cm}^{-1}$, corresponding to the wavelength range $\lambda \approx 2.5 - 25\,\mu\mathrm{m}$), where photon energies coincide with molecular and crystal lattice vibrational modes. This makes IR light exceptionally sensitive to the chemical and structural properties of the materials [45,46].

The spatial resolution of conventional optical techniques is constrained by the diffraction limit, to approximately $\sim \lambda/2$ [6,47,48]. For instance, with IR light of wavelength $\lambda \approx 10\,\mu\mathrm{m}$, the spatial resolution is limited to about $\lambda/2 \approx 5\,\mu\mathrm{m}$. Consequently, this limit in spatial resolution hinders the use of these techniques for many applications in modern science that require the investigation and characterization of nanoscale structures, including biological samples, nanoscale electronic and photonic devices, and nanoscale materials and composites.

Scanning probe microscopy (SPM) [49] techniques enable high resolution imaging by employing a sharp tip to scan the sample surface while recording various properties

(mechanical, optical, electrical, etc.) of the sample as a function of the tip position. Among the SPM techniques, atomic force microscopy (AFM) [50] is widely utilized, offering nanoscale-resolved images of the sample topography along with insights into the local mechanical [51–53], thermal [54], and electrical [55] properties of the sample in air [56,57], liquids [58–60], and ultrahigh vacuum [61–63].

Optical near-field techniques, such as scattering-type near-field optical microscopy (s-SNOM) [9,13], photothermal expansion (PTE) microscopy [64–66], and photoinduced force microscopy (PiFM) [67], are AFM-based techniques, in which the optical near fields confined to the apex of a metal-coated AFM tip are used to probe local optical properties with nanoscale resolution, overcoming the diffraction limit. The imaging process involves recording the tip-scattered field as a function of the sample position, where the spatial resolution is mainly determined by the radius of the tip apex, rather than the wavelength of the probing light [13].

In s-SNOM, the tip-scattered light is analyzed using a Michelson interferometer [68,69], facilitating simultaneous detection of both the amplitude and phase of the detected signal. This detection scheme offers many advantages over other near-field optical techniques, such as PTE [64–66] and PiFM [67]. These advantages include direct near-field phase measurements for determining phase and group velocities of polaritons [33], the reconstruction of complex-valued dielectric functions [14,15], and tomographic sample reconstruction [70]. Furthermore, s-SNOM supports nanoimaging and nanospectroscopy across a broad spectral range, from visible to sub-THz frequencies, employing continuous-wave (CW) and ultrafast lasers [71,72], synchrotrons [19,73], or free-electron lasers [74].

s-SNOM-based nanoimaging and nanospectroscopy constitute the core of the research presented in this thesis. This chapter outlines the working principles of s-SNOM and provides a brief introduction to AFM. Additionally, the interferometric detection schemes employed for nanoimaging (pseudo-heterodyne and synthetic optical holography) and nanospectroscopy (nano-FTIR) are discussed. Finally, the experimental implementation of amplitude- and phase-resolved s-SNOM and nano-FTIR are described briefly.

3.2. Atomic force microscopy (AFM)

AFM [50,57] is one of the most powerful and versatile SPM techniques routinely employed for investigating the nanomechanical properties of a wide range of sample systems such as polymers, biological membranes, and electronic devices [75–78]. In AFM, a sharp tip with a typical apex radius of $R = 1 - 50\,\mathrm{nm}$ is scanned across the sample surface. The mechanical forces between the tip and the sample are measured as a function of the tip position to generate a nanoscale-resolved map of the sample's

mechanical properties. The AFM tip is usually mounted on a long, flexible cantilever. As the tip scans over the sample surface, changes in the tip-sample interaction(e.g. due to sample topography) causes a change in the cantilever deflection.

The cantilever's deflection is monitored optically by focusing a laser beam (deflection laser) onto the back of the cantilever. The reflected laser beam off the cantilever's backside is directed to a position-sensitive detector, typically a quadrant photodiode. Any variations in the cantilever deflection leads to a change in the angle at which the laser beam reflects off the cantilever. Usually a feedback system is used to maintain a constant tip-sample interaction by adjusting the vertical position of the cantilever or the sample. By monitoring these changes while scanning the sample, a map of the sample topography (height) and other mechanical properties can be obtained with nanoscale resolution.

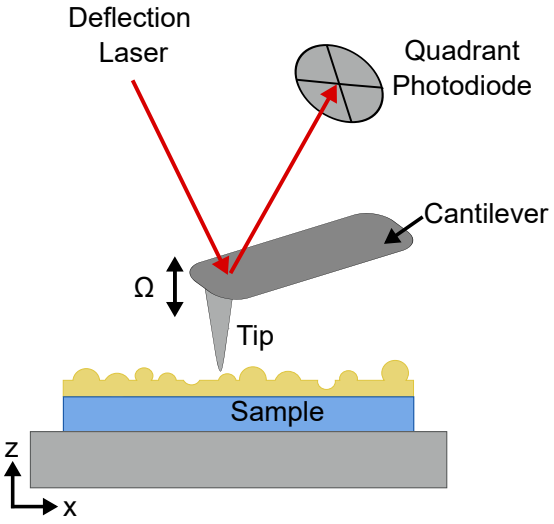

Figure 3.1.: **Illustration of a tapping mode AFM.** In tapping mode AFM, a nanoscale-resolved topography image of the sample surface is generated by raster scanning the sample under a tip oscillating at a frequency Ω. The cantilever oscillation is monitored by measuring the reflection of the deflection laser beam from the backside of the cantilever with a position-sensitive quadrant photodiode. The sample topography modifies the oscillation amplitude of the cantilever. The tip oscillation amplitude is kept constant by a closed feedback loop controlling the vertical position (along the $z-$axis) of the sample while raster scanning the sample.

AFM can be operated in several modes: contact mode, non-contact mode, and tapping (intermittent-contact) mode. Of these, tapping mode AFM forms the basis of s-SNOM. Figure 3.1 illustrates a typical tapping-mode AFM setup. In this mode, a cantilevered AFM tip oscillates near the resonant frequency of the cantilever, typically within the

range of $10 - 300\,\mathrm{kHz}$, with an amplitude ranging from $1 - 100\,\mathrm{nm}$, driven by a piezoelectric actuator [56]. To map the local mechanical properties of a sample, such as its topography, the sample is gradually brought close to the tip until the oscillation amplitude decreases to a set point of approximately $80 - 90\%$ of the cantilever's free oscillation amplitude. As the tip oscillates near the sample, during each oscillation cycle it intermittently makes contact with the sample surface, thus effectively "tapping" it. The oscillation amplitude serves as a feedback parameter in a closed-loop operation. A feedback loop is used to maintain a constant oscillation amplitude by adjusting the sample's height along the $z-$axis. By monitoring these vertical adjustment while raster scanning the sample surface, a two-dimensional map of the sample's topography is generated.

In addition to topography, the phase shift between the signal that drives the cantilever oscillation and the cantilever response is highly sensitive to variation in material properties such as as the elastic modulus, stiffness, and adhesion forces [79, 80].

One of the many advantages of AFM is that it can be adapted for operation in nearly any environment, including air [56, 57], ultra-high vacuum [61–63], or liquids [58–60]. AFM of samples fully immersed in liquid is particularly interesting in the field of (bio)chemistry [58, 75, 81], as it allows for the study of many dynamic processes and interactions with nanoscale resolution. In liquids, tapping mode AFM is usually preferred due to low lateral forces exerted by the tip onto the sample, which allows for imaging of soft samples with minimal degradation [82, 83]. Nonetheless, the presence of liquid can significantly alter the cantilever dynamics, making liquid-based AFM experiments more challenging to perform and interpret, detailed description of AFM operation in liquid is provided in Chapter 4, Section 4.3.1.

3.3. s-SNOM working principle and implementation

Scanning near-field optical microscopy (s-SNOM) is a technique based on AFM, that extends the capabilities of optical techniques by overcoming the diffraction limit through the confinement of electromagnetic radiation at the tip apex. This confined field interacts with the sample, and by detecting the tip-scattered field while raster scanning the sample, it is possible to obtain a map of the sample's local optical properties with nanoscale resolution, simultaneous to the sample topography. In this section, core concepts integral to s-SNOM operation will be briefly described.

3.3.1. Tip illumination and near-field enhancement in s-SNOM

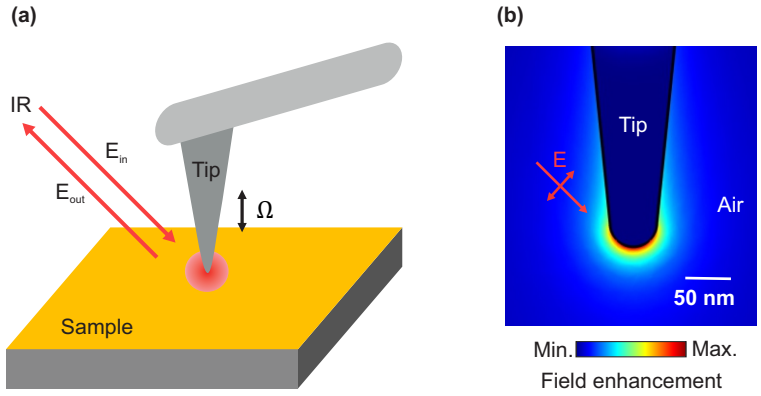

Figure 3.2.: **Working principle of s-SNOM and nano-FTIR.** (a) A metallic AFM tip (operating in tapping mode, where Ω is the tip oscillation frequency) is illuminated by a focused laser beam (IR in our case). The electric near-field confined at the tip apex interacts with the sample and modifies the tip-scattered field. By recording the tip-scattered field, the local optical properties of the sample can be measured while raster scanning the sample below the tip. (b) Simulated electric near-field distribution for a Pt tip (length $L = 10\,\mu\mathrm{m}$, apex radius $R = 25\,\mathrm{nm}$) illuminated with p-polarized IR light of wavelength $\lambda = 6\,\mu\mathrm{m}$ at an angle of $60°$ with respect to the tip axis, showing the electric field enhancement in the vicinity of the tip apex. The electric field distribution was simulated using the COMSOL Multiphysics software.

In s-SNOM, a metallic AFM tip is illuminated by a focused laser beam (visible, infrared, or terahertz) to enable nanoscale-resolved optical imaging simultaneously with topography mapping of the sample. Figure 3.2a illustrates the working principle of s-SNOM. The metallic tip functions as an antenna, concentrating the incoming radiation E_{in} into a highly confined and enhanced spot at the apex of the tip. This high electric field at the tip apex can be attributed to the accumulation of charges at the tip apex due to the lightning rod effect [47], along with the excitation of localized surface plasmon polaritons in the metal [47,84,85]. Figure 3.2b shows the simulated electric field enhancement at the apex of a Pt tip (the tip is modeled as a $10\,\mu\mathrm{m}$ long Pt cone ($\epsilon_{\mathrm{Pt}} = -549.56 + 255.33i$) [86] with an apex radius $R = 25\,\mathrm{nm}$) illuminated by IR radiation of wavelength $\lambda = 6\,\mu\mathrm{m}$ at an angle of $60°$ with respect to the tip axis. The electric field is p-polarized, i.e., oriented parallel to the tip axis. It can be seen that the metallic tip concentrates the electromagnetic radiation at the apex, and the near-field hotspot is strongly confined to a length scale of a few tens of nm, i.e., of the order of the apex radius $R = 25\,\mathrm{nm}$ [10,11,13],

which is significantly smaller than the diffraction-limited laser focus (i.e., $\ll \lambda/2$). This electric field confinement is essential for achieving sub-diffraction-limit resolution.

When the tip is brought into proximity with a sample, the electromagnetic near-field at the tip apex interacts with the sample, modifying the scattered field E_{sca} based on the local optical properties of the sample. By scanning the tip across the sample surface, we obtain a near-field optical image with the spatial resolution determined by the tip apex radius $R_{\mathrm{t}} = 25\,\mathrm{nm}$ [10, 11, 13] rather than the optical wavelength. This improvement in resolution arises from the non-propagating nature of near-field interactions, which decay exponentially with distance from the tip apex, thereby confining the interaction to a lateral extent of the order of the apex radius R_{t}.

The tip-scattered field E_{sca}, containing information about the local optical properties of the sample is detected in the far field and can be related to the incoming field E_{in} through the complex-valued scattering coefficient $\sigma = se^{i\phi}$ [8, 13], such that

$$E_{\mathrm{sca}} = \sigma E_{\mathrm{in}} = se^{i\phi} E_{\mathrm{in}}, \tag{3.1}$$

where s and ϕ are the scattering amplitude and phase, respectively. The relationship between E_{sca} and the dielectric properties of the sample are described below.

3.3.2. Tip-sample near-field interaction

The interaction between the tip and the sample in s-SNOM can be approximated using a point-dipole model. In this model, the tip apex is approximated as a sphere with radius R_{t} and dielectric permittivity ϵ_{t} [87,88]. A schematic of the point-dipole model is shown in Figure 3.3. The tip is illuminated by an incident electric field with field strength E_{in}, along with a far-field reflection from the sample surface. Therefore, the total incident field strength at the tip apex is given by $(1 + r_{\mathrm{s}})\, E_{\mathrm{in}}$, where r_{s} is the far-field reflection coefficient of the sample. This incident field polarizes the tip, inducing a dipole moment p given by:

$$p \propto \alpha(1 + r_{\mathrm{s}}) E_{\mathrm{in}}, \tag{3.2}$$

where α is the polarizability of the tip. For a sphere of radius R_t in air ($\epsilon_{\mathrm{air}} \approx 1$), α can be expressed as:

$$\alpha = 4\pi R_{\mathrm{t}}^3 \frac{\epsilon_{\mathrm{t}} - 1}{\epsilon_{\mathrm{t}} + 2}. \tag{3.3}$$

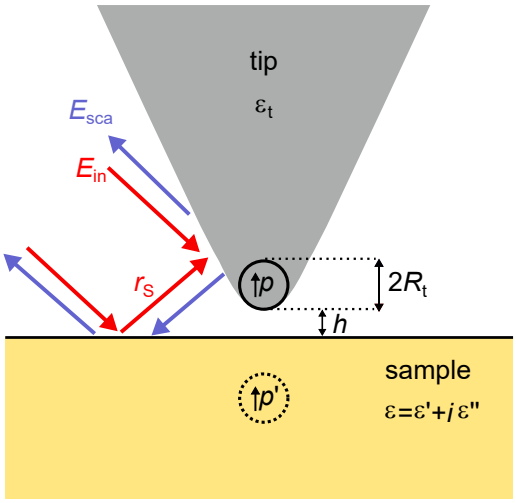

Figure 3.3.: **Schematic of the point-dipole model.** A metallic AFM tip in close proximity to the sample surface is illuminated by an incident electric field E_{in} and its reflection from the sample surface. The incident field induces a dipole moment p in the tip, approximated by a sphere of radius R_{t} located at its apex. The tip-sample near-field interaction is described by the interaction of the tip dipole p with its mirror dipole p' located below the sample surface.

For $R_t \ll \lambda$, where λ is the wavelength of the incident light, the tip dipole p can be described by a point dipole located at the center of the sphere. The interaction between the tip and the sample can be modeled as an electrostatic interaction between the tip dipole p and its mirror dipole $p' = \beta p$ located below the sample surface, where

$$\beta = \frac{(\epsilon - 1)}{(\epsilon + 1)} \tag{3.4}$$

is the quasi-static near-field reflection coefficient, which depends on the local dielectric constant ϵ of the sample [8, 14]. By solving the electrostatic equations describing the multiple interactions between the tip and mirror dipoles, the effective polarizability of the coupled tip-sample system α_{eff} can be expressed as [8]

$$\alpha_{\mathrm{eff}} = \frac{\alpha}{1 - \frac{\alpha\beta}{16\pi(h+R_{\mathrm{t}})^3}}. \tag{3.5}$$

Here, h denotes the tip-sample separation. For tip-sample separation $h < R_{\mathrm{t}}$, a sharp increase in the near-field scattering is observed. This sharp increase is a significant indicator of strong near-field interactions between the tip and the sample and is crucial for background suppression schemes, which will be discussed in subsequent sections. The field scattered from the coupled dipole system is related to the effective polarizability

as [8,89]

$$E_{\mathrm{sca}} \propto \alpha_{\mathrm{eff}} E_{\mathrm{in}}. \tag{3.6}$$

Since parameters such as α, β, and ϵ are generally complex-valued, the scattering coefficient σ also becomes complex and is defined as (using Equations (3.1) and (3.6)):

$$\sigma = se^{i\phi} = \frac{E_{\mathrm{sca}}}{E_{\mathrm{in}}} \propto \alpha_{\mathrm{eff}} \left(1 + r_{\mathrm{s}}\right)^2. \tag{3.7}$$

Here, s and ϕ represent the relative amplitude and phase shift between the incident and the scattered light, respectively. The $(1 + r_{\mathrm{s}})^2$ term accounts for the direct tip illumination and illumination via reflection at the sample surface. Equations (3.4), (3.5), and (3.7) provide a qualitative understanding of the tip-sample interaction in s-SNOM, linking the observed signals s and ϕ to the dielectric properties of the sample via the effective polarizability α_{eff} [8,10].

For a more precise and quantitative description of these signals, advanced models such as the finite-dipole model for bulk samples [90,91], for layered samples [92], or numerical modeling of the tip-sample interaction [93–95] are essential.

3.3.3. Background suppression

Effective background suppression is a critical aspect of s-SNOM for achieving distortion-free, high-resolution nanoimaging and spectroscopy. Techniques such as higher harmonic demodulation play an essential role in isolating the near-field signal from the background. In s-SNOM, the total detected signal E_{sca} comprises both the desired near-field signal E_{nf}, originating from the localized interaction at the tip apex, and an undesirable background signal E_{bg}, due to scattering from the tip shaft, the cantilever, and other regions outside the near-field interaction zone (caused by diffraction-limited illumination of the AFM tip).

The total scattered field detected in the far field can be expressed as the superposition of near-field E_{nf} and background E_{bg} components:

$$E_{\mathrm{sca}} = E_{\mathrm{nf}} + E_{\mathrm{bg}} = \sigma_{\mathrm{nf}} E_{\mathrm{in}} + \sigma_{bg} E_{\mathrm{in}}, \tag{3.8}$$

where E_{in} denotes the incoming field, and $\sigma_{\mathrm{nf}} = s_{\mathrm{nf}} e^{i\phi_{\mathrm{nf}}}$ and $\sigma_{bg} = s_{\mathrm{bg}} e^{i\phi_{\mathrm{bg}}}$ are the complex-valued scattering coefficients for the near-field and background components, respectively.

The detector measures only the intensity of the scattered electric field,which is given by

$$I_{\mathrm{det}} \propto I_{\mathrm{sca}} = |E_{\mathrm{sca}}|^2 = |E_{\mathrm{nf}} + E_{\mathrm{bg}}|^2 = (E_{\mathrm{nf}} + E_{\mathrm{bg}}) (E_{\mathrm{nf}} + E_{\mathrm{bg}})^*. \tag{3.9}$$

By employing the tapping mode of AFM, as previously discussed in Section 3.2, the tip oscillates vertically near its resonant frequency Ω with an amplitude $A \ll \lambda$. The tip oscillation modulates the scattered field E_{sca} and can be expressed as a Fourier series:

$$E_{\mathrm{sca}} = \sum_{n=0}^{\infty} E_{\mathrm{nf},n} \cos(n\Omega t) + \sum_{n=0}^{\infty} E_{\mathrm{bg},n} \cos(n\Omega t) \tag{3.10}$$

where $E_{\mathrm{nf},n}$ and $E_{\mathrm{bg},n}$ are the n^{th} order Fourier coefficients of the near-field E_{nf} and background E_{bg} electric fields, respectively [91].

The near-field signal E_{nf}, which originates from the interaction of the highly localized evanescent field at the tip apex with the sample (see also Figure 3.2b), exhibits a sharp decay as the tip-sample distance increases. This strong non-linear dependence of the near-field signal E_{nf} on the tip-sample distance [47] (as seen in Equation (3.5)) leads to significant contributions from the near-field signal at higher harmonics of the tip oscillation frequency Ω. Conversely, the background signal E_{bg} varies much more slowly over distances comparable to the wavelength λ of the incident field E_{in} and is almost constant at the length scales of the oscillation amplitude A. Hence, the higher-order Fourier coefficients of the background signal are negligible compared to those of the near-field signal, i.e., $E_{\mathrm{bg},n} \ll E_{\mathrm{nf},n}$ for $n \geq 2$.

Therefore, demodulating the signal at high harmonics ($n \geq 2$) substantially minimizes the background contribution. From Equations (3.9) and (3.10), the intensity of the nth harmonic of the detected signal can be written as:

$$I_{\mathrm{det},n} \propto E_{\mathrm{bg},0} E^*_{\mathrm{nf},n} + E_{\mathrm{nf},n} E^*_{\mathrm{bg},0} \approx s_{\mathrm{bg},0}.s_{\mathrm{nf},n} \cos(\phi_{\mathrm{nf},n} - \phi_{\mathrm{bg},0}) \,. \tag{3.11}$$

Here, $s_{\mathrm{bg},0}$, $\phi_{\mathrm{bg},0}$ and $s_{\mathrm{nf},n}, \phi_{\mathrm{nf},n}$ represent the amplitude and phase of the nth order components of the background and near-field scattering, respectively.

Equation (3.11) shows that even at higher harmonics, near-field components $E_{\mathrm{nf},n}$ are influenced by the lower-order background components $E_{\mathrm{bg},0}$, indicating a multiplicative relationship between them. Thus, while higher harmonic demodulation effectively reduces the background, it does not entirely eliminate it. To completely eliminate this multiplicative background, interferometric detection schemes, such as pseudo-heterodyne detection (Section 3.4.1) and synthetic optical holography (Section 3.4.2), are often utilized.

3.4. Advanced detection techniques in s-SNOM

In addition to higher harmonic demodulation, s-SNOM incorporates interferometric detection schemes, where the near-field signals are mixed with a reference beam. The

resulting interference effectively eliminates both additive and multiplicative background contributions and allows for the simultaneous measurement of the amplitude and phase of the scattered signal. The interferometric schemes employed in s-SNOM for nanoimaging and nanospectroscopy are briefly described below:

3.4.1. Pseudo-heterodyne interferometric detection

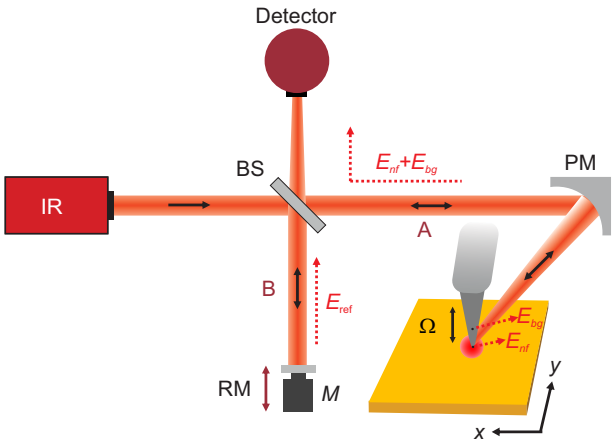

Figure 3.4.: **Schematic of the pseudo-heterodyne s-SNOM imaging setup.** The tip is illuminated with a monochromatic infrared (IR) source. The tip-scattered light is detected using a Michelson interferometer, which consists of a beamsplitter (BS), a reference mirror (RM), and a parabolic mirror (PM). The reference mirror oscillates with a frequency $M < \Omega$ (Ω is the tip oscillation frequency), phase modulating the reference beam. The detector signal is demodulated at frequencies $n\Omega \pm mM$.

Pseudo-heterodyne detection [96] is a technique in s-SNOM that employs a Michelson interferometer to achieve simultaneous measurement of both the near-field optical amplitude and phase in s-SNOM. A schematic of the pseudo-heterodyne detection scheme is shown in Figure 3.4. Light from a monochromatic IR source is divided into two parts (A and B) by a beamsplitter (BS). One part of the beam (A) is directed towards the tip apex using a parabolic mirror (PM). The tip-scattered light is collected by the same parabolic mirror and is steered to the detector. The other part of the beam (B) is reflected off a reference mirror (RM) and is combined with the scattered light at the detector. The resulting intensity at the detector (see Equation (3.9)) due to the interference of the two beams can be expressed as follows:

$$I_{\mathrm{det}} \propto \left|E_{\mathrm{bg}} + E_{\mathrm{nf}} + E_{\mathrm{ref}}\right|^2 = \left(E_{\mathrm{bg}} + E_{\mathrm{nf}} + E_{\mathrm{ref}}\right)\left(E_{\mathrm{bg}} + E_{\mathrm{nf}} + E_{\mathrm{ref}}\right)^*, \tag{3.12}$$

where E_{ref} denotes the reference electric field.

In s-SNOM, the tip oscillation modulates the rapidly changing near-field signal (which decays exponentially with increasing tip-sample distance; see Section 3.3.3) generating near-field scattering components at integer multiples of the tip oscillation frequency, $n\Omega$ (typically in the range of a few hundred kHz with $n \geq 2$), whereas the slowly changing background is mostly confined to the components with $n \leq 1$.

In pseudo-heterodyne detection, the reference beam is phase-modulated by oscillating the reference mirror along the beam path at a frequency M (typically around $M = 300\,\mathrm{Hz}$). The interference of the phase-modulated reference beam with the tip-scattered field at the detector generates additional sidebands at frequencies $n\Omega \pm mM$ (where m is a non-zero integer, typically $m \geq 1$). When utilizing the phase-modulated reference beam, the multiplicative background appears only on the $n\Omega$ components and is notably absent at the sideband frequencies ($n\Omega \pm mM, m \geq 1$) [96].

Thus, by measuring the intensity $I_{n,m}$ of the first $I_{n,1}$ and second $I_{n,2}$ sidebands of the modulated signal at sufficiently high harmonics of the tip oscillation ($n \geq 2$), pseudo-heterodyne detection can effectively separate the near-field signal from the multiplicative background [91,96] (see discussion in Section 3.3.3). The background-free near-field amplitude $s_{\mathrm{nf},n}$ and phase $\phi_{\mathrm{nf},n}$ can be written as:

$$s_{\mathrm{nf},n} = 2.16k\sqrt{I_{n,1}^2 + I_{n,2}^2} \tag{3.13}$$

and

$$\phi_{\mathrm{nf},n} = \arctan\left(2.16k\frac{I_{n,2}}{I_{n,1}}\right), \tag{3.14}$$

where k is a complex-valued proportionality constant. Note that the validity of these equations requires that the amplitude of the reference mirror oscillation is set to 0.21λ, λ being the wavelength of the incident light [91,96].

The exact value of k does not need to be determined, as s-SNOM typically focuses on relative material contrasts, which allows for comparisons between measurements under varying experimental conditions. The factor $2.16k$ cancels out when s-SNOM signals are normalized to a known reference material, usually a spectrally flat substrate such as Si or Au. The normalized complex-valued scattering coefficient can be expressed as:

$$\frac{\sigma_{\mathrm{nf},n}^{\mathrm{sam}}}{\sigma_{\mathrm{nf},n}^{\mathrm{sub}}} = \frac{s_{\mathrm{nf},n}^{\mathrm{sam}}}{s_{\mathrm{nf},n}^{\mathrm{sub}}}\exp\left(i\left(\phi_{\mathrm{nf},n}^{\mathrm{sam}} - \phi_{\mathrm{nf},n}^{sub}\right)\right), \tag{3.15}$$

where $\sigma_{\mathrm{nf},n}^{\mathrm{sam}}$ and $\sigma_{\mathrm{nf},n}^{\mathrm{sub}}$ are the near-field scattering coefficients of the sample and the substrate, respectively.

In summary, pseudo-heterodyne detection in s-SNOM leverages the oscillatory behavior

of the tip and modulated reference beam to facilitate background suppression and accurate measurement of near-field interactions, aiding in nanoscale-resolved optical characterization of materials.

3.4.2. Synthetic optical holography (SOH)

Optical holography [97,98] is an imaging technique where the light scattered from an object illuminated with a monochromatic coherent source is superimposed with a reference beam. The resulting interference pattern, referred to as a hologram, encodes the complex optical field scattered from an object in a single image. Owing to the speed and ease of implementation of optical holography (especially digital holography [99,100]), it is widely used for reconstructing three-dimensional images [101,102], quantitative phase imaging of biological samples [103,104], and non-destructive product testing [100].The ability to detect complex optical fields makes holography an interesting approach for enabling rapid phase resolved imaging in s-SNOM. While digital holography utilizes a camera (essentially a two-dimensional array of point detectors) to record a hologram, s-SNOM relies on a single point detector to capture the tip-scattered light. This distinction complicates the adaptation of holographic methods to s-SNOM systems.

Synthetic optical holography (SOH) based on synthetic reference waves leverages both the high spatial resolution of s-SNOM and the phase sensitivity of holography to enable phase-resolved near-field imaging with significantly improved speed and technical simplicity [105]. The synthetic reference wave is generated sequentially by slowly varying the phase of the reference field while scanning the sample.

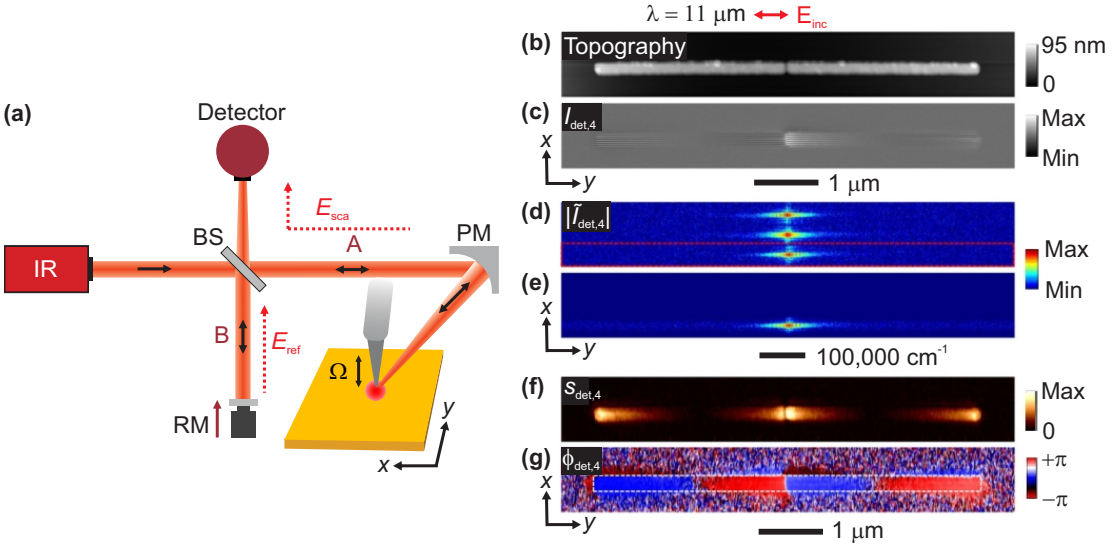

Figure 3.5.: **Schematic and experimental demonstration of SOH for phase resolved nanoimaging.** (a) Light from a monochromatic coherent IR source is focused on the tip via a parabolic mirror (PM). The same PM is used to collect the tip-scattered light. The tip-scattered light is overlapped with the reference beam, which is phase-modulated by slowly translating the reference mirror (RM) while recording an image of the sample. The detector signal is demodulated at higher harmonic of the tip's oscillation frequency, Ω, to record a synthetic hologram of the sample. BS, beamsplitter. (b) AFM topography of two Au rods forming an infrared gap antenna (rod length $l = 2.9\,\mu$m, gap width $w = 50\,$nm) on a CaF_2 substrate. (c) Synthetic hologram, obtained by recording the intensity at the detector $I_{\mathrm{det},4}(\mathbf{r})$ as a function of the distance $\boldsymbol{r}$. (d) Magnitude of the Fourier transform of the synthetic hologram $\left|\tilde{I}_{\mathrm{det},4}\right|(\mathbf{q})$, showing three peaks corresponding to the autocorrelation (middle), direct (top), and conjugate (bottom) terms. (e) Filtered Fourier transform (by applying a Hamming window) according to the red dashed box in d. (f,g) Reconstructed near -field amplitude ($s_{\mathrm{sca},4}$) and phase images($\phi_{\mathrm{sca},4}$). Figure b-g are reproduced from Reference [105].

Figure 3.5a illustrates a typical SOH s-SNOM setup. Analogous to the pseudo-heterodyne interferometric detection discussed in Section 3.4.1, the tip is illuminated with a monochromatic, coherent infrared light source and the tip-scattered light is recorded while raster scanning the sample. For amplitude- and phase-resolved imaging, a Michelson interferometer is employed to combine the tip-scattered field E_{sca} (path A) with the reference field E_{ref} (path B). However, in contrast to pseudo-heterodyne imaging, where the reference phase ϕ_{ref} is sinusoidally modulated at each pixel, in SOH, the reference phase $\phi_{\mathrm{ref}}(\mathbf{r})$ is varied slowly across the image by linearly translating the

reference mirror (RM) position $\delta(\mathbf{r})$ while the sample is scanned rapidly below the tip. By translating the reference mirror at a constant velocity v_{ref}, the reference phase varies linearly-in-time according to $\phi_{\mathrm{ref}}(t) = \overline{\omega}t + \phi_0$, where ϕ_0 is the reference phase at $t = 0$ and $\overline{\omega}$ is the angular frequency given by $\overline{\omega} = 2\pi \cdot 2v_{\mathrm{ref}}\lambda$. Simultaneously, the sample is raster scanned below the tip, moving rapidly in the x direction with speed v_x. After traveling the full scan length (X), the sample returns to the initial position with the same speed and moves one step in the y direction Δ_y with speed $v_y = {}^{v_x\Delta_y}/_{2X}$. A synthetic reference wave $\mathbf{k}_{\parallel} = (k_x, k_y)$ can thus be introduced, where $k_x = {}^{\overline{\omega}}/_{v_x}$ and $k_y = {}^{\overline{\omega}}/_{v_y} = {}^{2Xk_x}/_{\Delta_y} = {}^{2X\overline{\omega}}/_{v_x\Delta_y}$. The reference phase can then be written as a function of the position ($\mathbf{r} = (x, y)$) as $\phi_{\mathrm{ref}}(r) = \mathbf{k}_{\parallel} \cdot \mathbf{r} + \phi_0$. [105]

A synthetic near-field hologram is generated by superimposing the tip-scattered field $E_{\mathrm{sca}}(\mathbf{r}) \propto \sigma_{\mathrm{sca}} = s_{\mathrm{sca}}(\mathbf{r})\, e^{i\phi_{\mathrm{sca}}(\mathbf{r})}$ with the synthetic reference field $E_{\mathrm{ref}}(\mathbf{r}) \propto \sigma_{\mathrm{ref}} = s_{\mathrm{ref}}(\mathbf{r})\, e^{i\phi_{\mathrm{ref}}(\mathbf{r})}$ at the detector. For background suppression, the detector signal $I_{\mathrm{det}}(\mathbf{r})$ is demodulated at the nth order of the tip oscillation frequency Ω and given by [105]:

$$I_{\mathrm{det},n}(\mathbf{r}) = \sum_{m=-\infty}^{\infty} E_{\mathrm{sca},m+n}(\mathbf{r})\, E^*_{\mathrm{sca},m}(\mathbf{r}) + E^*_{\mathrm{sca},n}(\mathbf{r})\, E_{\mathrm{ref}}(\mathbf{r}) + E^*_{\mathrm{ref}}(\mathbf{r})\, E_{\mathrm{sca},n}(\mathbf{r})\,. \quad (3.16)$$

The $E_{\mathrm{sca},n}(\mathbf{r})$ terms in Equation (3.16) are the coefficients of the time-harmonic components of the scattered field and yield a background-free near-field signal for $n > 2$. The near-field amplitude $s_{\mathrm{sca},n}$ and phase $\phi_{\mathrm{sca},n}$ can be reconstructed from the near-field hologram $I_n(\mathbf{r})$ by Fourier transform (FT) filtering. The FT of the near-field hologram (calculated from Equation (3.16)) is given by [105]

$$I_{\mathrm{det},n}(\mathbf{q}) = C_n(\mathbf{q}) + s_{\mathrm{ref}} E^*_{\mathrm{sca},n}\left(\mathbf{k}_{\parallel} - \mathbf{q}\right) + s^*_{\mathrm{ref}} E_{\mathrm{sca},n}\left(\mathbf{k}_{\parallel} + \mathbf{q}\right), \quad (3.17)$$

where C_n is the nth order autocorrelation term i.e., FT of $\sum_{l=-\infty}^{\infty} E_{\mathrm{sca},l+n}(\mathbf{r})\, E^*_{\mathrm{sca},l}(\mathbf{r})$, while $s_{\mathrm{ref}} E^*_{\mathrm{sca},n}$ and $s^*_{\mathrm{ref}} E_{\mathrm{sca},n}$ are the direct and conjugate terms, shifted by $-\mathbf{k}_{\parallel}$ and $\mathbf{k}_{\parallel}$, respectively. The direct term $s_{\mathrm{ref}} E^*_{\mathrm{sca},n}$ can be isolated from the other terms by applying an FT filter. Background-free near-field amplitude and phase images can be obtained by simply filtering the direct term and performing an inverse FT of the direct term for $n > 2$.

An example of near-field SOH imaging with an infrared gap antenna (rod length $l = 2.9\,\mu\mathrm{m}$, gap width $w = 50\,\mathrm{nm}$) is shown in Figures 3.5b-g. Figures 3.5b-c show the topography and the simultaneously recorded near-field hologram $I_4(\mathbf{r})$, respectively. The FT of the hologram in Figure 3.5c is shown in Figure 3.5d. The autocorrelation term C_4(center of FT shown in Figure 3.5d), as well as the direct $s_{\mathrm{ref}} \tilde{E}^*_{\mathrm{sca},4}$ (top of Figure 3.5d) and conjugate $s^*_{\mathrm{ref}} \tilde{E}_{\mathrm{sca},4}$ terms can be clearly seen in the FT. The direct term

is isolated (Figure 3.5e) by applying an FT filter indicated by the red dashed box in Figure 3.5d. By performing an inverse FT transform of the direct term, the background-free near-field amplitude $s_{\mathrm{sca},4}$ and phase $\phi_{\mathrm{sca},4}$ images of the antenna are shown in Figures 3.5f, g, respectively. The reconstructed near-field images reveal the fundamental dipolar resonance of the antenna, which is characterized by strong fields at the rod extremities that oscillate $180°$ out of phase [26].

Note that isolating the direct term $s_{\mathrm{ref}} E^*_{\mathrm{sca},n}$ allows for effective elimination of the multiplicative background discussed in Section 3.3.3 [26], as it is only contained in the autocorrelation term C_n (see Equation (3.17)). SOH's technical simplicity and efficacy in isolating and removing multiplicative background signals thus allows for reliable background free amplitude and phase mapping in s-SNOM.

3.4.3. Nanoscale resolved Fourier transform infrared (nano-FTIR) spectroscopy

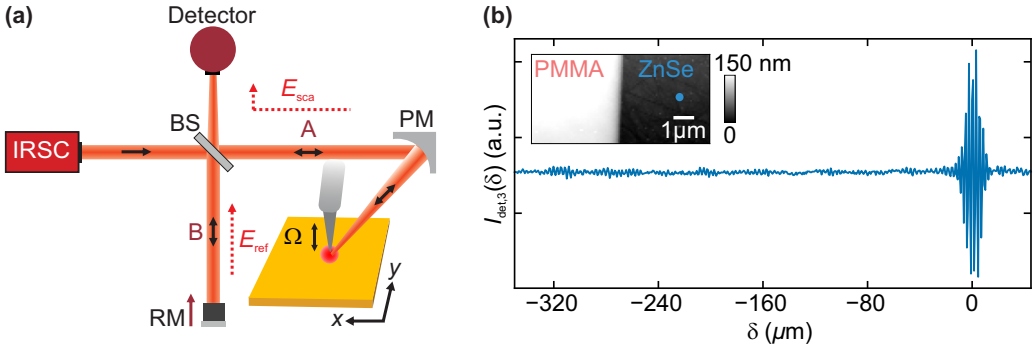

Figure 3.6.: **Illustration of nano-FTIR setup and recorded interferogram.** (a) The nano-FTIR spectroscopy setup, where the tip is illuminated using an infrared supercontinuum (IRSC) broadband laser. The backscattered light is analyzed with an asymmetric Fourier transform spectrometer. BS, beamsplitter; PM, parabolic mirror; RM, linearly translating reference mirror. (b) Nano-FTIR interferogram $I_{\mathrm{det},3}(\delta)$ recorded on a ZnSe substrate (blue dot in the the figure's inset showing the sample topography, where a $125\,\mathrm{nm}$ thick PMMA film is spin coated on a ZnSe substrate).

Nano-FTIR [16] spectroscopy is an advanced technique in s-SNOM that combines the chemical sensitivity of FTIR spectroscopy [45] with the high spatial resolution of atomic force microscopy (AFM) to achieve nanoscale-resolved chemical identification of diverse materials [22, 106], including biological samples [17] and polymers [15, 107]. Unlike the imaging modes discussed above, nano-FTIR utilizes a broadband source to illuminate the tip, allowing for spectral analysis at the nanoscale.

Figure 3.6a illustrates a typical nano-FTIR setup. Analogous to s-SNOM imaging, nano-FTIR spectroscopy relies on an asymmetric Michelson interferometer, where the tip and the sample are placed in one of the interferometer arms (A). The tip is illuminated using a broadband infrared supercontinuum (IRSC) laser. The tip-scattered light is analyzed using an asymmetric Fourier transform spectrometer, which is essentially a Michelson interferometer fitted with a linearly translating reference mirror (RM) [16,18]. To suppress background contributions, the detector signal is demodulated at higher harmonics $n\Omega$ ($n \geq 2$) of the tip oscillation frequency Ω. This asymmetric detection scheme enables the simultaneous measurement of both the amplitude and phase of the complex-valued tip-scattered field [14,16].

Linearly translating the reference mirror (RM) and recording the demodulated detector signal $I_{\mathrm{det},n}$ as a function of mirror position δ yields an interferogram $I_{\mathrm{det},n}(\delta)$. An example interferogram, recorded on a ZnSe substrate is shown in Figure 3.6b. The interferogram predominantly exhibits fast oscillations superimposed on an exponentially decaying envelope, reaching a maximum at the white light position (WLP). The WLP corresponds to the case where both arms of the interferometer have equal optical lengths, resulting in constructive interference across all frequencies, maximizing the detected signal. The near-field spectrum $I_{\mathrm{det},n}(\omega)$ can then be obtained by performing a Fourier transform of the complex valued interferogram $I_{\mathrm{det},n}(\delta)$, where ω represents the spectral frequency.

Background suppression in nano-FTIR spectroscopy

As in s-SNOM imaging, to suppress the background signal, the detector signal is demodulated at higher harmonics $n\Omega$ of the tip oscillation frequency Ω. Using Equation (3.11), the nth harmonic of the complex valued interferogram $I_{\mathrm{det},n}(\delta)$ can be approximated by [108]

$$I_{\mathrm{det},n} \propto s_{\mathrm{nf},n}\left[s_{\mathrm{bg},0}\cos\left(\phi_{\mathrm{nf},n}-\phi_{\mathrm{bg},0}\right)+s_{\mathrm{ref}}\cos\left(\phi_{\mathrm{nf},n}-\phi_{\mathrm{ref}}\right)\right], \tag{3.18}$$

where ϕ_{ref} denotes the reference phase, $s_{\mathrm{nf},n}$, $\phi_{\mathrm{nf},n}$, and $s_{\mathrm{bg},0}$, $\phi_{\mathrm{bg},0}$ denote the amplitude and phase of the near-field and background signals, respectively. An interferogram $I_{\mathrm{det},n}(\delta)$ is recorded by linearly translating the reference mirror. By performing a Fourier transform of the complex valued interferogram $I_{\mathrm{det},n}(\delta)$, the complex valued spectra for $\phi_{\mathrm{ref}} = 2\pi\omega\delta$ is given by:

$$I_{\mathrm{det},n}(\omega) = \int_0^\infty s_{\mathrm{nf},n}\left[s_{\mathrm{bg},0}\cos\left(\phi_{\mathrm{nf},n}-\phi_{\mathrm{bg},0}\right)+s_{\mathrm{ref}}\cos\left(\phi_{\mathrm{nf},n}-2\pi\omega\delta\right)\right]\mathrm{d}\delta. \tag{3.19}$$

Only the first term in Equation (3.19) contains background contributions, which are independent of the mirror position δ. This implies that the background terms are

restricted to the part of the spectrum at $\omega = 0$. Thus, for $\omega > 0$, background free nano-FTIR spectrum

$$I_{\mathrm{det},n}(\omega) \propto s_{\mathrm{nf},n}(\omega)\, e^{i\phi_{\mathrm{nf},n}(\omega)} \tag{3.20}$$

can be obtained for signal demodulated at a sufficiently high harmonic ($n\Omega$ for $n \geq 2$).

Practical aspects in nano-FTIR spectroscopy

Unlike Equation (3.19), in practical applications the reference mirror cannot be translated over an infinite distance. The finite translation range $\delta_{\max}$ of the reference mirror limits the spectral resolution to $\Delta\omega_{\min} = \frac{10^4}{2\delta_{\max}}$ [108]. For instance, with a maximum mirror translation $\delta_{\max} = 800\,\mu\mathrm{m}$ (i.e., maximum interferogram length of the nano-FTIR setup discussed here), the spectral resolution is limited to $\Delta\omega_{\min} = 6.25\,\mathrm{cm}^{-1}$. The finite length of the interferogram leads to artificial oscillations or ringing in the spectra, which can be mitigated by multiplying the interferogram by appropriate apodization (window) functions. Another limitation arises from the finite sampling of the recorded interferograms, which leads to a decrease in the spectral resolution. Zero-filling is often used to improve visibility of spectral features in the recorded spectra. Detailed processing steps are elaborated in References [45, 108].

Normalization of nano-FTIR spectra

To remove the influence of instrumental and environmental factors (such as the detector responsivity, beamsplitter efficiency, CO_2 and water vapor absorption) from the recorded spectra, the nano-FTIR spectra must be normalized against a reference sample that exhibits a flat spectral response in the mid-IR region. Normalization allows for accurate comparison between spectra recorded during different experiments, ensuring that the observed differences are caused by chemical variations rather than sample inconsistencies.

Figure 3.7 illustrates this normalization process. Figure 3.7a shows the nano-FTIR interferograms recorded on Poly(methyl methacrylate) PMMA (red) and a ZnSe substrate (blue). Figure 3.7b shows the corresponding nano-FTIR amplitude spectra obtained by Fourier transformation of the interferogram shown in Figure 3.7a. The PMMA spectrum is normalized to the spectrum recorded on ZnSe according to

$$\frac{I_{\mathrm{det},n}^{\mathrm{PMMA}}(\omega)}{I_{\mathrm{det},n}^{\mathrm{ZnSe}}(\omega)} \propto \frac{\sigma_{\mathrm{nf},n}^{\mathrm{PMMA}}(\omega)}{\sigma_{\mathrm{nf},n}^{\mathrm{ZnSe}}(\omega)} = \frac{s_{\mathrm{nf},n}^{\mathrm{PMMA}}(\omega)}{s_{\mathrm{nf},n}^{\mathrm{ZnSe}}(\omega)} \exp\left(i\phi_{\mathrm{nf},n}^{\mathrm{PMMA}}(\omega) - i\phi_{\mathrm{nf},n}^{\mathrm{ZnSe}}(\omega)\right), \tag{3.21}$$

yielding normalized near-field amplitude $s_{\mathrm{nf},3}^{\mathrm{PMMA}}/s_3^{\mathrm{ZnSe}}$ and phase $\phi_{\mathrm{nf},3}^{\mathrm{PMMA}} - \phi_{\mathrm{nf},3}^{\mathrm{ZnSe}}$ spectrum of PMMA.

The third harmonic of the normalized amplitude and phase spectra of PMMA is shown in Figure 3.7c and 3.7d, respectively. The normalized amplitude spectrum exhibits a dispersive behavior, while the normalized phase spectrum shows a peak at $1735\,\mathrm{cm}^{-1}$, corresponding to the absorption associated with the $\mathrm{C}=\mathrm{O}$ stretching in PMMA. The nano-FTIR phase spectra of organic samples correspond well with far-field FTIR absorption spectra [16, 18, 109], facilitating material characterization and identification using standard FTIR references [110]. The ability to resolve chemical composition with nanoscale resolution has made nano-FTIR an invaluable tool in numerous investigative avenues in materials science, biology, and polymer research.

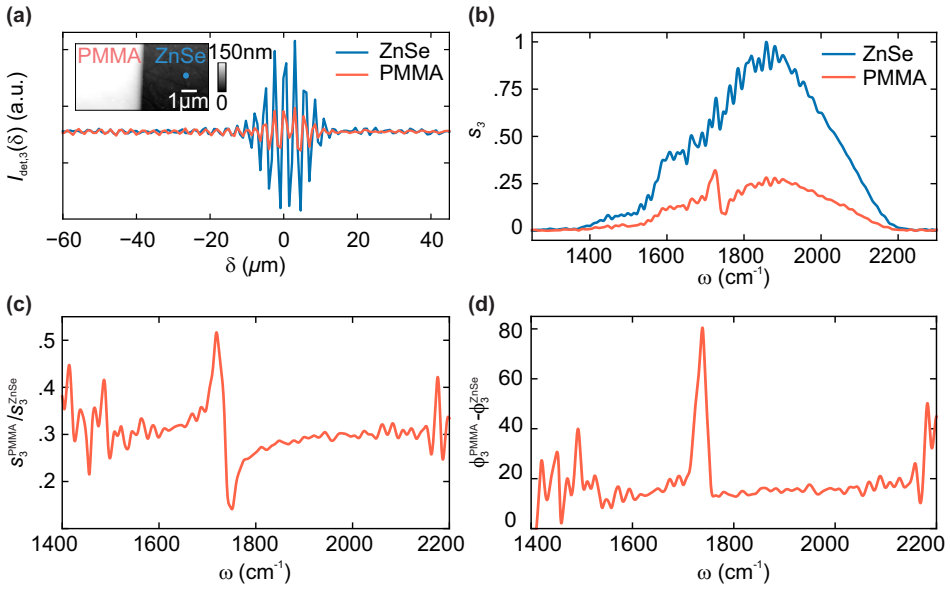

Figure 3.7.: **Normalization of nano-FTIR spectra.** (a) Interferograms, zoomed near the white light position (WLP), recorded on ZnSe(blue) and PMMA(red). The inset shows the topography of a 125 nm thick PMMA film on a ZnSe substrate. (b) Near-field amplitude spectra $s_{\mathrm{nf},3}^{\mathrm{PMMA}}$(red) and $s_{\mathrm{nf},3}^{\mathrm{ZnSe}}$(blue) obtained by Fourier transform of interferograms in panel (a). (c) Normalized near-field amplitude $s_{\mathrm{nf},3}^{\mathrm{PMMA}}/s_{\mathrm{nf},3}^{\mathrm{ZnSe}}$ and (d) phase $\phi_{\mathrm{nf},3}^{\mathrm{PMMA}} - \phi_{\mathrm{nf},3}^{\mathrm{ZnSe}}$ spectrum of PMMA.

3.5. Side illumination s-SNOM and nano-FTIR for operation in air

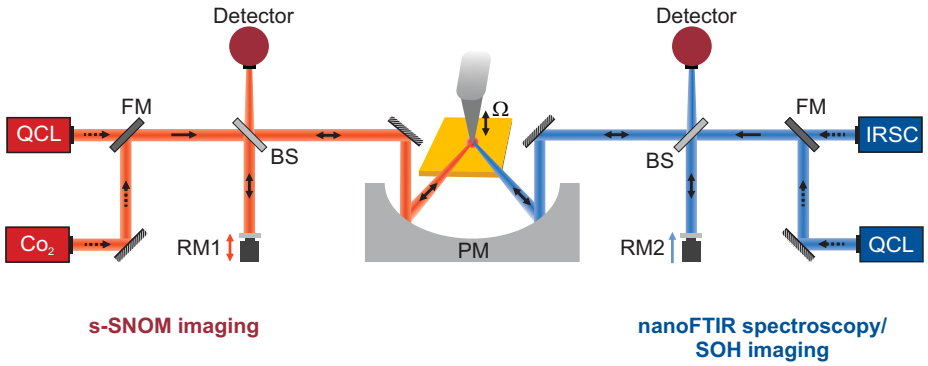

Figure 3.8.: **Illustration of s-SNOM, SOH, and nano-FTIR setup.** For s-SNOM imaging, the tip is illuminated with either a frequency-tunable quantum cascade laser (QCL) or a CO_2 laser. The backscattered light is demodulated at higher harmonics of the tip's oscillation frequency, $n\Omega$, and recorded with a pseudo-heterodyne Michelson interferometer (left). BS, beamsplitter; RM1, piezo-actuated vibrating mirror; FM, flip mirror. For SOH imaging (right), the tip is illuminated with a monochromatic light source such as a frequency-tunable QCL laser. For nano-FTIR, the tip is illuminated with an infrared supercontinuum (IRSC) broadband laser. The backscattered light is analyzed using an asymmetric Fourier transform spectrometer (right). RM2, piezo-actuated translating mirror. Figure adapted from Reference [111].

Here we describe a standard side illumination s-SNOM setup (neaSNOM, Attocube systems AG) . In this work, this setup was modified to enable s-SNOM and nano-FTIR measurements in a liquid environment. The necessary instrumental development is described in detail in Chapter 4.

Figure 3.8 illustrates a side illumination s-SNOM setup for infrared nanoimaging and nanospectroscopy in air. The setup can be broadly divided into two sub-systems: one for nanoimaging and the other for nanospectroscopy.

For nanoimaging, the s-SNOM setup can be operated in two configurations: pseudo-heterodyne (left side of Figure 3.8) and synthetic optical holography SOH (right side of Figure 3.8). For both configurations, monochromatic illumination is provided either by a CO_2 gas laser (Access Laser Merit-G) or a frequency-tunable quantum cascade laser (QCL, Daylight Solutions Inc.). The light is focused onto a commercially available metal-coated AFM tip using a parabolic mirror (PM). A piezo actuator is used to oscillate the AFM tip with frequency Ω. Due to the tip-sample near-field interaction

(Section 3.3.2), the tip-scattered light is modulated at higher harmonics $n\Omega$ of the oscillation frequency. It is collected by a Michelson interferometer equipped with either a piezo-actuated vibrating mirror (RM1 for pseudo-heterodyne imaging) or a linearly translating reference mirror (RM2 for SOH). The scattered light is detected by an MCT detector (InfraRed Associates, Inc.). The detector signal is recorded using a fast data acquisition card and the NeaSNOM software processes and demodulates the signal yielding amplitude s_n and phase ϕ_n images of the sample.

For nanospectroscopy (nano-FTIR, shown on the right side of Figure 3.8), the AFM tip is illuminated with a broadband infrared radiation from a difference frequency-generated laser supercontinuum (frequency range $= 1200 - 1700\,\mathrm{cm}^{-1}$, average power: $500\,\mu\mathrm{W}$). Similar to nanoimaging the modulated tip-scattered light is collected with a Michelson interferometer, where the reference mirror (RM2) is translated linearly to record an interferogram. The neaSNOM software processes the interferogram according to Section 3.4.3 yielding the amplitude $s_n^{\mathrm{sam}}(\omega)$ and phase $\phi_n^{\mathrm{sam}}(\omega)$ spectra of the sample. The sample spectra are normalized against a reference spectra (recorded on the substrate) according to the Equation (3.21).

4. Instrumental development for infrared s-SNOM and nano-FTIR in a liquid environment

Infrared scattering-type near-field optical microscopy (IR s-SNOM) and nanoscale-resolved Fourier transform infrared (nano-FTIR) spectroscopy are powerful, label free techniques for characterization and identification of a wide range of materials, including polymers, biomaterials, semiconductors, metallic nanoparticles, and 2D materials with nanoscale resolution. Extending these techniques to liquid environments could provide unprecedented insights into bio-chemical processes, crystal growth, material sciences, and molecular sensing. However, the development of in-situ IR s-SNOM and nano-FTIR has remained a significant challenge due to water's strong IR absorption and challenges associated with the tapping mode AFM operation in liquid. In this chapter, we describe two novel s-SNOM techniques developed during this thesis, enabling amplitude- and phase-resolved nanoimaging and nanospectroscopy in liquid environments. These advancements open new possibilities for in-situ nanoscale study of materials and processes in their native liquid state. Some parts of the results presented in this chapter were previously published in Reference [112].

4.1. Introduction

Nanoscale-resolved studies of molecular interactions and dynamic processes in liquid environments could provide valuable insights into fundamental processes in biological systems, chemical reactions, (nano)biomolecular engineering, and material research. However, developing scattering-type scanning near-field optical microscopy (s-SNOM) and nanoscale resolved Fourier transform infrared (nano-FTIR) spectroscopy techniques for operation in liquid environments has remained significantly challenging, primarily due to the strong absorption of infrared (IR) radiation by water and the complexities associated with tapping mode atomic force microscopy (AFM) operation in liquids. Initially, mid-IR s-SNOM experiments with samples in liquid relied on graphene/SiN-based liquid cells, where the liquid is covered by a thin IR transparent membrane while the s-SNOM is operated in air. These ultrathin membranes have enabled nanospectroscopy of living cells and nanoparticles in liquid environments [35–40]. However,

membrane-based liquid cells often require complex sample preparation and may exert pressure on the encapsulated samples [35, 113, 114], potentially distorting the topographical information. Additionally, fluctuations in the volume of the encapsulated water can create artifacts impacting the image contrast [35].

More recently and parallel to the results presented in this thesis, IR s-SNOM where both the near-field probe and the samples were immersed in liquid was demonstrated for organic materials [41, 42]. This in-situ near-field optical microscopy approach has the potential to allow imaging of bio(chemical) samples in physiological environments while minimizing near-field interactions between the samples and the membranes that cover them. However, IR s-SNOM and nano-FTIR spectroscopy in liquid remain underdeveloped due to various technical and scientific challenges. For instance, complex beam shapes are often necessary for normal incidence illumination, allowing for nanoimaging but complicating spectroscopy [42]. Conversely, a total internal reflection (TIR)-based geometry has been successfully demonstrated for nanospectroscopy, but is deemed challenging for nanoimaging due to effective beam path change during scanning [41].

Beyond s-SNOM, nanoscale-resolved IR nanoimaging in liquid has also been achieved using techniques such as photothermal expansion (PTE) microscopy and photoinduced force microscopy (PiFM) [115–118]. These methods detect the IR absorption of a sample non-optically by monitoring changes in the cantilever oscillation caused by the photothermal expansion of the sample. However, the interferometric detection scheme of s-SNOM provides several advantages over these techniques, as discussed previously in Chapter 3.

In this Chapter, we outline the development and implementation of two novel instrumental approaches enabling s-SNOM imaging and nano-FTIR spectroscopy in liquid environments. We begin by discussing the underlying concept (Section 4.2) and experimental implementation (Section 4.3) of our techniques. This includes a detailed discussion of AFM operation in liquid (Section 4.3.1), followed by the implementation of two illumination and collection schemes: the normal incidence/collection transflection setup (Section 4.3.2) and the TIR-based setup (Section 4.3.3) for s-SNOM and nano-FTIR in liquids. We apply the transflection s-SNOM for mapping localized plasmon polaritons in metal antennas in liquid in Section 4.4. Subsequently, in Section 4.5, we demonstrate the application of TIR-based s-SNOM for chemical nanoimaging and nanospectroscopy in liquids.

4.2. Concept

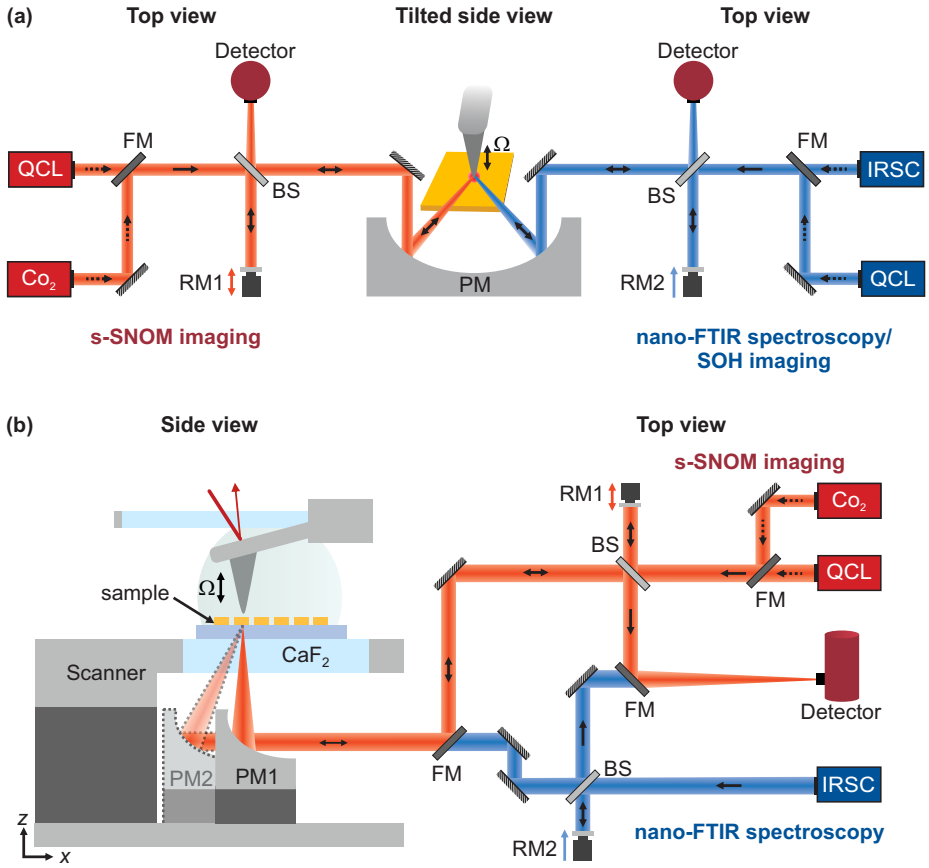

Figure 4.1.: **Schematic representation of the bottom illumination and detection scheme for IR s-SNOM nanoimaging (red) and nanospectroscopy (blue) in liquid.** A schematic of the two illumination and detection schemes designed for amplitude- and phase-resolved s-SNOM (red) and nano-FTIR (blue) in a liquid environment. In the first scheme, the sample is illuminated from either a monochromatic (red) or a broadband (blue) source under normal incidence using a parabolic mirror (PM1). In the second scheme, the sample is illuminated from either a monochromatic (red) or a broadband (blue) source with totally internally reflected light from a ZnSe wedge (not shown here, see Figure 4.9) using a second parabolic mirror (PM2). BS, beamsplitter; FM, flip mirror; RM1, piezo actuated vibrating mirror; RM2, piezo actuated translating mirror; QCL, frequency-tunable quantum cascade laser; IRSC, infrared supercontinuum broadband laser.

s-SNOM and nano-FTIR are advanced AFM-based techniques that enable amplitude- and phase-resolved optical characterization of diverse samples with nanoscale resolution.

Before discussing the instrumental development for liquid environments, it is crucial to understand the fundamental principles underlying s-SNOM and nano-FTIR. These principles are rooted in the interaction between light, the AFM tip, and the sample, which are essential for achieving precise optical measurements. A detailed discussion of these fundamental working principles of s-SNOM is presented in Chapter 3.

Figure 4.1a illustrates a typical s-SNOM setup for amplitude- and phase-resolved nanoimaging (s-SNOM or synthetic optical holography (SOH)) and nanospectroscopy (nano-FTIR) in air. In this configuration, the AFM tip is illuminated at an angle of 60° relative to the tip axis using an off-axis parabolic mirror (PM), and the back-scattered light is collected by the same parabolic mirror. However, such side-illumination geometry is unsuitable for operation in liquid environments, particularly at infrared frequencies, due to the strong absorption of infrared light by water and other liquids.

To facilitate s-SNOM and nano-FTIR measurements of samples immersed in liquids with the AFM also operating in liquid (as opposed to membrane-based liquid cells [35–40]), it is essential to adopt an illumination and detection scheme that minimizes the optical path through the liquid medium. To address this, we implement a bottom illumination and detection scheme for s-SNOM, as illustrated in Figure 4.1b. In this setup, the IR beam is focused onto the tip apex using an off-axis parabolic mirror (PM) through a substrate and a sample holder window made of $\mathrm{CaF_2}$. We chose $\mathrm{CaF_2}$ as the window material in our setup since it is transparent to both visible and infrared light, facilitating precise alignment of the IR light from laser sources to the tip and subsequently to the detector. For alignment purposes, the IR beam in our setup is guided by overlapping it with a pilot laser (HeNe, $\lambda = 633\,\mathrm{nm}$) as a visual reference.

To conduct nanoimaging and nanospectroscopy in liquids, we employed an open liquid cell, described in detail in Section 4.3, consisting of a droplet of water confined between the sample and a transparent window above the AFM cantilever (see Figure 4.1b). The transparent ($\mathrm{CaF_2}$) window is integrated into the cantilever holder to optimize the AFM and, consequently, s-SNOM performance in liquid. The AFM operation in liquid is elaborated in Section 4.3.1.

We propose two distinct bottom illumination and detection schemes for operation in liquid. In the first scheme (transflection s-SNOM setup), the tip is illuminated under normal incidence (i.e., perpendicular to the sample surface) while the back-scattered light is collected in a transflection configuration (see Figure 4.1b). A detailed discussion of the implementation of the transflection setup in air and liquid environments, along with its advantages and disadvantages, will be provided in Section 4.3.2. In the second scheme (TIR s-SNOM setup), the tip is illuminated via the totally internally reflected (TIR) beam at the substrate-liquid or substrate-air interface. A comprehensive discussion of the working principle and implementation of TIR-based s-SNOM in liquid will be elaborated in Section 4.3.3.

4.3. Implementation

To enable amplitude- and phase-resolved nanoimaging and nanospectroscopy in liquid environments, we developed two novel instrumental approaches. Our implementations consist of the transflection and TIR-based s-SNOM techniques, both of which are based on a commercial s-SNOM (neaSNOM) setup from Neaspec, Attocube Systems AG. To facilitate the operation of this setup in a liquid environment (illustrated in Figure 4.1b), we modified the cantilever and sample holders, along with adjustments to the illumination and collection schemes, as summarized in Section 4.2. Some of these modifications were made in collaboration with Neaspec. In this section, we present a detailed description and implementation of the modified setup.

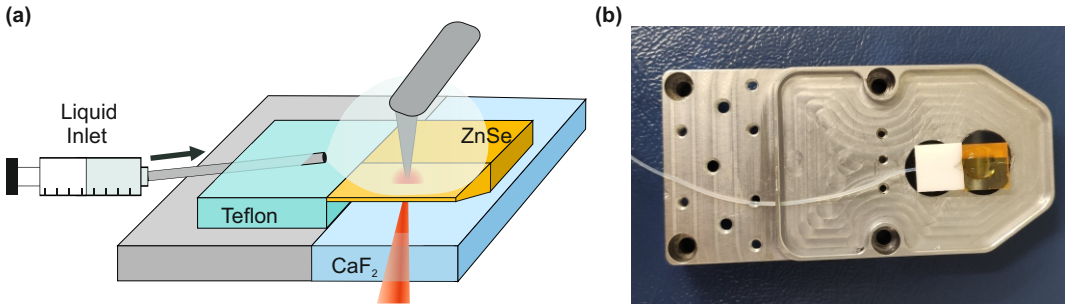

Figure 4.2.: **Open liquid cell concept for s-SNOM and nano-FTIR.** (a) Schematic of the liquid cell and (b) an image of the sample holder showing the formation of a liquid droplet on a $ZnSe$ wedge. The droplet can be easily refilled by injecting a small quantity of liquid through a tube connected to the substrate. This concept is similarly applied for for both transflection and TIR-based s-SNOM measurements.

To facilitate the setup's operation in liquid, we implemented an open liquid cell (see Figure 4.2). The sample is securely mounted to the CaF_2 window on the sample table (Figure 4.3a) using double-sided carbon tape (Figure 4.2b). An electrically conductive carbon tape is employed to minimize charge accumulation on the AFM tip, which is a common issue when working with insulating substrates (for instance, the sample holder window is made from the insulating material CaF_2) [119,120]. Charge accumulation can degrade AFM performance, often preventing the AFM tip from making contact with the sample during the tapping cycle. Notably, increasing ambient humidity can also mitigate charge accumulation, which tends to affect measurements in air [119].

A droplet of liquid is placed directly on the CaF_2 or wedged $ZnSe$ substrate, and it can be replenished by injecting additional liquid from a syringe connected via a tube to a Teflon

(Polytetrafluoroethylene) block, which is in direct contact with one edge of the substrate. This design allows for convenient refilling of the droplet between measurements (see Figure 4.2).

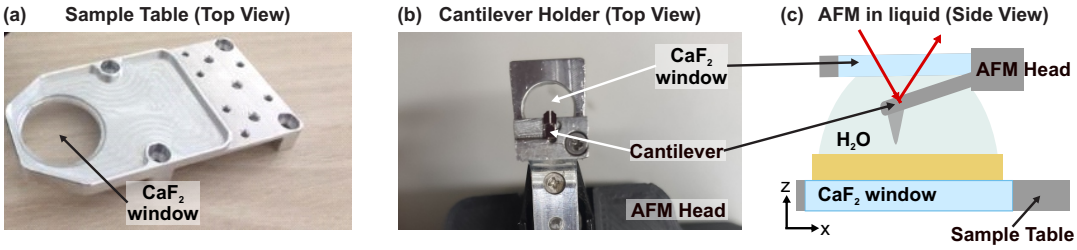

Figure 4.3.: **Modified cantilever and tip holder for s-SNOM operation in liquids.** (a) Sample table integrated with a CaF_2 window to facilitate illumination and collection from below the sample. (b) Cantilever holder integrated with a CaF_2(IR transparent) window for optimal detection of the deflection laser as part of the AFM operation. (c) Schematic representation of the AFM tip in an open liquid cell.

For AFM and s-SNOM operation in liquid, an AFM tip (Si tip coated with either $Pt-Ir$ (Arrow NCPt, Nanoworld) or Au (PPP-NCSTAu, Nanosensors)) is affixed to the modified cantilever holder using thermal glue (Figure 4.3b). A CaF_2 window is integrated into the cantilever holder to ensure optimal detection of the deflection laser within the liquid medium. The deflection laser is focused through this CaF_2 window onto the backside of the cantilever and the reflected beam is detected as part of the AFM operation (for a detailed description of AFM operation in liquid, see Section 4.3.1). The sample is brought close to the AFM tip until the droplet of water is uniformly squeezed between the sample and the transparent window above the AFM cantilever (see Figure 4.1 and 4.3c). This open liquid cell enables stable s-SNOM operation in liquid. A detailed protocol for AFM and s-SNOM operation in liquid specific to this setup can be found in Appendix A.

In this thesis, we utilize either deionized (DI) water (H_2O) or heavy water (D_2O) (99.9 atom % D, Sigma-Aldrich). We substitute H_2O with D_2O when extended measurement times are necessary. This substitution is advantageous because the IR absorption in D_2O is lower than that in H_2O [121,122] within the frequency range of the broadband laser emission ($1200-2100\,cm^{-1}$, essential for the polariton and dielectric mapping shown in this work). The reduced absorption in D_2O minimizes the rate of evaporation of the liquid, thus enhancing the stability of AFM operation.

4.3.1. AFM in liquid

In this section, we describe the operation of tapping mode AFM in liquid, which serves as the foundation for s-SNOM and nano-FTIR measurements. The working principle of AFM, specifically tapping mode AFM, has been previously discussed in Chapter 3, Section 3.2. A schematic of the tapping mode AFM setup operated in liquid is shown in Figure 4.4. We employ an open liquid cell (see Figure 4.3c), where a droplet of liquid held between the sample surface and the CaF_2 window integrated in the cantilever holder serves as the imaging medium. This CaF_2 window minimizes spurious reflections from the liquid droplet's meniscus, allowing for efficient focusing and detection of the deflection laser, which is crucial for accurate AFM detection in liquid. A detailed protocol for loading and operating the liquid cell is provided in Appendix A.

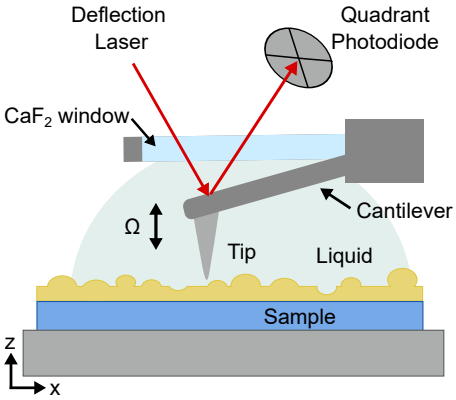

Figure 4.4.: **Schematic of tapping mode AFM in liquid.** The open liquid cell concept allows both the sample and cantilever to be fully immersed in liquid during imaging. The cantilever movement is monitored by recording the reflection of the deflection laser focused on the back of the cantilever using a position-sensitive quadrant photodiode.

In tapping mode AFM, a piezoelectric actuator is commonly used to acoustically excite the cantilevered tip by applying a sinusoidal voltage to the drive piezo [56]. The cantilever is oscillated at a fixed frequency, typically near its fundamental resonant frequency. The oscillation amplitude is sensitive to the tip-sample interaction and decreases as the tip approaches the sample surface. This oscillation amplitude serves as a feedback parameter, enabling the monitoring of changes in the sample's topography while the sample is raster-scanned beneath the tip. Figure 4.5a shows a typical frequency response spectrum of a $Pt-Ir$ coated Si tip (Arrow NCPt, Nanoworld) measured in air, revealing a distinct sharp peak, with a zoom-in shown in Figure 4.5b, corresponding to its fundamental resonant frequency.

In contrast, when operating in liquid, the acoustic excitation of the cantilever leads to a frequency response that is characterized by multiple peaks, commonly referred to as a "forest of peaks" [123]. Figure 4.5c shows the measured frequency response of the same cantilevered tip (as presented in Figure 4.5a) now immersed in liquid (specifically H_2O). The appearance of these additional peaks can be attributed to the acoustic vibrations of the liquid surrounding the cantilever, which can also drive the cantilever. Consequently, the frequency response of the cantilever in liquid can be approximated as a convolution of the true cantilever resonance and the complex fluid drive spectrum of the liquid cell. This combined response is influenced not only by the intrinsic properties of the cantilever but also by the geometry and dynamics of the liquid cell itself [123, 124].

The presence of these additional sharp peaks (see example in Figure 4.5c) complicates the selection of the appropriate driving frequency for effective operation in liquid. To navigate this complexity, one must first identify a strong low-frequency peak specific to the particular cantilever-liquid cell setup being used. This involves a careful analysis of the frequency response spectrum to discern which peaks correspond to useful resonant modes for excitation while filtering out the less relevant or spurious peaks. Once the optimal driving frequency is determined, it serves as a reliable reference for future measurements in liquid environments. The detailed protocol for selecting the driving frequency, along with guidance for adjusting the imaging parameters in liquid, is outlined in Appendix A.

The presence of liquid significantly influences two key cantilever resonance parameters: the resonance frequency f_0 and the quality factor $Q \approx \frac{f_0}{\Delta f}$ (see Figure 4.5b), where Δf is the bandwidth of the resonance, i.e., Full Width at Half Maximum (FWHM). The quality factor Q is a dimensionless quantity that gives a measure of the damping in the cantilever oscillation. Both f_0 and Q influence how quickly the tip responds to changes in the sample's topography. In liquid, both the resonance frequency and the quality factor are reduced. Specifically, the resonant frequency (f_0) can decrease to approximately one third of its value in air, with $f_0^{H_2O} \approx \frac{1}{3} f_0^{air}$, due to the increased effective mass of the cantilever in liquid (which occurs as a result of the cantilever dragging the surrounding liquid during oscillations) [123, 125]. For instance, in our liquid cell, the resonant frequency of a $Pt-Ir$ tip recorded in air $f_0^{air} \approx 268\,kHz$ shifts to roughly $f_0^{H_2O} \approx 108\,kHz$ in H_2O (see Figures 4.5b, d). A detailed protocol for selecting the driving frequency is provided in Appendix A.

Moreover, the hydrodynamic damping in liquid broadens the resonance peak, leading to a significant reduction in the quality factor Q. For our system, the Q factor in liquid is approximately five times lower than in air ($Q^{air} = 525$, $Q^{H_2O} = 28$), see cantilever resonance in air and H_2O in Figures 4.5b, d, respectively. This low Q factor results in anharmonic and asymmetric oscillations of the cantilever, which can enhance the force exerted by the tip on the sample [126]. Such an increase in tip force, combined

with incorrect selection of the drive frequency, may lead to greater sample damage and deformation in liquid. Therefore, it is crucial to carefully select optimal imaging parameters in liquid to minimize potential sample damage. A detailed description can be found in Appendix A.

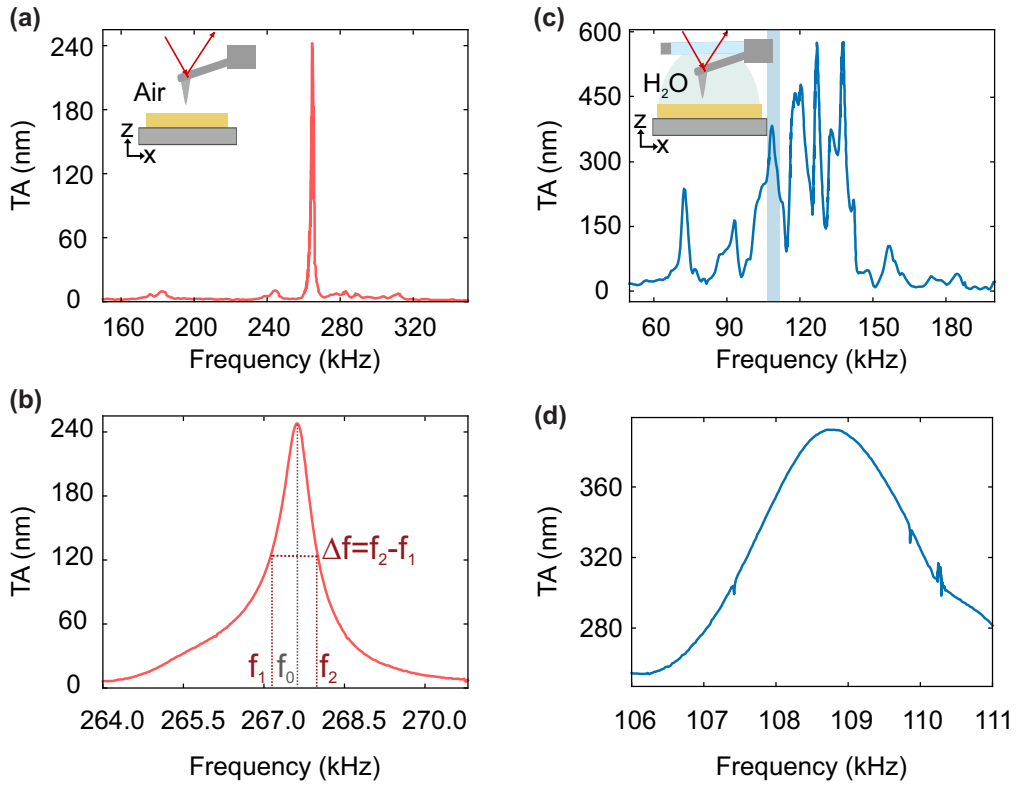

Figure 4.5.: **Comparison of typical frequency response of a cantilevered AFM tip recorded in air and liquid.** (a) Frequency response spectrum of a commercially available $\mathrm{Pt-Ir}$ coated Si AFM tip (NCPt arrow tip, Nanoworld) measured in air. TA, tapping amplitude. (b) Zoom-in of the resonance peak of the cantilever in air. (c) Frequency response spectrum of the same AFM tip (as in panel a) measured in liquid ($\mathrm{H_2O}$). (d) Zoom-in of the selected resonance peak (indicated by shaded region in panel c) for AFM operation in liquid. A detailed protocol for selecting the driving frequency is provided in Appendix A.

To evaluate the performance of our setup in liquid, we recorded a topographical image ($10 \times 10\,\mu\mathrm{m}$) of a TGQ1 calibration grating (NT-MDT Spectrum Instruments Ltd., Ireland), which consists of a 3D array of $\mathrm{SiO_2}$ islands patterned onto a Si wafer. The $\mathrm{SiO_2}$ islands are approximately $20 \pm 1.5\,\mathrm{nm}$ high and $1.5 \pm 0.35\,\mu\mathrm{m}$ wide, with a grating

periodicity of $3 \pm 0.05\,\mu\mathrm{m}$. The topographical image recorded in liquid is shown in Figure 4.6a, revealing a drift-free topography map of the grating structure. This indicates robust AFM performance in liquid. The measured height, width, and separation of the islands corresponds well with the parameters specified by the manufacturer. A representative line scan showing the height data (extracted along the blue line shown in Figure 4.6a) for a SiO_2 island is shown in Figure 4.6b, further confirming the stability and accuracy of our setup in liquid.

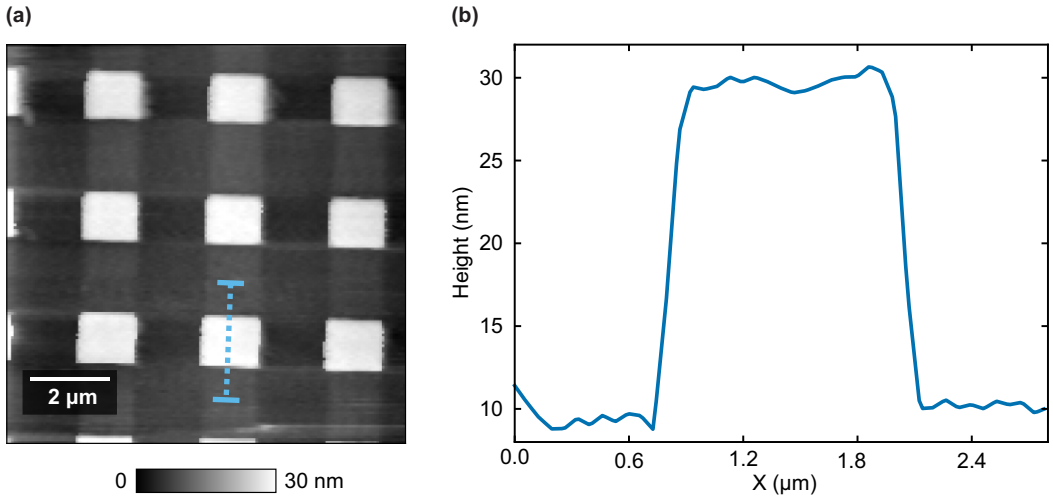

Figure 4.6.: **AFM in liquid.** (a) AFM topography image of the TGQ1 calibration sample, demonstrating the reliable performance of our setup in liquid. (b) Line profile extracted along the horizontal line shown in panel a, revealing the height $h = 20\,\mathrm{nm}$ and width $w = 1.5\,\mu m$ of the SiO_2 islands on the Si substrate. These values match well with the grating specifications provided by the manufacturer.

It is important to note that the AFM setup used in this study remains relatively basic for liquid operation. Future improvements in AFM performance and resolution could be achieved by implementing advanced Q control strategies to increase the quality factor Q of the cantilever oscillation in liquid [127, 128]. Additionally, alternate excitation methods, such as magnetic piezoelectric excitation [129], could be explored to mitigate the appearance of spurious peaks in the cantilever response spectra and improve overall imaging stability.

4.3.2. Transflection illumination and collection geometry

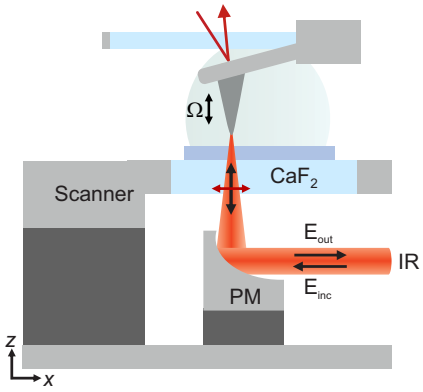

Figure 4.7.: **Normal incidence transflection illumination and collection geometry**. Schematic representation of the transflection setup. The incident light E_{inc} illuminates the tip under normal incidence and the backscattered light E_{out} is collected. The polarization direction of the incident light is indicated by the red double sided arrow. PM, parabolic mirror; Ω, tip oscillation frequency.

In this section, we describe the implementation of the transflection illumination and collection geometry in s-SNOM, specifically designed to minimize the optical path through the liquid medium enabling nanoimaging and nanospectroscopy in liquid environments. A schematic of the normal incidence transflection scheme is shown in Figure 4.7.

In this setup, a $\mathrm{Pt-Ir}$ coated AFM tip (NCPt arrow tip, Nanoworld) is illuminated with a focused IR beam under normal incidence relative to the sample surface using a parabolic mirror ($f = 8\,\mathrm{mm}$, $\mathrm{NA} = 0.44$) through a $\mathrm{CaF_2}$ substrate and sample holder, similar to transmission mode s-SNOM [26, 130]. The parabolic mirror was mounted on a three-axis ($-xyz$) piezo translation stage to enable fine positioning of the laser focal spot. The parabolic mirror and the piezo stage were provided by Neaspec, Attocube Systems AG. A key difference in transflection mode is that we collect the backscattered light transmitted through the substrate using the same parabolic mirror, instead of employing a second parabolic mirror to collect the tip-scattered light above the sample, as in transmission mode.

The transflection geometry is crucial for enabling s-SNOM measurements in liquid environments. By effectively minimizing the optical path of the tip-scattered light in the liquid, it significantly reduces IR absorption (particularly by water, $\mathrm{H_2O}$) and mitigates reflection losses at the liquid droplet meniscus. Furthermore, the backscattered light is recorded as a function of either the tip position (using a standard pseudo-heterodyne interferometer [96]) or the reference mirror position (using an asymmetric

FTIR spectrometer; nano-FTIR [16]) with an MCT detector (see also the schematic in Figure 4.1).

To suppress background contributions, higher harmonic signal demodulation of the detector signal at $n\Omega$ (for $n \geq 2$, where Ω is the tip oscillation frequency) is used, similar to side illumination s-SNOM (described previously in Chapter 3).

Within the s-SNOM community, it is well-established that maximum field enhancement between the tip and the sample occurs when the polarization of the incident light aligns parallel to the long axis of the tip [131, 132]. However, under normal incidence, the polarization of the incident beam remains perpendicular to the long axis of the tip, preventing direct coupling between the probing tip and the IR light. To overcome this limitation, we propose utilizing the transflection geometry to examine nanostructures, such as resonant polaritonic antennas, which can convert the incident electric field into a field possessing a vertical component that is aligned parallel to the tip's long axis.

The transflection geometry offers a two-fold advantage for performing nanoimaging and nanospectroscopy of resonant antennas in a liquid environment. First, normal incidence is an ideal configuration for antenna mapping, as it facilitates efficient excitation of antennas while minimizing tip excitation (since the field polarization is perpendicular to the tip axis), thus reducing distortion of the antenna fields [130,133]. Second, polaritons are well known for their ability to significantly enhance infrared absorption not only in air [134,135] but also in liquid environments [136–138].

While near-field mapping of optical and infrared antennas has been successfully demonstrated in air using transmission mode s-SNOM [26, 130, 139] and side illumination s-SNOM [28,140–142], transflection s-SNOM has not yet been reported. We demonstrate the application of transflection s-SNOM for amplitude- and phase-resolved nanoimaging and nanospectroscopy of the antenna near-fields in both air and liquid environments (Section 4.4 and Chapter 5, respectively). The ability to perform amplitude- and phase-resolved nanoimaging of the antenna near-field distribution is critical for the design and optimization of antennas for future in-situ studies of antenna-enhanced (bio)chemical interactions.

4.3.3. TIR-based s-SNOM

The normal incidence transflection mode in s-SNOM is suitable for scenarios where the near-field is generated by an antenna and the tip serves exclusively as a scattering probe. However, for applications such as dielectric mapping, chemical identification [15, 16, 21, 143], and imaging ultraconfined polaritons in 2D materials [30, 31], efficient coupling of the incident light with the tip is essential to generate concentrated near fields at the tip apex.

To overcome the limitations of the transflection setup, we developed a TIR-based illumination and collection geometry in s-SNOM. This setup enables efficient coupling of the incident light with the tip, enabling nanoimaging and nanospectroscopy of diverse sample systems.

TIR occurs when light traveling from an optically denser medium strikes the interface with an optically rarer medium at an angle greater than the critical angle θ_c. Let medium 1 be the optically denser medium with refractive index n_1 and medium 2 the optically rarer medium with refractive index n_2, such that $n_1 > n_2$. The light is totally internally reflected back into medium 1 when the angle of incidence θ exceeds the critical angle θ_c (i.e., $\theta \geq \theta_c$). The critical angle can be calculated using Snell's law: $n_1 \sin\theta_1 = n_2 \sin\theta_2$. By setting the angle of refraction $\theta_2 = 90°$, the critical angle θ_c is defined as [6]

$$\theta_c = \sin^{-1}\left(\frac{n_2}{n_1}\right). \tag{4.1}$$

Above the critical angle θ_c, no propagating fields exist in the optically rarer medium (medium 2). However, an evanescent field is generated that extends perpendicular to the interface of the two media (in medium 2). This evanescent field decays exponentially with increasing distance from the interface. Notably, the electric field of the evanescent wave is oriented vertically, i.e., parallel to the tip axis, which is crucial for efficient coupling with the AFM tip. The decay length of the evanescent field into medium 2, defined as the distance at which the field strength has decayed to $1/e$ of its maximum intensity, can be calculated as follows [45]:

$$\gamma = \frac{\lambda}{2\pi n_1 \sqrt{\sin^2\theta - (n_2/n_1)^2}}, \tag{4.2}$$

where λ is the wavelength of the incident light. This decay length depends on the angle of incidence and the refractive indices of both media. Typically, in the infrared region, the decay length is of the order of $0.5 - 2\,\mu\mathrm{m}$ (see schematic in Figure 4.8b).

The confinement of the electric field near the interface makes TIR particularly suited for the study of surfaces and interfaces. Furthermore, it enables measurements in liquids with strong infrared absorption, such as H_2O [144–146]. Consequently, TIR techniques are widely used in various spectroscopy and microscopy applications, including attenuated total internal reflection Fourier transform infrared spectroscopy (ATR-FTIR) [45, 145, 147], total internal reflection fluorescence (TIRF) microscopy [148, 149], and total internal reflection Raman spectroscopy [150, 151].

To implement TIR-based s-SNOM, the tip is illuminated with the evanescent fields generated above the surface of an optically denser medium when the incoming light

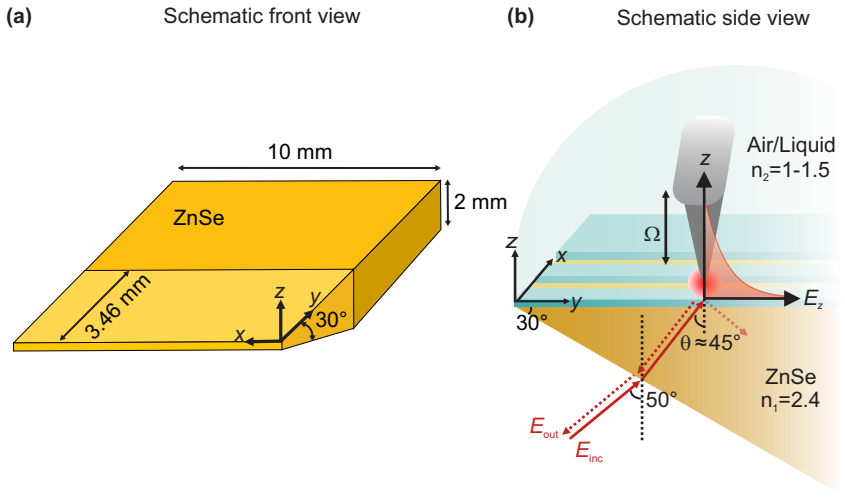

Figure 4.8.: **Implementation of TIR-based illumination and collection scheme**. (a) Schematic of the fabricated ZnSe wedge. The wedge angle is 30°. (b) Schematic of the tip illumination in TIR based s-SNOM. The incoming light E_{inc} is focused onto the ZnSe wedge (n_1) at an angle $\theta > \theta_c$, where θ_c is the critical angle. The tip is illuminated via an exponentially decaying evanescent field generated by total internal reflection of the incoming light at the ZnSe and liquid interface, which efficiently polarizes the tip-sample dipole that radiates into the far field E_{out}.

undergoes total internal reflection. Typically, a prism is used to meet the conditions for TIR and to create this evanescent field. The prism material is selected based on several key criteria: the material must be transparent in the measurement spectral range, exhibit no overlapping IR resonances with the sample, be chemically compatible with both the sample and imaging medium (i.e., does not react with the sample or dissolve in the liquid), and possess a higher refractive index compared to the sample under investigation. Commonly used materials for the prism at IR frequencies include ZnSe, Si, and Ge.

Due to space constraints in the current setup, we utilized a wedged substrate to achieve TIR [45, 146]. Specifically, a wedged ZnSe substrate was chosen for this work owing to its higher refractive index of $n_{\mathrm{ZnSe}} = 2.4$ [152], when compared to the intended imaging media $(\mathrm{H_2O}, \mathrm{D_2O})$ and samples (refractive index of medium 2, $n_2 \sim 1.6$). Furthermore, ZnSe has a broad transmission range $(0.6 - 21\,\mu\mathrm{m})$, is chemically inert, and is easy to fabricate with custom specifications. Additionally, its transparency to visible light (specifically, HeNe laser at $\lambda = 633\,\mathrm{nm}$) facilitates the optical alignment of

the IR beam using a HeNe pilot laser.

The ZnSe wedges were fabricated according to custom specifications by Crystan Ltd, UK. To create the wedges, one edge of a $10 \times 10 \times 2\,\mathrm{mm}$ ZnSe substrate was polished at an angle of 30°. For added stability, the wedge edge was chamfered to $0.3\,\mathrm{mm}$ (see schematic in Figure 4.8a).

A detailed schematic of the tip illumination is shown in Figure 4.8b. In this setup, the wedge is illuminated by a focused beam using an off-axis parabolic mirror ($f = 10\,\mathrm{mm}$) at a central beam angle of approximately 50° relative to the tip axis. The angled polished surface ensures that the ZnSe-air or ZnSe-liquid interface is illuminated at an incidence angle $\theta > \theta_c \approx 34°$ (with $n_2 = 1.35$ and $n_1 = 2.4$). As a result, the tip is illuminated by the TIR-generated evanescent field at the wedge-liquid interface (see Schematic in Figure 4.8b).

The decay length γ of the evanescent field above the ZnSe wedge can be calculated using Equation (4.2). For an illuminating wavelength of $6\,\mu\mathrm{m}$ with $\theta = 45°$, the decay length is approximately $700\,\mathrm{nm}$ in liquid. Consequently, samples are placed directly on the top surface of the ZnSe wedge.

Figure 4.9a illustrates the tip illumination and collection geometry in TIR-based s-SNOM. An off-axis parabola ($f = 10\,\mathrm{mm}$) focuses the incident beam onto the wedged substrate, while the tip-scattered light is collected by the same parabolic mirror. The parabolic mirror was mounted on a three-axis ($-xyz$) piezo translation stage to enable fine positioning of the laser focal spot. The parabolic mirror and the piezo stage were provided by Neaspec, Attocube Systems AG. This setup enables both monochromatic nanoimaging and nano-FTIR spectroscopy, as elaborated in Section 4.5 and Chapter 6.

Figures 4.9b, c display so-called "approach curves" recorded in $\mathrm{D_2O}$ with the TIR s-SNOM and nano-FTIR setup, respectively. These curves show the demodulated near-field amplitude signal s_n ($n \geq 2$) as a function of the tip-sample distance. In practice, the "approach curves" are recorded as the oscillating tip is retracted from the sample surface. Notably, a higher tapping amplitude was used for the AC recorded with nano-FTIR compared to s-SNOM imaging. This adjustment was aimed to improve the signal-to-noise (S/N) ratio when using typically low-powered broadband infrared sources [16, 17, 153].

The approach curves exhibit a strong signal decay with increasing tip-sample distance, which is more pronounced for higher harmonic signals. This behavior is consistent with well-established results from s-SNOM studies in air [88]. As expected, all the curves decay to the noise floor at large tip-sample distances, verifying that background-free near-field signals are measured. The rapid signal decay at higher harmonics of the demodulated signal is known for significantly enhancing surface sensitivity and spatial resolution in s-SNOM and nano-FTIR. Consequently, Figures 4.9b, c suggest that higher

harmonic demodulation may also be exploited for increasing the spatial resolution and surface sensitivity in liquid environments.

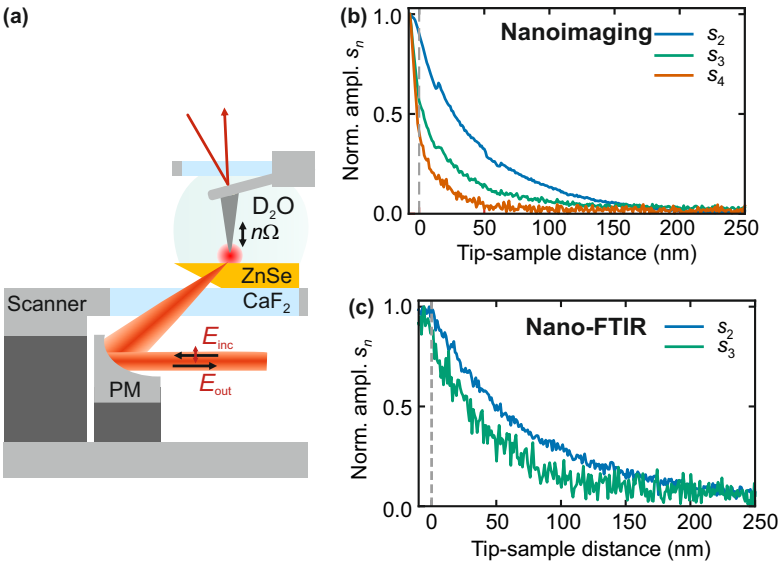

Figure 4.9.: **TIR-based s-SNOM and nano-FTIR in liquid.** (a) Schematic of the setup. The tip is illuminated by the TIR-generated evanescent field. The backscattered light is demodulated at higher harmonic's of the tip's oscillation frequency, $n\Omega$. PM, parabolic mirror. (b) Approach curves (ACs) showing the decay of s-SNOM amplitude signals s_n in liquid (D_2O) with increasing tip-sample distance (i.e., the minimum distance between the tip apex and the sample during an oscillation cycle of the tip, as typically done in tapping mode AFM), recorded at $1600\,\mathrm{cm}^{-1}$. Tapping amplitude (TA) $\sim 60\,\mathrm{nm}$. (c) ACs recorded for the nano-FTIR signal (at the white light position) in liquid, with TA $\sim 120\,\mathrm{nm}$.

In Section 4.5, we demonstrate the application of TIR-based s-SNOM for amplitude- and phase-resolved chemical nanoimaging and nanospectroscopy, both in air and liquid environments. Furthermore, Chapter 6 describes the application of TIR-based s-SNOM for nanoimaging and nanospectroscopy of ultraconfined polaritons in van der Waals materials, specifically hexagonal boron nitride flakes, in a liquid environment.

4.4. Demonstration of transflection s-SNOM for amplitude and phase resolved antenna mapping in liquid

In this section, we apply the transflection s-SNOM setup described in Section 4.3.2 for amplitude- and phase-resolved antenna mapping in a liquid environment, which is crucial for designing and optimizing antennas for enhanced molecular sensing applications in liquid environments.

4.4.1. Sample fabrication

The samples were prepared by Irene Dolado at CIC Nanogune BRTA.

Au disks were fabricated on a double-side polished $\mathrm{CaF_2}\,[100]$ substrate using high-resolution electron-beam lithography. To facilitate the lithography process, a layer of polymethyl methacrylate (PMMA) was spin coated onto the substrate at $4000\,\mathrm{rpm}$, serving as the electron-sensitive polymer. To enable lithography on insulating substrates $(\mathrm{CaF_2})$, a $2\,\mathrm{nm}$ thick layer of gold (Au) was deposited on top of the PMMA layer. This gold layer was then chemically etched by immersing the sample in a $\mathrm{KI/I_2}$ solution for approximately 5 seconds. Following this, the PMMA was developed in a 1:3 methyl isobutyl ketone and isopropanol solution. A $3\,\mathrm{nm}$ layer of Ti was subsequently deposited by electron beam evaporation, followed by thermal evaporation of $50\,\mathrm{nm}$ of Au. Finally, the lift-off of the fabricated disks was accomplished by immersing the sample in acetone overnight.

4.4.2. Nanoimaging in liquid

We demonstrate the application of transflection s-SNOM for antenna mapping in liquid using a gold disk with a diameter of $4\,\mu\mathrm{m}$ on a $\mathrm{CaF_2}$ substrate, exhibiting a dipolar resonance at $10.5\,\mu\mathrm{m}$ wavelength. Simultaneous to the topography (Figure 4.10a, left), we observe two bright spots in the IR amplitude image (Figure 4.10a, middle). They are aligned along the polarization of the incident beam (indicated by the double-sided arrow in Figure 4.11a) and reveal the strongly enhanced fields of the in-plane oriented dipole. The phase (Figure 4.10c, right) at the position of the two bright spots is stable and nearly the same. Similar amplitude and phase images were obtained for the same disk imaged in air (Figure 4.10), demonstrating that our setup allows for reliable amplitude- and phase-resolved imaging of infrared antenna modes without significant distortion by the liquid. However, a small resonance shift is observed due to the liquid, as discussed in detail in Chapter 5, which does not affect the mode pattern.

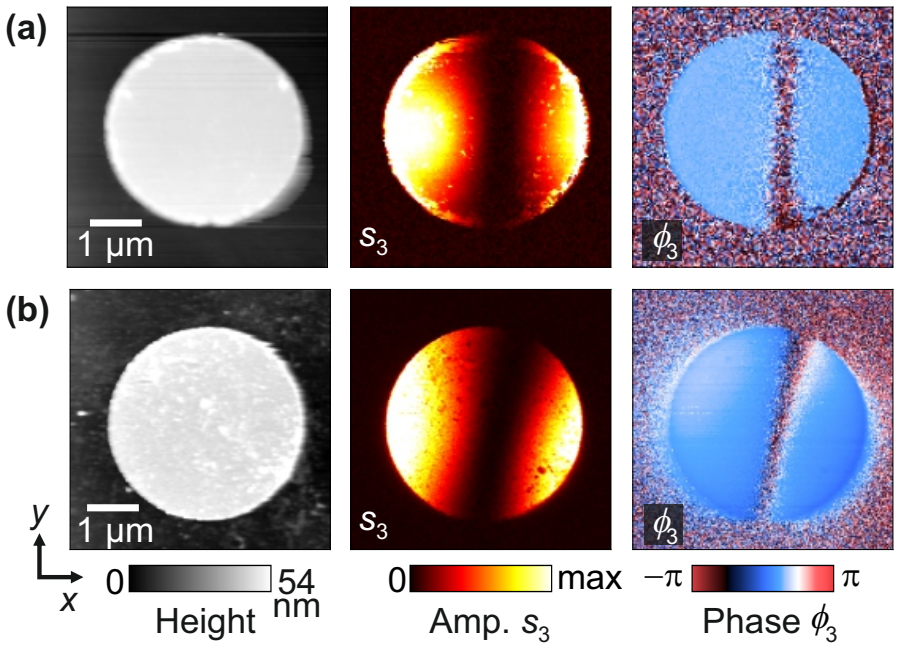

Figure 4.10.: **Normal incidence transflection s-SNOM for mapping mid-IR plasmonic antennas.** (a, b) Topography, amplitude (s_3), and phase (ϕ_3) (from left to right, respectively) images of the dipolar antenna mode of a gold disk (approximately $40\,\mathrm{nm}$ high with a diameter of $4\,\mu\mathrm{m}$) in (a) H_2O and (b) air. The mid-IR imaging wavelength is $10.5\,\mu\mathrm{m}$.

Compared with previous side-illumination s-SNOM experiments [28,135] the amplitude and phase pattern resemble the ones obtained with s-polarized illumination (where particularly the phase is the same for the two bright amplitude spots). This can be explained by a double scattering process [28,135] which is illustrated in Figure 4.11a. Here, the near field of the antenna illuminates and polarizes the tip. The tip-polarization can be approximated as an antenna-induced dipole in the tip. Due to the close proximity of this tip dipole to the antenna, the tip radiates into the far field via the gold disk. As a result, the gold disk effectively acts twice. The amplitude image yields essentially the sum of the squares of the in- and out-of-plane electric antenna near fields (weighted by the polarizability tensor of the tip) and a constant phase across the whole disk. A more detailed discussion is beyond the scope of this thesis and we refer the interested reader to the detailed analysis provided in Reference [135].

To further analyze the near-field contrast, we record approach curves at four representative positions on the sample, as indicated by the colored dots in the inset of Figure 4.11b.

For the ACs recorded on the disk edges (orange and blue curves), we observe a sharp decrease in the near-field amplitude signal s_3 with increasing tip-sample distance. The signal eventually decays to the noise floor for distances $z > 150\,\mathrm{nm}$. The ACs recorded at the left and right edges of the disk are well correlated, suggesting homogeneous illumination of the antennas in the transflection geometry. This allows us to largely avoid the impact of retardation effects on the electromagnetic field of the antennas, as previously described in References [140, 142]. In contrast, the ACs recorded with the tip positioned on the substrate and the center of the disk (pink and green curves) show no notable changes in the amplitude signal s_3. This confirms that the near-field signal is negligible on the substrate, consistent with our previous observations in Figure 4.10.

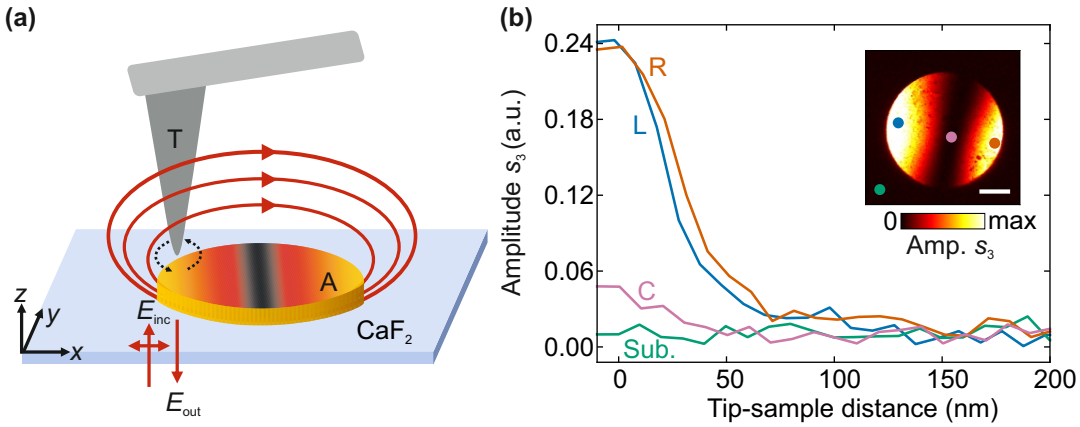

Figure 4.11.: **Probing infrared antennas with tansflection s-SNOM** (a) Illustration of the near-field scattering process. The incident field E_{inc} illuminates the antenna (A). The fields generated by the antenna illuminate and polarize the tip (T), which then scatters the near-field through the antenna into the far field, where it is detected interferometrically (not shown here). (b) Approach curves (ACs) showing how the demodulated s-SNOM amplitude signal s_3 changes with increasing tip-sample distance, recorded at an illumination wavelength of $10\,\mu\mathrm{m}$. The inset shows the near-field amplitude image of the disk antenna as in Figure 4.10. The colored dots in the inset (red, right; blue, left; pink, center; green, substrate) indicate the positions where the ACs were recorded. Scale bar: $1\,\mu\mathrm{m}$.

To summarize, we successfully demonstrate that the transflection s-SNOM setup in liquid yields undistorted, amplitude- and phase-resolved infrared nanoimages of the near-field distribution of resonant plasmonic antennas. These results closely resemble those obtained in air, highlighting the effectiveness of our approach.

4.5. Demonstration of TIR-based s-SNOM for chemical nanoimaging and nanospectroscopy in liquid

In this section, we apply the TIR-based s-SNOM setup described in Section 4.3.3 for chemical nanoimaging and nanospectroscopy in both air and liquid environments. To this end we investigated the IR absorption of a PMMA layer on a wedged ZnSe substrate.

4.5.1. Methods

Sample fabrication

The samples were prepared by Irene Dolado at CIC Nanogune BRTA.

To demonstrate amplitude- and phase-resolved chemical mapping of organic layers in a liquid environment, a layer of 495A4 PMMA was spin coated at $4000\,\mathrm{rpm}$ onto the top surface of a wedged ZnSe substrate. Following this step, the sample was baked for 1 minute and 30 seconds at $180°\mathrm{C}$.

To measure the contrast between the substrate and the PMMA layer, PMMA patches were fabricated using electron beam lithography. To enable electron beam lithography on an insulating substrate, a $2\,\mathrm{nm}$ thick layer of gold was evaporated on top of the PMMA layer. After the electron-beam assisted writing of the patches, the gold was chemically etched by immersing the sample in a KI/I_2 solution for 5 seconds. The PMMA patches were then developed in a methyl isobutyl ketone and isopropanol (MIBK/IPA) 1:3 solution. Finally, the sample was fully dried using a nitrogen gun.

Correction for phase drift in near-field phase images

During the imaging process, the wedged ZnSe substrate with the sample is raster scanned. This scanning causes a change in the effective beam path in the y-direction due to the varying thickness of the substrate that the beam transverses (see geometry illustrations in Figure 4.8b and topography in Figure 4.12a). Consequently, a constant phase drift in the y-direction is superimposed onto the phase images (see Figure 4.12b). To correct for this effect, we calculate the phase correction $\exp(ik_y y)$. For the example in Figure 4.12, we used $k_y = 1.4\,\mu\mathrm{m}^{-1}$, which corresponds to a period of $\approx 4.5\,\mu\mathrm{m}$ (see Figure 4.12c). The corrected phase image is obtained after subtracting the phase correction from the raw phase image (see Figure 4.12d).

This procedure is applied to all phase images presented in this work.

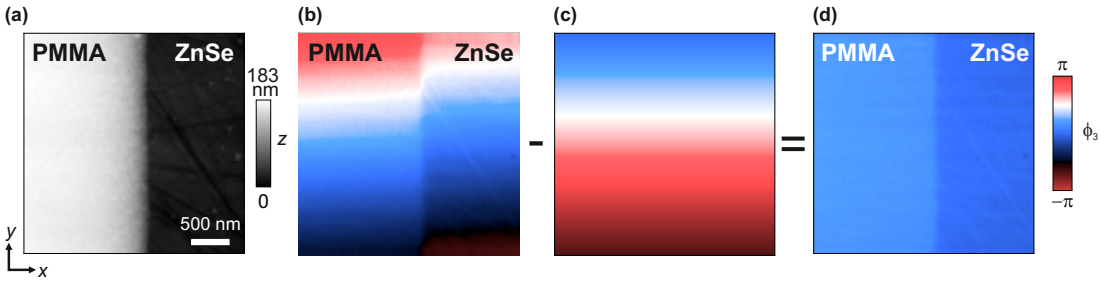

Figure 4.12.: **Phase drift correction.** (a) AFM topography of a $135\,\mathrm{nm}$ thick PMMA layer on a ZnSe wedge. (b) Near-field phase ϕ_3 image recorded at $1735\,\mathrm{cm}^{-1}$, superimposed by a constant phase drift in the y-direction caused by the effective beam path change along the y-direction during imaging. (c) Calculated phase correction $\exp(ik_y y)$, where $k_y = 1.4\,\mu\mathrm{m}^{-1}$. (d) Corrected phase image obtained after subtracting the calculated phase correction in panel c from the raw phase image in panel b.

4.5.2. Amplitude- and phase-resolved chemical mapping in air and liquid

The interferometric detection scheme in s-SNOM allows for simultaneous measurement of the near-field amplitude s_n and phase ϕ_n of the scattered field, which encodes information about the local dielectric function of the sample. For dielectric materials, such as polymers and biological samples, the signals s_n and ϕ_n provide insights into the local reflectivity and absorption of the sample, respectively, facilitating chemical identification and composition mapping with nanoscale resolution [15, 21, 110].

To demonstrate nanoscale-resolved chemical mapping using the TIR-based s-SNOM setup in both air and liquid environments, we investigated the well-defined C = O stretching mode of PMMA [16] (see dielectric function in Figure 4.13d [154]). The PMMA layer was spin coated directly onto the wedged ZnSe substrate (refer to the schematic in Figure 4.13b) according to the protocol described in Section 4.5.1. Figures 4.13a, g show the topography of a $135\,\mathrm{nm}$ thick PMMA layer recorded in air and H_2O, respectively. The smooth topography images acquired in liquid indicate stable AFM operation with minimal noise.

Using SOH (detailed description is provided in Section 3.4.2, Chapter 3), we recorded, simultaneous to the topography, the near-field amplitude s_3 and phase ϕ_3 images of the sample in both air (Figures 4.13a-f) and liquid (Figures 4.13g-l) environments. The near-field images were recorded at two representative frequencies: $1735\,\mathrm{cm}^{-1}$, where the PMMA film is strongly absorbing (indicated by the blue dashed line in Figures 4.13d, j) and $1600\,\mathrm{cm}^{-1}$ (green dashed line in Figures 4.13d, j), where the PMMA film is non-absorbing.

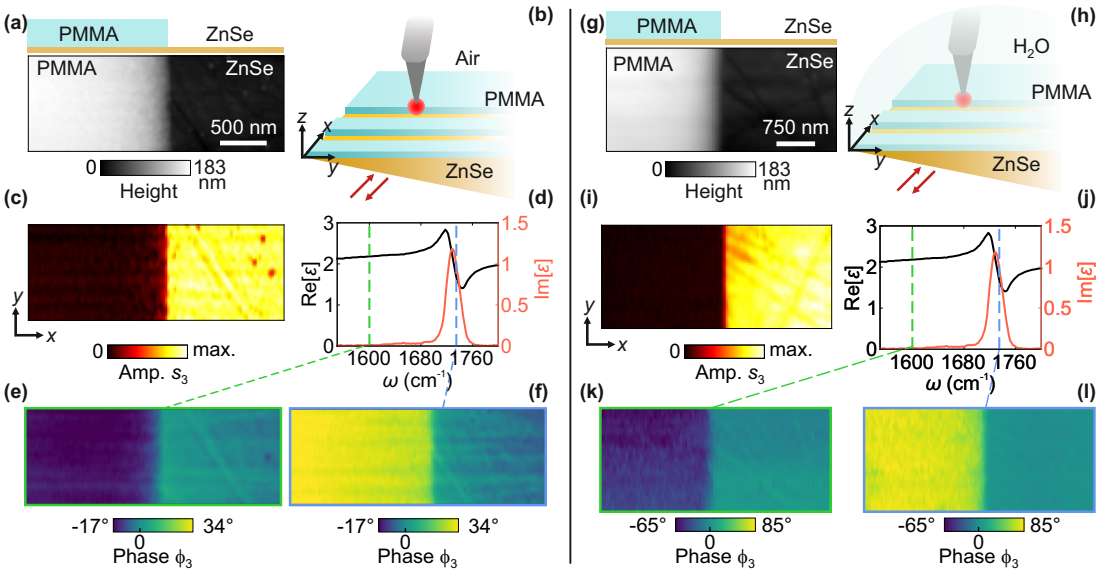

Figure 4.13.: **Amplitude- and phase-resolved dielectric mapping in air (a-f) and liquid (g-l).** (a) AFM topography of a 135 nm thick PMMA layer on a ZnSe wedge recorded in air. (b) Schematic of TIR-based s-SNOM imaging of PMMA film (blue) on a ZnSe wedge (yellow) in air. (c) Near-field amplitude image s_3 recorded at 1600 cm^{-1}. (d) Real (black) and imaginary (red) parts of the dielectric function of PMMA, modeled by a Lorentz oscillator, showing the IR absorption centered around 1735 cm^{-1} [154]. (e) Near-field phase image ϕ_3 recorded at 1600 cm^{-1} and (f) at 1735 cm^{-1}. (g-l) Same as panels a-f, but for measurements performed in liquid (H_2O).

To ensure consistency between different measurements, the measured near-field images were normalized to the average signal obtained from the ZnSe substrate. Specifically, the normalized amplitude is expressed as $s_n^{\mathrm{PMMA}}/s_n^{\mathrm{ZnSe}}$ and the normalized phase as $\phi_n^{\mathrm{PMMA}} - \phi_n^{\mathrm{ZnSe}}$. For clarity, we will refer to these normalized values simply as s_n and ϕ_n throughout the discussion. It is important to note that scanning the ZnSe wedge in the y-direction yields a phase drift, which was subtracted from all phase images presented in this work (see Section 4.5.1).

In the normalized near-field amplitude s_3 images recorded in air (Figure 4.13c) and in liquid (H_2O) (Figure 4.13i), we observe a strong near-field contrast between the PMMA region and the ZnSe substrate, i.e., PMMA appears darker than the substrate. The higher near-field amplitude signal on ZnSe can be attributed to its higher refractive index compared to PMMA [11, 152]. The abrupt change in the near-field amplitude signal at the material boundary verifies the nanoscale spatial resolution in both air and liquid environments.

Figures 4.13f, l show the near-field phase images recorded at 1735 cm^{-1} (which is associ-

ated with the $\mathrm{C=O}$ stretching mode of PMMA [155]) in both air and $\mathrm{H_2O}$, respectively. In both environments, as expected a positive phase contrast between the PMMA layer and the ZnSe substrate is observed due to the strong IR absorption by the PMMA layer relative to the non-absorbing ZnSe substrate [15]. For the near-field phase images recorded at $1600\,\mathrm{cm^{-1}}$, where PMMA is non-absorbing, we expected a vanishing phase contrast between the PMMA layer and the ZnSe substrate (i.e., $\phi_n^{\mathrm{PMMA}} - \phi_n^{\mathrm{ZnSe}} = 0$). However, a negative phase contrast on the PMMA layer is observed in the near-field images recorded in both air (Figure 4.13e) and liquid (Figure 4.13k) environments (see also line profiles in Figures 4.14d, h).

Negative phase contrasts on weakly absorbing materials with respect to a non-absorbing reflective substrate have been previously observed in literature [21, 42, 156, 157]. In our setup, we speculate that the negative contrast on PMMA is caused by a cumulative effect of the negative contrast typically observed in s-SNOM experiments [21, 42, 156, 157] and the optical path difference caused by the vertical movement of the ZnSe wedge as the tip scans the PMMA film (see schematic in Figure 4.14b). However, for the measurements recorded in liquid, we observe a much higher negative contrast on PMMA compared to the measurements in air. This effect is potentially related to the mixing of the amplitude and phase signals observed in TIR-based nano-FTIR spectroscopy discussed in Section 4.5.3.

To isolate the local near-field response of the sample, we calculated the difference of the demodulated phase data obtained at the third and second harmonics, expressed as $\phi_3 - \phi_2$. The resultant phase images and corresponding line profiles are shown in Figures 4.14e, f (air) and Figures 4.14i, j (liquid), revealing the vanishing phase contrast between the PMMA film and the ZnSe substrate. The method of calculating complex-valued ratios between two harmonics (i.e., $\frac{\sigma_m}{\sigma_n} = \frac{s_m}{s_n} \exp i\,(\phi_m - \phi_n)$ for m$\neq n$) has been previously employed to effectively eliminate artifacts resulting from far-field reflections [158, 159] and isolating the pure near-field response of the sample.

A comparison of near-field images recorded in liquid and air offers significant insights. The signal-to-noise ratio in the liquid environment is slightly reduced, likely due to enhanced IR absorption, sample drift, and tip contamination during probing in $\mathrm{H_2O}$. Nevertheless, the amplitude and phase contrasts between the PMMA and ZnSe areas remain distinct and clear. The qualitative agreement between near-field images obtained in both environments confirms the robustness and sensitivity of the TIR-based s-SNOM technique for high-resolution chemical nanoimaging, even in liquid environments.

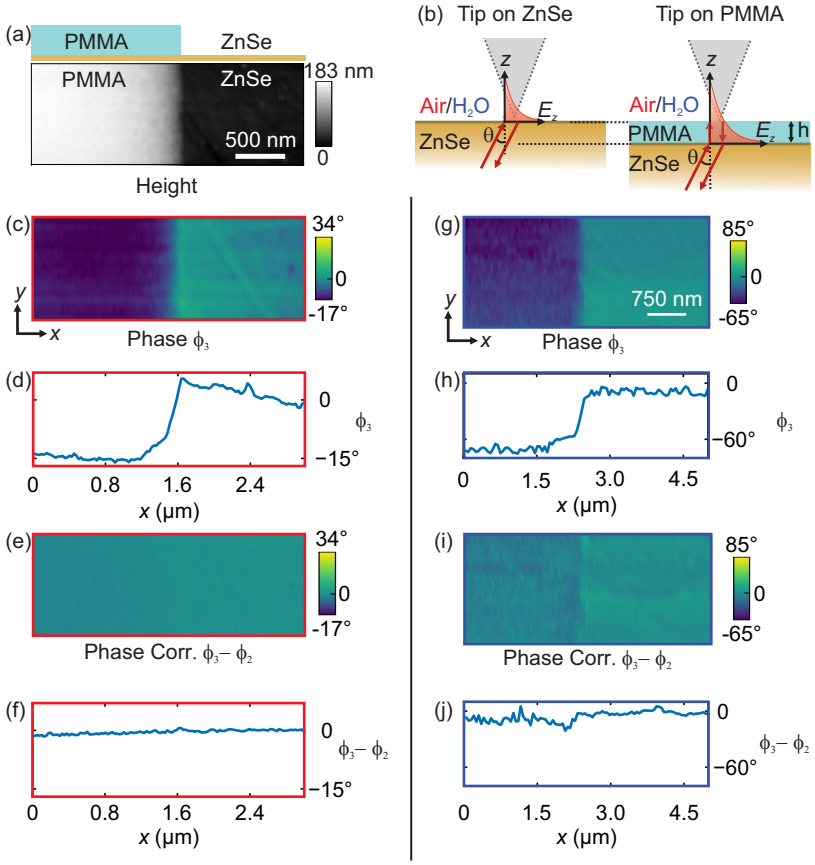

Figure 4.14.: **Negative phase contrast on the PMMA film on ZnSe wedge.** (a) AFM topography of a 135 nm thick PMMA layer on ZnSe. (b) Schematic showing the optical path traversed by the incoming beam when the tip is on ZnSe (left) and on PMMA (right). (c) Near-field phase image recorded at $1600\,\mathrm{cm}^{-1}$, revealing a negative phase contrast on PMMA compared to the substrate and (e) the corresponding line profile (averaged over 10 lines) extracted perpendicular to the PMMA edge. (d) Calculated near-field phase difference image $(\phi_3 - \phi_2)$ recorded at $1600\,\mathrm{cm}^{-1}$ and (f) the corresponding line profile extracted perpendicular to the PMMA edge. Panels (g-j) show the same as panels c-f, but for mapping done in liquid H_2O.

4.5.3. Amplitude- and phase-resolved nanospectroscopy in air and liquid

We finally demonstrate nanoscale-resolved chemical recognition using TIR-based nano-FTIR spectroscopy in both air and liquid environments. For the liquid measurements, the spectra were recorded in D_2O instead of H_2O to minimize IR absorption by the liquid [121,122]. To this end, we recorded point spectra indicated by red/blue (PMMA) and green (reference, ZnSe) markers in the topography images, as presented in Figures 4.15b (air) and 4.15f (D_2O). Figures 4.15c, d show the normalized amplitude

$$s_2(\omega) = \frac{s_2^{\mathrm{PMMA}}(\omega)}{s_2^{\mathrm{ZnSe}}(\omega)} \tag{4.3}$$

and phase

$$\phi_2(\omega) = \phi_2^{\mathrm{PMMA}}(\omega) - \phi_2^{\mathrm{ZnSe}}(\omega) \tag{4.4}$$

spectra recorded in air, respectively. The amplitude spectrum $s_2(\omega)$ (Figure 4.15c) exhibits dispersive behavior at $1735\,\mathrm{cm}^{-1}$, corresponding to the C = O stretching mode in PMMA. Conversely, the phase spectrum $\phi_2(\omega)$ (Figure 4.15d) shows an absorption peak at $1735\,\mathrm{cm}^{-1}$. These near-field amplitude and phase spectra closely resemble the real and imaginary parts of the complex dielectric permittivity of PMMA (see Figure 4.13d), respectively. These observations are consistent with expected near-field response of organic materials [14,15,21].

However, we observe significant deviations when examining the spectra from the sample fully immersed in the liquid environment (see Figures 4.13g, h for amplitude $s_2(\omega)$ and phase $\phi_2(\omega)$ spectra, respectively). Specifically, the amplitude spectrum $s_2(\omega)$ (Figure 4.13g) exhibits a dip centered around $1735\,\mathrm{cm}^{-1}$, while the phase spectrum $\phi_2(\omega)$ (Figure 4.15h) exhibits dispersive behavior. In simpler terms, the amplitude and phase spectra appear reversed compared to their air counterparts.

Although this setup demonstrates sensitivity to the chemical composition of the sample, further studies are required to explore this phenomenon. This could be caused due to contributions from both propagating and evanescent fields that illuminate the tip, which arise from a non-optimal prism geometry given the space constraints in our current setup or from enhanced higher-order mechanical harmonic generation in liquids. Nevertheless, in Chapter 6, we successfully apply this TIR-based setup for the mapping and nanospectroscopy of ultra-confined phonon polaritons in liquid environments.

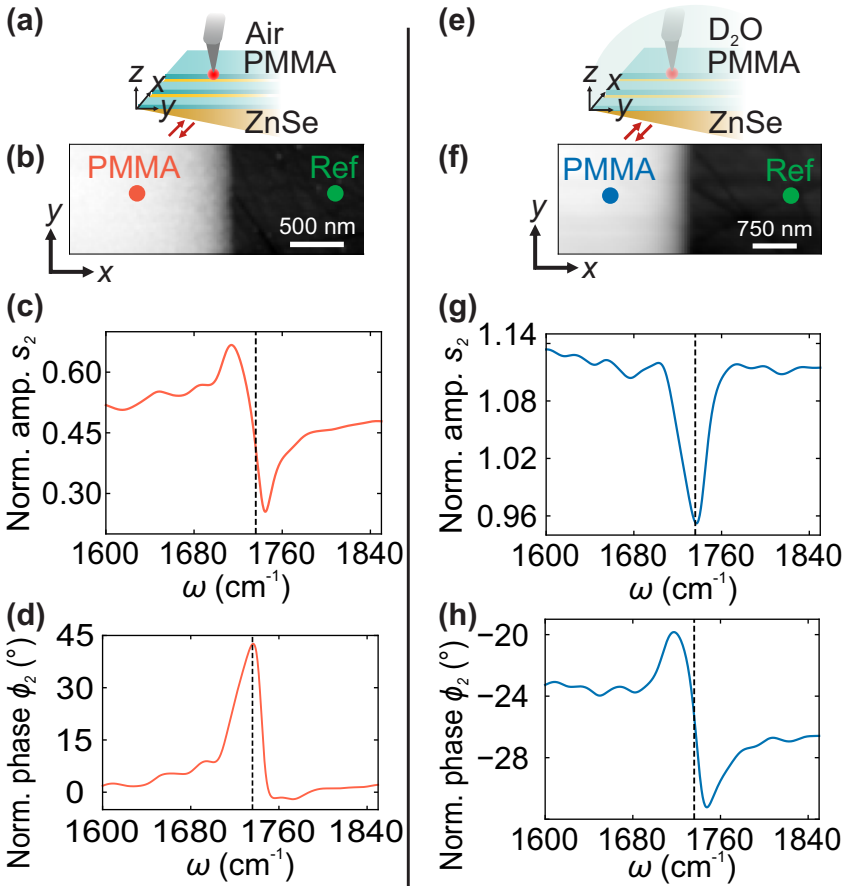

Figure 4.15.: **TIR-based nano-FTIR spectroscopy in air and liquid.** (a) Schematic of TIR-based nano-FTIR in air. (b) AFM topography of a 150 nm thick PMMA layer on a ZnSe wedge. The bright area corresponds to the PMMA layer. (c) Normalized nano-FTIR amplitude $s_2(\omega)$ and (d) phase $\phi_2(\omega)$ spectra of PMMA, recorded at the point indicated by the red dot in the topography image shown in panel b. The spectra are normalized to those recorded on ZnSe (green dot in the topography image). (e-h) Same as panels a-d, but recorded in liquid (D_2O). The position at which the PMMA spectra were recorded is indicated by a blue dot in the topography image in panel f. Spectral resolution: 16.67 cm^{-1}

4.6. Conclusions and outlook

In this chapter, we developed and implemented two novel instrumentation techniques to enable infrared s-SNOM and nano-FTIR spectroscopy for samples fully immersed in liquid environments. These advancements address the significant challenges posed by water's strong IR absorption and the complexities of AFM operation in liquids.

The first approach described is the normal incidence transflection s-SNOM setup, which minimizes the optical path through the liquid and effectively reduces IR absorption in water. This setup demonstrated robust, background-free amplitude- and phase-resolved infrared nanoimaging of the near-field distribution of resonant plasmonic antennas in liquid. This setup can potentially facilitate future in-situ s-SNOM studies of (bio)chemical substances with enhanced sensitivity [160], vibrational strong coupling experiments [161], or plasmon-induced chemical modifications. By extending the applicability of this setup for nanospectroscopy of single antennas in both air and liquid environments, we move closer to fully realizing in-situ studies based on antenna-enhanced s-SNOM nanoimaging and nanospectroscopy, as described in Chapter 5.

The second approach is the TIR-based s-SNOM setup, which utilizes evanescent fields generated by TIR for efficient tip excitation. This setup enables high-resolution chemical nanoimaging and nanospectroscopy of samples fully immersed in liquids. Although deviations in dielectric contrasts in air and liquid are observed (specifically between PMMA and ZnSe), our TIR-based s-SNOM setup demonstrates promising results for chemical mapping and identification of samples. Further exploration and optimization of the setup is needed for quantitative dielectric mapping using TIR-based s-SNOM. Nevertheless, this setup was successfully applied for mapping ultraconfined phonon polaritons in van der Waals materials like hexagonal boron nitride (h-BN). Detailed application of this setup for polariton mapping and nanospectroscopy in liquids is explored in Chapter 6.

These advancements collectively represent a significant step forward in near-field optical microscopy of materials in their native liquid states. The methodologies presented here lay a foundation for future optimization and exploitation of both transflection and TIR-based setups for in-situ infrared studies of chemical, polaritonic, and biological systems fully immersed in liquid environments.

5. Transflection nano-FTIR for infrared spectroscopy of single metal antennas

Infrared antennas based on metal nanostructures facilitate efficient conversion of incident light into highly confined hotspots that are characterized by strongly enhanced electromagnetic fields. A nanoscale-resolved characterization of the local electromagnetic field distribution of metal antennas is crucial for understanding and exploiting these hotspots in the future for highly sensitive sensing applications. In this chapter, we demonstrate the application of the normal incidence transflection nanoscale resolved Fourier Transform Infrared (nano-FTIR) spectroscopy setup described in Chapter 4 for near-field spectroscopy of resonant metal antennas in both air and liquid environments. We describe the key technical details for recording, referencing, and stitching transflection nano-FTIR spectra. The results form a foundation for future nano-FTIR studies of antenna enhanced molecular spectroscopy in liquid environments and may open new paths for developing highly sensitive molecular sensors. Some parts of the results presented in this chapter are published in Reference [162].

5.1. Introduction

Optical and infrared (IR) antennas based on metal nanostructures facilitate the efficient conversion of incident light into highly confined hotspots characterized by strongly enhanced electromagnetic fields [163–167]. Nanoantennas play a crucial role in the development of highly sensitive (bio)chemical sensors [167–170], optoelectronics [171–173] and light detection devices [174, 175]. At infrared frequencies, localized plasmon resonances in metal antennas have significantly improved surface-enhanced infrared absorption (SEIRA) spectroscopy in both air [134, 135] and liquid environments [136–138], allowing for highly sensitive analyses of chemical composition and molecular conformation of minute quantities of substances, opening new possibilities for plasmonic sensing in the infrared spectral range.

Imaging the local field distribution of metal nanostructures is critical for designing and optimizing antenna performance. Scanning near-field optical microscopy (s-SNOM) [13] has emerged as a powerful tool for mapping the antenna near-fields, providing access to both the amplitude and the phase of the antenna near-fields with nanoscale

resolution [25, 130, 140, 142, 176, 177]. In a typical s-SNOM setup, a metal-coated tip is illuminated with $p-$polarized light (i.e., along the tip axis). The tip-scattered light is detected in the far-field using an interferometric detection scheme (see Figure 4.1b in Chapter 4). The near-field interaction between the tip and the sample modifies the scattered field, allowing for mapping the local dielectric properties of the sample with nanoscale resolution. However, when mapping the antenna near-field distribution, the excitation of the metallic tip in a such a scheme can distort the near-fields of the antenna [133].

Several modifications to the typical s-SNOM setup have been introduced to minimize the tip perturbations. These include using a dielectric tip illuminated with $s-$polarized light [28, 141, 178] (i.e., perpendicular to the tip axis and along the antennas) and employing cross-polarization illumination and detection schemes [140, 142]. Transmission mode s-SNOM [130] and transflection s-SNOM (developed in this work, see details in Chapter 4) [112] are alternate illumination schemes, that enable distortion-free antenna mapping and homogeneous illumination of the antenna, preventing retardation effects on the electromagnetic response of the sample [140, 142]. However, distortion-free nano-FTIR spectroscopy of antenna near-fields has not been demonstrated so far. Furthermore, most studies have primarily been performed in air. s-SNOM-based infrared mapping and spectroscopy of antennas in both air and liquid environments represent an essential first step towards future in-situ studies of antenna-enhanced chemical sensing. In Chapter 4, Section 4.4, the normal incidence transflection s-SNOM was successfully demonstrated for background-free, amplitude- and phase-resolved infrared nanoimaging of the near-field distribution of resonant plasmonic antennas in liquid environments [112].

In this chapter, we demonstrate a normal-incidence transflection nano-FTIR setup for infrared spectroscopy of individual antenna structures in both air and liquid environments. The chapter is structured as follows: In Section 5.2, we introduce the methodologies used in our experiments, including sample preparation and numerical simulations. In Section 5.3, we discuss the transflection nano-FTIR setup and the normalization process of the spectra. Details of phase unwrapping and stitching of nano-FTIR spectra recorded at different broadband laser settings are presented in Section 5.3.2. In Section 5.4, we demonstrate the application of the setup for infrared spectroscopy of individual metal rod antennas in both air and liquid environments, followed by a discussion on the shifts in antenna resonance frequencies and the origins of the observed spectral features.

5.2. Methods

5.2.1. Sample preparation

The sample preparation was carried out by Irene Dolado at CIC Nanogune BRTA.

In this chapter, we present results obtained from experiments conducted on Au rods fabricated on a double-side polished $\mathrm{CaF_2}\,(100)$ substrate using high-resolution electron-beam lithography. For the lithography process, Polymethyl methacrylate (PMMA) was spin coated onto the substrate at $4000\,\mathrm{rpm}$,acting as the electron-sensitive polymer layer. To facilitate the lithography process on the insulating substrate, $2\,\mathrm{nm}$ thick layer of gold was deposited on top of the PMMAlayer. After the electron-beam assisted writing of the rods, the gold was chemically etched by immersing the sample in a $\mathrm{KI/I_2}$ solution for ~ 5 seconds. PMMA was then developed in $1:3$ methyl isobutyl ketone: isopropanol. Subsequently, a $3\,\mathrm{nm}$ layer of Ti was deposited by electron beam evaporation, followed by the thermal evaporation of a $50\,\mathrm{nm}$ Au layer. Finally, the lift-off of the fabricated rods was done by immersing the sample in acetone overnight.

Using an identical protocol, Au patches with dimensions of $100 \times 100\,\mu\mathrm{m}$ were also fabricated on the same $\mathrm{CaF_2}$ substrate through electron beam lithography. These Au patches serve as a reference plane for the experimental work discussed in this chapter.

5.2.2. Numerical simulations

The numerical calculations were carried out by Martin Schnell at CIC Nanogune BRTA.

For the results presented in Figure 5.7(b), the out-of-plane component (E_z) of the antenna near-fields as a function of the incoming light frequency was calculated numerically using the finite-difference time-domain (FDTD) method (Ansys Lumerical FDTD, Ansys, Inc.). Although, in transflection mode the sum of the square of the in- and out-of-plane electric antenna near-fields (weighted by the polarizability tensor of the tip) is mapped, the out-of-plane electric antenna near-field $|E_z|$ can be used as a good approximation to describe the near-field amplitude at the extremities of the antenna [135].

The simulations were performed for rod antennas with lengths ranging from $L = 1.5\,\mu\mathrm{m}$ to $L = 2.5\,\mu\mathrm{m}$, while the width and height were fixed at $W = 100\,\mathrm{nm}$ and $H = 100\,\mathrm{nm}$, respectively. The calculations were performed for rod antennas placed on a $\mathrm{CaF_2}$ substrate in both air and in $\mathrm{H_2O}$. The near-field was computed at a height of $50\,\mathrm{nm}$ above the antenna surface and $100\,\mathrm{nm}$ from one of the antenna ends. A mesh size of $5\,\mathrm{nm}$ was used for these calculations.

The dielectric permittivity of gold (Au) was calculated by a Drude fit to the Johnson and Christy values (permittivity 6, plasma resonance $\omega_p = 1.3597 \times 10^{16}\,\frac{\mathrm{rad}}{\mathrm{s}}$, plasma collision $\omega_c = 1.07527 \times 10^{14}\,\frac{\mathrm{rad}}{\mathrm{s}}$) [179]. The dielectric permittivities of H_2O and CaF_2 were taken from references [180] and [181], respectively.

5.3. Transflection nano-FTIR setup and normalization of nano-FTIR spectra

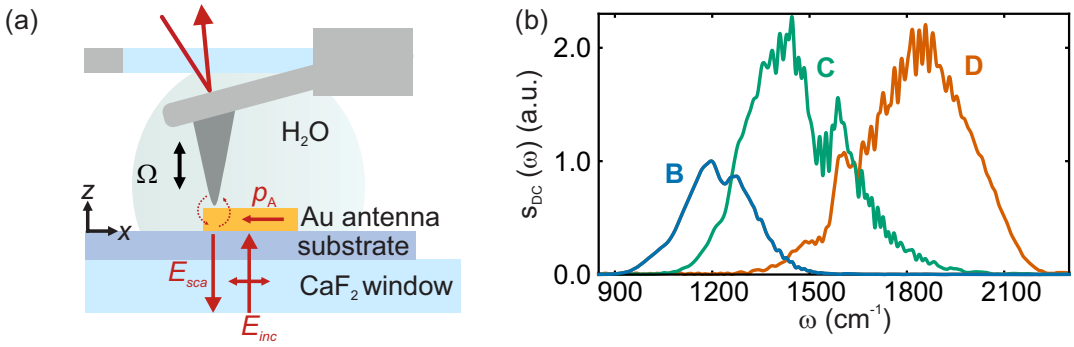

Figure 5.1.: **Normal incidence transflection nano-FTIR setup for near-field infrared spectroscopy in air and liquid.** (a) Illustration of the illumination and scattering process in the transflection nano-FTIR setup. A metal-coated AFM tip is illuminated with an infrared supercontinuum (IRSC) broadband laser. The incident field, E_{inc}(polarized along the long axis of the antenna), induces a dipole moment p_{A}in the antenna. Dashed lines illustrate the near-field coupling between the antenna and the tip, which is modulated at the tip tapping frequency Ω. The backscattered field, E_{sca} is analyzed in the far field using an asymmetric nano-FTIR spectrometer, yielding amplitude and phase spectra of the antennas (not shown here). (b) Measured output spectra for three settings of the IRSC laser covering a frequency range of $850 - 2200\,\mathrm{cm}^{-1}$.

A detailed description of the normal incidence transflection s-SNOM setup developed during this work has been previously presented in Chapter 4. Here, we describe the application of the transflection setup for spectroscopic measurements of single IR-resonant antennas. The transflection-mode geometry allows for efficient excitation of the antenna structures on the sample while largely avoiding direct excitation of the s-SNOM probe as the long axis of the tip is oriented along the direction of light propagation. This configuration permits the use of metallic near-field probes as a strong scatterer of the local near-fields.

A schematic of the setup is shown in Figure 5.1a. For nano-FTIR spectroscopy, a standard $\mathrm{Pt-Ir}$ coated (metallic) AFM tip (NCPt arrow tip, Nanoworld) is illuminated under normal incidence with broadband infrared radiation (IRSC). The IRSC laser covers the following frequency ranges: B: $850-1450\,\mathrm{cm}^{-1}$, C: $1200-1900\,\mathrm{cm}^{-1}$, and D: $1500-2200\,\mathrm{cm}^{-1}$ depending on the settings of the broadband laser (see output spectra in Figure 5.1b). As in Chapter 4, Sections 4.3.2 and 4.4, a parabolic mirror is used to focus the IRSC beam (under normal incidence) through a $\mathrm{CaF_2}$ window (sample holder) and the substrate ($\mathrm{CaF_2}$). The polarization of the illuminating beam is chosen to be parallel to the nanorod axis for efficient excitation of the dipolar resonance. The back-scattered light transmitted through the substrate is collected by the same parabolic mirror and analyzed using an asymmetric Fourier transform spectrometer. Background contributions are suppressed by oscillating the near-field probe sinusoidally in the $z-$direction with an amplitude $\Delta\delta \sim 100\,\mathrm{nm}$ and frequency $\Omega = 256\,\mathrm{kHz}$, $\delta = \delta_0 + \Delta\delta\cos\Omega t$. The detector signal is then demodulated at a frequency $n\Omega$, yielding background-free amplitude $s_n(\omega)$ and phase $\phi_n(\omega)$ spectra of individual Au antennas for $(n \geq 2)$. Measurements in liquid were conducted using the same open liquid cell concept described in Chapter 4, Section 4.3, with $\mathrm{H_2O}$ as the liquid medium for the results presented in this Chapter.

To ensure background-free detection of antenna near-fields, we maximize the signal scattered by the antenna at each setting of the IRSC laser placing the tip at one of the ends of the IR-resonant rod antenna. During this process, we block the reference arm of the nano-FTIR interferometer and record white-light images, which are essentially spectrally integrated maps of the rod antenna. Upon proper alignment of the setup, we observe the fundamental dipolar mode of the rod antennas (Figure 5.2a), even though spectrally integrated maps of the antenna field are recorded. This can be attributed to the broader spectrum of the rod antenna in comparison to the frequency range of one of the ranges (B, C, or D) of the IRSC laser. More importantly, the signal on the substrate is small and below the noise floor.

To quantify this observation, Figure 5.2b shows line profiles taken across the long axis of the rods. Recording near-field spectra on the antenna and on the substrate confirms that the near-field signal is negligible on the substrate (Figure 5.2c). Additionally, we recorded approach curves (Figure 5.2d) with the tip placed at the edge of the rod antenna, showing the typical exponential decay of the demodulated signal s_n $(n \geq 2)$ with increasing tip-sample distance [88]. All the harmonics decay to the noise floor within a tip-sample distance of approximately $60\,\mathrm{nm}$. Therefore, we conclude that the transflection setup allows for both uniform illumination of antenna structures and background-free detection of the antenna spectra.

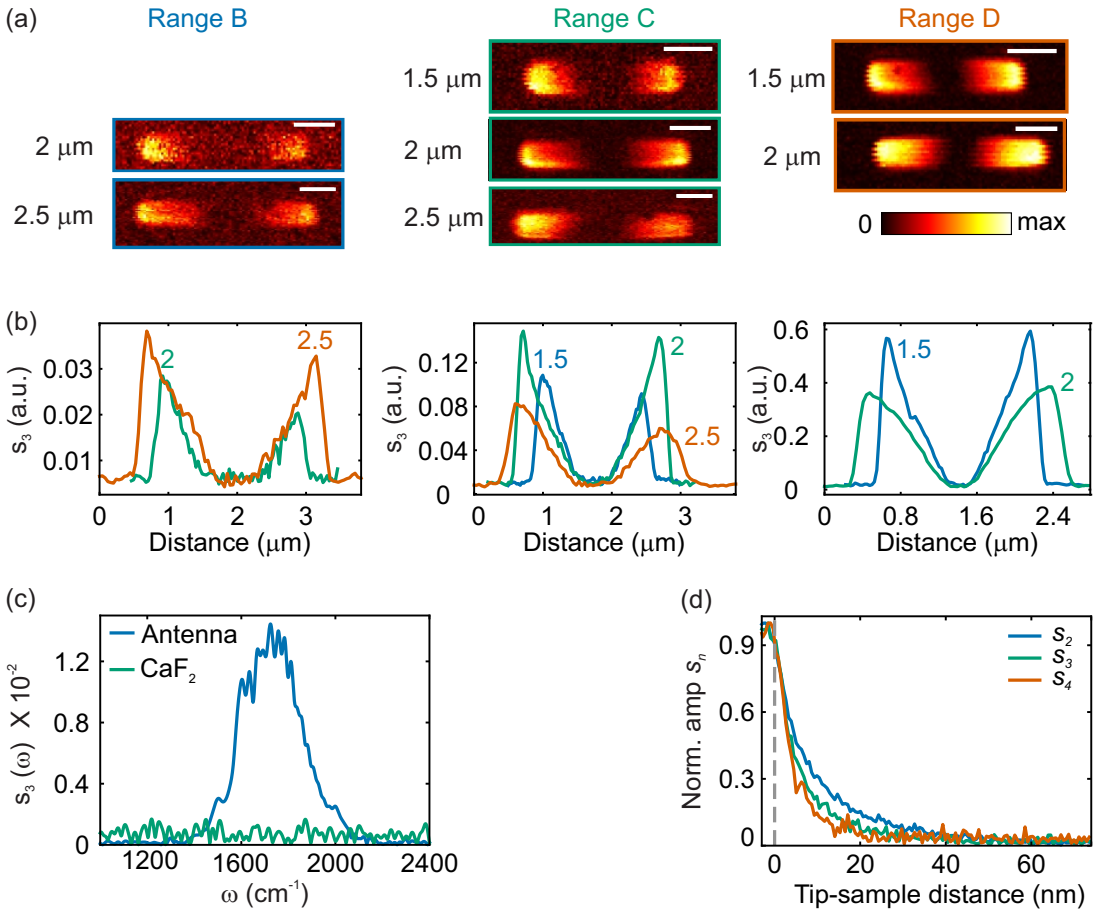

Figure 5.2.: **White-light imaging and other test measurements for near-field alignment.** (a) White-light images of the rod antennas taken at different settings of the broadband laser: B: $850 - 1450\,\mathrm{cm}^{-1}$, C: $1200 - 1900\,\mathrm{cm}^{-1}$, and D: $1500 - 2200\,\mathrm{cm}^{-1}$. The fundamental dipolar mode is clearly visible. Scalebar: $500\,\mathrm{nm}$. (b) Line profiles taken along the long axis of the rod antennas in (a), averaged over 8 lines. (c) Raw near-field amplitude spectra recorded on a $1.8\,\mu\mathrm{m}$ long rod antenna and on the CaF_2 substrate. (d) Approach curves recorded at the edge of a $1.5\,\mu\mathrm{m}$ long antenna, measured at the white light position. Tapping amplitude $\sim 78\,\mathrm{nm}$.

5.3.1. Normalization of nano-FTIR spectra

For spectral analysis of the antenna structures, we placed the tip at one of the edges of the rod antenna (Figure 5.3a) and recorded interferograms by recording the demodulated detector signal while translating the reference mirror (Figure 5.3c, blue). We then removed the global DC offset from the recorded interferograms, applied a Tukey

window with a parameter of $\alpha = 0.1$, and zero filled the interferograms by a factor of 3. The raw near-field amplitude $s_n^{\mathrm{sam}}(\omega)$ (Figure 5.3d, blue) and phase spectra $\phi_n^{\mathrm{sam}}(\omega)$ (Figure 5.3e, blue) were obtained by inverse Fourier transformation of the interferograms. For quantitative analysis of nano-FTIR spectra, the recorded sample spectra needs to be normalized to a reference spectra. In a typical side-illumination nano-FTIR setup, the reference spectrum is recorded on a spectrally flat substrate such as Au or Si. However, in transflection nano-FTIR spectroscopy (Figure 5.2, see also Chapter 4, Section 4.4), where the near-field signal on the substrate is negligible, reference spectra cannot be recorded on the substrate. To remove the influence of the instrument characteristics from the transflection nano-FTIR spectra, we fabricated large $(100\,\mu\mathrm{m} \times 100\,\mu\mathrm{m})$ Au patches adjacent to the antennas on the same sample.

We then carried out the following steps: First, the s-SNOM probe was moved to the center of the metal patch and brought into close proximity to the patch surface (Figure 5.3b). By doing so, the incident beam was focused on, and reflected at, the metal patch, effectively shielding the s-SNOM probe from directly contributing to the measurement. We recorded the DC signal of the MCT detector by using the DC output at the detector amplifier and selecting the s_0 signal in the microscope software to acquire a reference interferogram (Figure 5.3c, red). Applying the same steps as mentioned above, we obtained the DC amplitude $s_{\mathrm{DC}}^{\mathrm{ref}}(\omega)$ (Figure 5.3d, red) and phase $\phi_{\mathrm{DC}}^{\mathrm{ref}}(\omega)$(Figure 5.3e, red) reference spectrum. The normalized near-field spectra were then determined according to:

$$s_n(\omega) = \frac{s_n^{\mathrm{sam}}(\omega)}{s_{\mathrm{DC}}^{\mathrm{ref}}(\omega)} \tag{5.1}$$

and

$$\phi_n(\omega) = \phi_n^{\mathrm{sam}}(\omega) - \phi_{\mathrm{DC}}^{\mathrm{ref}}(\omega) + 180^\circ. \tag{5.2}$$

Normalization of the amplitude spectra mitigates the influence of the nano-FTIR source spectrum. Simultaneously, normalization of the phase spectra provides an absolute measurement of the scattering phase of the antenna. The normalization effectively corrects for the phase shifts accumulated by both the illuminating and scattered beams as they traverse the substrate, thereby allowing for direct and reliable comparison of phase spectra across different antennas. Notably, during the reference measurement, the illuminating beam undergoes an additional phase shift of 180° due to the reflection from the metal patch. Consequently, we explicitly incorporate this additional phase shift into ϕ_n in Equation (5.2).

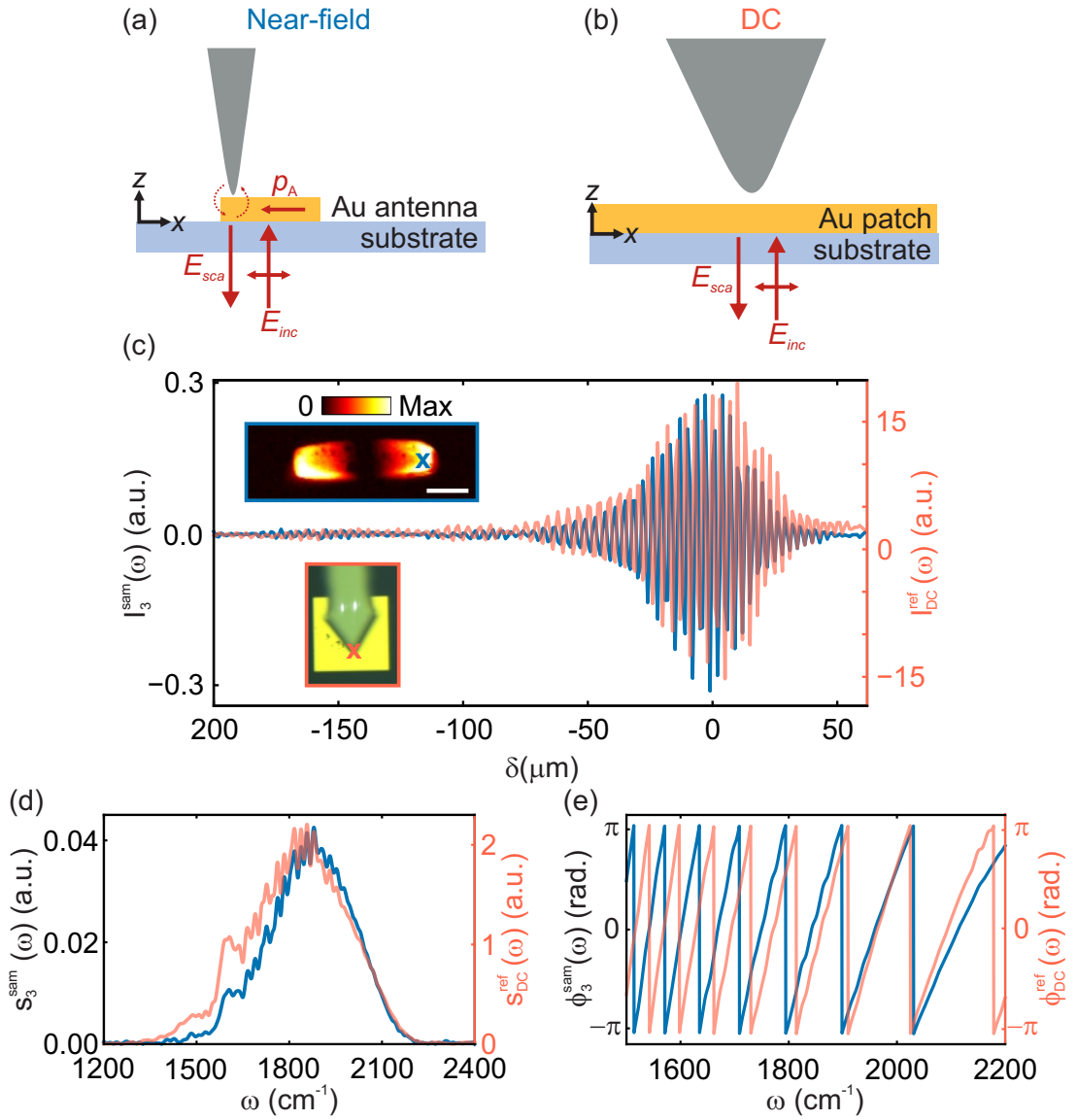

Figure 5.3.: **Nano-FTIR measurements of individual Au rod antennas.** (a) Illustration of the tip position for recording raw near-field spectra on the sample, at one edge of a linear rod antenna. (b) Schematic of the tip position for recording the reference spectra on a $100 \times 100\,\mu$m Au patch. (c) Interferograms recorded on a $1.5\,\mu$m long Au antenna ($I_3^{\mathrm{sam}}(\omega)$; blue) and via back reflection from the Au patch ($I_{\mathrm{DC}}^{\mathrm{ref}}(\omega)$; red). The interferograms were recorded on the positions marked by crosses in the inset of the panel c. The upper left inset shows the near-field amplitude image of the rod antenna recorded at the white light position (WLP), while the lower left inset displays the Au patch where the DC interferograms were recorded. (d) Nano-FTIR amplitude spectrum $\left(s_3^{\mathrm{sam}}(\omega), s_{\mathrm{DC}}^{\mathrm{ref}}(\omega)\right)$ obtained by inverse Fourier transformation of the recorded interferograms shown in panel c. (e) Corresponding phase spectrum $\left(\phi_3^{\mathrm{sam}}(\omega), \phi_{\mathrm{DC}}^{\mathrm{ref}}(\omega)\right)$ recorded with a spectral resolution of $12.5\,\mathrm{cm}^{-1}$.

To obtain near-field scattering spectra over a wide spectral range, we conducted the experiment under various settings of the broadband source (see Figure 5.1b), covering a range from 850 to 2200 cm^{-1}. The normalized spectra recorded on a 1.5 μm long antenna at different settings of the IRSC laser are shown in Figure 5.4. For better visualization of the complete spectrum of the rod antennas, we stitched together the individual spectra. The stitching protocol and the details of phase unwrapping are described below in Section 5.3.2. For the measurements presented in this chapter, we recorded a reference spectrum after each antenna measurement under similar measurement parameters (i.e., same tip, tapping amplitude, optical alignment, etc.) to minimize the impact of sample drift on the spectra. The spectra were recorded with a spectral resolution of 12.5 cm^{-1} and averaged over 40 spectra, with an acquisition time of approximately 5 minutes per antenna.

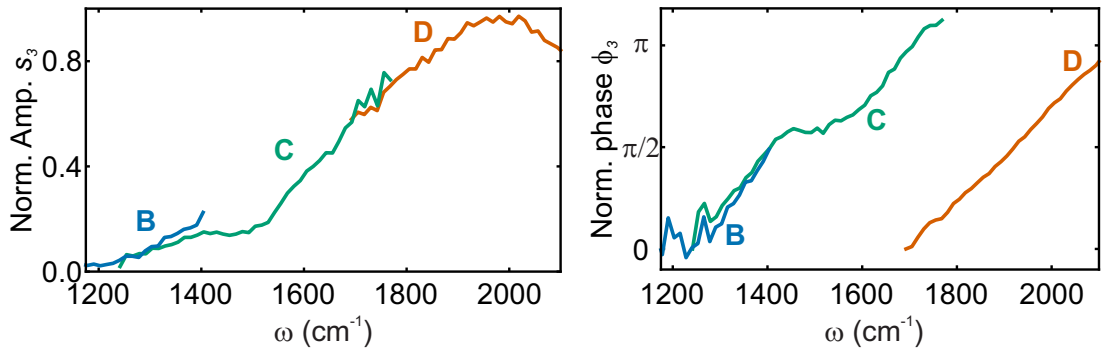

Figure 5.4.: **Normalized nano-FTIR spectra of rod antenna.** Normalized (a) amplitude $s_3(\omega)$ and (b) phase $\phi_3(\omega)$ spectra of a 1.5 μm long antenna, recorded at different settings of the IRSC laser indicated by B (blue), C (green), and D (orange) as shown in Figure 5.1 (b).

5.3.2. Stitching of nano-FTIR spectra

For better visualization of the full spectrum of the rod antenna structures, individual nano-FTIR spectra (as shown in Figure 5.4) recorded at different IRSC laser settings (see Figure 5.1b), were combined through a stitching algorithm. This process, applied to each pair of partially overlapping adjacent spectra, involves identifying the overlap region of the adjacent spectra and computing averages in this region to combine them.

To ensure a seamless transition between partially overlapping spectra, linear interpolation was employed before averaging the data in the overlap region. This step was necessary because the data points in the overlap region do not necessarily coincide on the x-axis (i.e., ω). By interpolating the data, averages can be calculated without introducing additional artifacts.

Additionally, to avoid stitching jumps (i.e., vertical dislocations due to discrepancies at the overlap region boundaries), each spectrum was extended with an additional data point from the adjacent spectrum outside the overlap region, effectively enlarging the overlap region. This modification ensures seamless alignment of the interpolated spectra at the borders of the overlap region, mitigating stitching jumps while preserving original data features. Alternatively, a weighting function as described in Reference [182] can also be employed to achieve similar results.

This stitching process was implemented using custom Python scripts, utilizing the NumPy and SciPy libraries for numerical operations. The methodology was validated with multiple data sets, confirming its robustness and reliability. As illustrated in Figure 5.5, the stitching procedures differ slightly for the near-field amplitude and phase spectra, a detailed description is provided below.

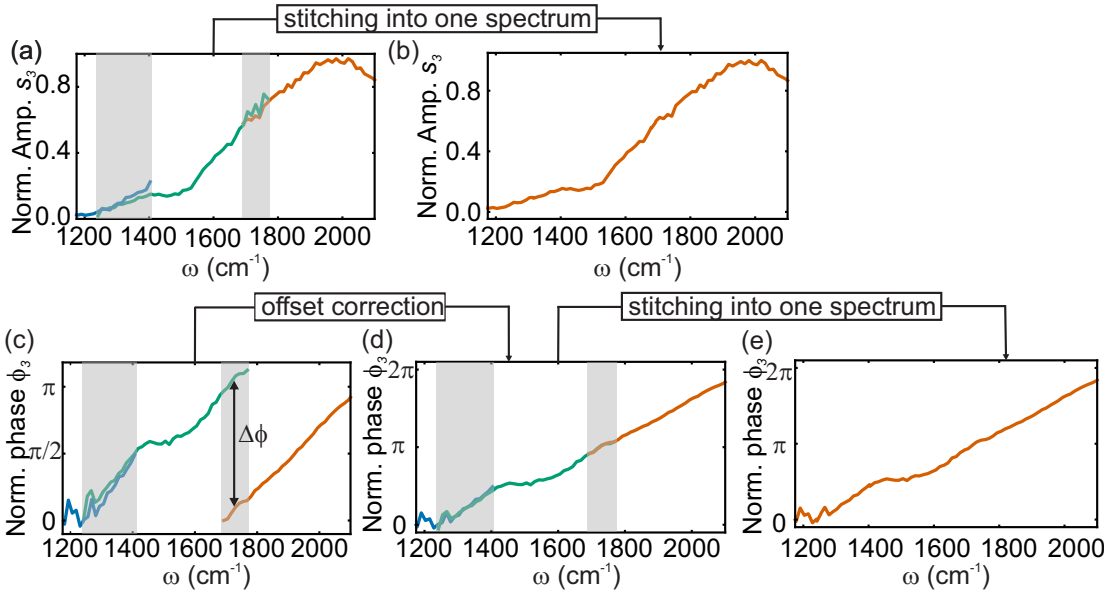

Figure 5.5.: **Stitching of nano-FTIR spectra** (a) Normalized nano-FTIR amplitude $s_3(\omega)$ spectra for a $1.5\,\mu$m long Au antenna recorded at three different settings of the IRSC laser and (b) broadband nano-FTIR amplitude spectra after stitching. (c) Normalized nano-FTIR phase ϕ_3 spectra of the same antenna at three different settings of the IRSC laser, (d) spectra after offset correction, and (e) broadband phase spectra after stitching. The spectral overlap region is marked by the gray shaded area.

Amplitude Spectra Stitching

For combining the adjacent amplitude spectra, average amplitude values were calculated in the overlap regions (marked by the gray shaded area in Figure 5.5a). The normalized amplitude spectra were stitched as follows:

$$s_{\text{stitch}}(\omega) = \begin{cases} s_1(\omega) & \text{for } \omega \in [\omega_{\min}, \omega_1] \\ \frac{1}{2}(s_1(\omega) + s_2(\omega)) & \text{for } \omega \in (\omega_1, \omega_2) \\ s_2(\omega) & \text{for } \omega \in [\omega_2, \omega_{\max}] \end{cases} \tag{5.3}$$

where $s_1(\omega)$ and $s_2(\omega)$ represent adjacent segments of the amplitude spectra, and $[\omega_1, \omega_2]$ represents the overlap region. An example of the stitched normalized nano-FTIR amplitude $s_3(\omega)$ spectra of a $1.5\,\mu\text{m}$ long rod antenna is shown in Figure 5.5(b).

Phase Spectra Stitching

Before combining adjacent phase spectra, phase unwrapping was applied to the individual normalized phase data. This procedure is essential for removing discontinuities (jumps of $\pm\pi$) inherent to the periodic nature of phase measurements. This is achieved by adding or subtracting multiples of 2π to the phase values, ensuring smooth variation in the overall phase [183]. Without phase unwrapping, the data exhibits jumps that can complicate the stitching procedure and compromise its accuracy.

In the subsequent step, it is necessary to correct for the phase offset $\Delta\varphi$ between adjacent spectra (illustrated in Figure 5.5c). This phase offset $\Delta\varphi$ can be attributed to fluctuations in the environmental conditions, such as temperature variations and air flow, causing a drift in the effective interferometer path length. The unwrapped and offset-corrected phase data can then be stitched together in a similar manner to the amplitude data, as follows:

$$\phi_{\text{stitch}}(\omega) = \begin{cases} \phi_1(\omega) & \text{for } \omega \in [\omega_{\min}, \omega_1] \\ \frac{1}{2}(\phi_1(\omega) + \phi_2(\omega) - \Delta\varphi) & \text{for } \omega \in (\omega_1, \omega_2) \\ \phi_2(\omega) - \Delta\varphi & \text{for } \omega \in [\omega_2, \omega_{\max}] \end{cases} \tag{5.4}$$

where, $\Delta\varphi$ is the difference between the average phases in the overlap region.

An example of the stitching of the normalized phase ϕ_3 spectra of a $1.5\,\mu\text{m}$ long rod antenna is shown in Figures 5.5c-e. The spectra after offset correction, and the broadband phase spectra post-stitching, are presented in Figures 5.5d and 5.5e, respectively. The spectral overlap region is marked by the shaded gray area.

5.4. Infrared spectroscopy of individual antennas

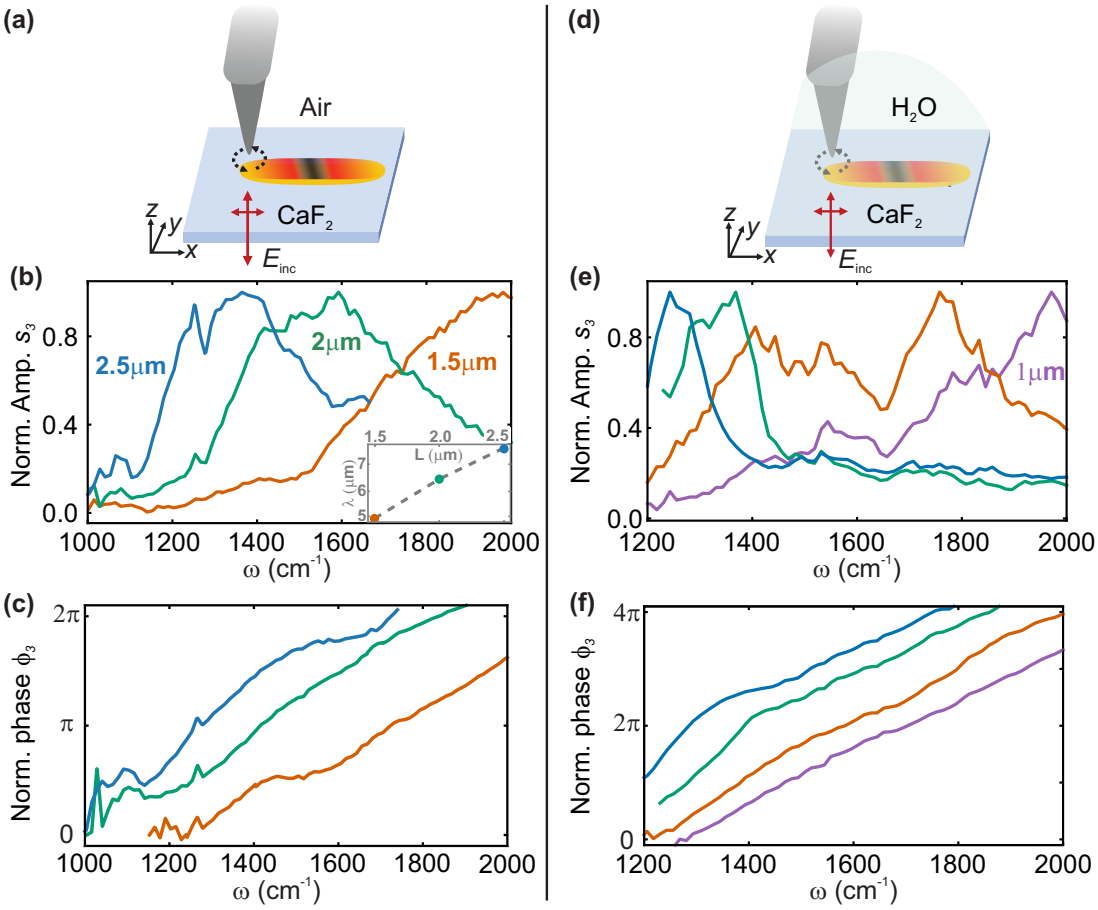

Figure 5.6.: **Nano-FTIR spectroscopy of individual Au rod antennas in air** ($L = 1.5 - 2.5\,\mu$m) **and in a liquid** ($L = 1 - 2.5\,\mu$m) **environment.** (a) Schematic of the tip illumination and scattering in air. The incident field E_{inc} is polarized along the long axis of the rod antenna. The inset to panel a shows the linear dependence of nanorod resonance (λ) with its length (L). Normalized (b) amplitude (s_3) and (c) phase (ϕ_3) spectra of metal rod antennas of different lengths, $L = 1 - 2.5\,\mu$m recorded in air. (d-f) Same as in panels a-c but similar antennas were probed in liquid (H_2O).

Metal rod antennas exhibit a dipolar resonance, visible as two bright spots at the edges of the antenna in near-field amplitude images (see Figure 5.2a). To demonstrate nano-FTIR spectroscopy of single antenna structures, we recorded nano-FTIR spectra on one of the

edges of gold (Au) rod antennas (see schematic in Figure 5.6a). The resulting spectra were recorded and normalized as described in Section 5.3.

In Figure 5.6b, c, we present the third harmonic of the normalized amplitude $s_3(\omega)$ and phase $\phi_3(\omega)$ spectra of rod antennas with lengths $L = 1.5 - 2.5\,\mu\mathrm{m}$, recorded in air. The near-field amplitude spectra $s_3(\omega)$ in Figure 5.6b show the typical fundamental resonance of the nanorods in the form of a broad peak, which shifts to lower frequencies (or higher wavelengths, λ) with increasing antenna length (L). Analogous to traditional radio wave antennas, the nanorod resonance wavelength (λ) follows a linear scaling with the length (L) of the nanorod, see inset to the Figure 5.6b. However, the antenna lengths (L) are significantly shorter than $\lambda/2$ [184] due to the relatively large width of the nanoantennas compared to its length and dielectric screening by the substrate [26, 185, 186].

Additionally, the near-field phase spectra $\phi_3(\omega)$ in Figure 5.6c show a transition from 0 to 2π as the fundamental resonance of the antenna is crossed. Specifically, the typical response of an antenna (i.e., a phase transition from 0 to π across the antenna resonance) is doubled owing to the double-scattering process between the antenna and the tip [28] (see also Chapter 4, Section 4.4).

We note that in addition to the fundamental antenna resonance, we observe the spectral signature of the vibrational resonance of polydimethylsiloxane (PDMS), a common contaminant found on commercial tips packed in gel boxes, specifically the Si-CH_3 vibration centered at $1258\,\mathrm{cm}^{-1}$. However, a detailed analysis of this field-enhanced molecular vibrational scattering goes beyond the scope of the current discussion and is thoroughly examined in Reference [162].

To demonstrate nano-FTIR spectroscopy of antennas in liquid, we recorded spectra of similar rod antennas with lengths $L = 1 - 2.5\,\mu\mathrm{m}$ in H_2O (see Figure 5.2d). As in air, we observe the fundamental nanorod resonance in liquid in the near-field amplitude spectra $s_3(\omega)$ in Figure 5.6e, which shifts to lower frequencies with increasing antenna length (L).

Upon comparing with the spectra recorded in air, two main observations can be made: First, the fundamental nanorod resonances undergo a red shift (i.e., shifted to lower frequencies) in H_2O for the same antenna lengths. This shift can be attributed to the higher refractive index of H_2O compared to air [169, 187]. Second, we observe a broad dip in the near-field amplitude spectra $s_3(\omega)$ at $\omega \sim 1660\,\mathrm{cm}^{-1}$, which can be attributed to the H_2O absorption, specifically the vibrational resonance of the H-O-H bending mode of H_2O [180]. Notably, unlike the spectra recorded in air, we do not observe the PDMS absorption peaks in the antenna spectra recorded in H_2O. This can be attributed to the additional cleaning protocol of the cantilevered AFM tips before operation in liquid environments (see Appendix A), stripping away parts of the PDMS contamination

along with other contaminants.

To better understand the impact of liquid (H_2O) on the near-field response of the antenna, we numerically calculated the out-of-plane component (E_z) of the near-field spectra of the rod antennas on a CaF_2 substrate in air and in H_2O (for details see Section 5.2.2). Figure 5.7 shows a comparison of the calculated near-field amplitude spectra (Figure 5.7b) with the experimentally recorded normalized near-field amplitude spectra $s_3(\omega)$ (Figure 5.7a) of a $1.5\,\mu m$ long rod antenna in air (red) and in H_2O (blue). The numerical calculations qualitatively reproduced the measured spectra, particularly the shape of the fundamental antenna resonances. The differences between the spectra recorded in air and H_2O can be fully attributed to the impact of the dielectric function of H_2O on the fundamental antenna resonance, specifically the vibrational resonance of the H-O-H bending mode of H_2O [180]. The discrepancy between the experimental and numerical data can be attributed to the small variations in the antenna geometry between the calculations and the experiment. The effect of demodulation of the scattered signal has also not been taken into account for these calculations.

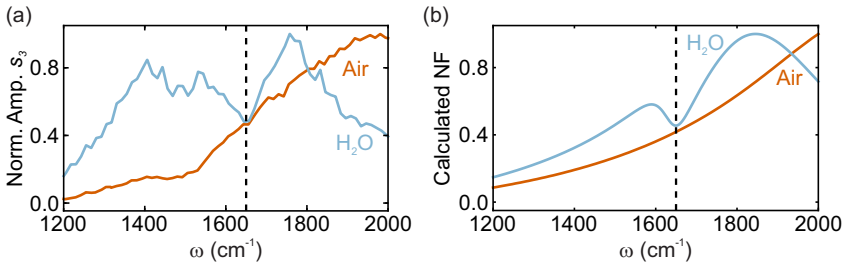

Figure 5.7.: **Impact of liquid on the near-field antenna response.** (a) Comparison of the normalized near-field amplitude spectra s_3 of a $1.5\,\mu m$ long rod antenna recorded in Air (red) and in H_2O(blue). Dashed black line indicates the dip associated with water absorption frequency centered at $1650\,cm^{-1}$. (b) Calculated out-of-plane component (E_z) of the near-field amplitude spectra of the same antenna in air and in H_2O. The near-field was calculated at a height of $50\,nm$ above the antenna surface at a distance of $100\,nm$ from one of the edges of the antenna. See details in Section 5.2.2

However, the near-field phase spectra $\phi_3(\omega)$ recorded in H_2O show a peculiar behavior compared to the phase spectra ($\phi_3(\omega)$) recorded in air. Unlike in air, where the near-field phase undergoes a transition from 0 to 2π as the fundamental resonance of the nanorod is crossed, in liquid, we observe a phase spanning from 0 to almost 4π. We suspect that this behavior is likely due to the absorption of the infrared light by H_2O, leading to stronger drifts between the tip and the sample, changes in the local temperature, and volume of the liquid droplet. These factors can lead to a strong baseline tilt in the phase spectra [45, 188]. In the future, better strategies need to be developed for baseline

correction in liquid-phase near-field spectroscopy to mitigate these effects and improve quantitative analysis.

5.5. Conclusions and outlook

In this chapter, we demonstrated the application of the normal incidence transflection nano-FTIR setup (described in detail in Chapter 4) for infrared spectroscopy of individual resonant plasmonic antennas in both air and liquid environments (specifically, H_2O). To this end, we established a reliable methodology for acquiring, normalizing, and stitching nano-FTIR spectra obtained using a bandwidth-limited IRSC laser, enabling reliable near-field spectroscopy over a broad spectral range.

Our results include detailed near-field measurements of the fundamental resonances of metal antennas in both air and liquid. Notably, we observed shifts in these resonances when transitioning from air to H_2O, owing to the higher refractive index of water. Additionally, we detected vibrational absorption features of H_2O in the near-field amplitude spectra, demonstrating the setup's efficacy in performing background-free, amplitude- and phase-resolved infrared nanospectroscopy in liquid environments. The experimental findings were supported by numerical simulations that qualitatively reproduced the near-field amplitude spectra and confirmed the observed antenna resonance shifts.

The developed transflection nano-FTIR spectroscopy setup offers significant potential for several applications, including in-depth studies of field-enhanced molecular scattering in both air [162] and liquid environments, refractive index sensing applications, and investigating coupling phenomena between individual objects with nanoscale resolution. This work lays the groundwork for further nano-FTIR based in-situ studies of plasmon enhanced chemical identification. Additional research focused on mitigating stabilization issues, particularly in liquid environments, are necessary to fully exploit these capabilities.

6. Total internal reflection-based s-SNOM for phonon polariton mapping in a liquid environment

Strongly confined surface polaritons allow for strong light-matter coupling and for highly sensitive analysis of (bio)chemical substances and processes. Nanoimaging of the polaritons' evanescent fields is critically important for experimental mode identification and field confinement studies. In this chapter, we demonstrate an application of the total internal reflection (TIR)-based s-SNOM and nano-FTIR setup described in Chapter 4 for nanoimaging and nanospectroscopy of polaritons in liquid. The s-SNOM tip is both launching and probing ultraconfined phonon polaritons in thin hexagonal boron nitride (h-BN) flakes, laying the foundation for s-SNOM-based polariton interferometry in liquid. Our results promise manifold applications, for example, in-situ studies of strong coupling between polaritons and molecular vibrations or chemical reactions at the bare or functionalized surfaces of polaritonic materials. The results presented in this chapter were previously published in Reference [112].

6.1. Introduction

Plasmon and phonon polaritons are electromagnetic modes formed by the coupling of light with dipolar excitations (light coupled to free charge carriers in metals and crystal lattice vibrations, respectively) in a material. Of particular interest are surface polaritons (propagating modes at the interface of two materials, one with positive and the other with negative dielectric permittivity) as they allow for highly confined and enhanced electromagnetic fields owing to their shorter wavelengths (compared to the free-space wavelength) and exponentially decaying field strengths perpendicular to the interface [189]. At infrared frequencies, where propagating plasmon polaritons are less confined, surface phonon polaritons could provide an alternative for polariton enhanced bio(chemical) sensing [190]. Recently, ultraconfined IR plasmon and phonon polaritons in van der Waals (vdW) materials such as graphene, hexagonal boron nitride (h-BN), and molybdenum trioxide (MoO_3) have attracted wide attention [30–32,34,191], as they promise ultracompact and highly sensitive devices for molecular vibrational spectroscopy for (bio)chemical analysis [192–195]. However, the majority of these

studies were performed in air. Considering that (bio)chemical processes often occur in liquid, it would be thus of great interest to explore the properties of ultraconfined vdW material polaritons in a liquid environment. For future exploitation, for example, in mid-IR biosensing applications, study of bio-molecular interactions, and chemical reactions in the liquid environment.

Graphene plasmons and phonon polaritons in polar vdW materials can be imaged in great detail by scattering-type scanning near-field optical microscopy (s-SNOM), photothermal expansion (PTE) microscopy, and photoinduced force microscopy (PiFM). So far, polariton imaging in the aqueous phase has been demonstrated only by PTE [117] and PiFM [196], although the interferometric detection scheme of s-SNOM offers many advantages, especially direct near-field phase measurements for retrieving phase and group velocities of polaritons [33] (see also Chapter 3, Section 3.1).

In this chapter, we describe an application of our total internal reflection (TIR)-based s-SNOM setup, which allows for efficient coupling of standard mid-IR Gaussian beams to the near-field probe to perform both tip-enhanced infrared nanoimaging and nanospectroscopy in a liquid environment (Section 6.2). In Section 6.3, we apply this setup for amplitude- and phase-resolved imaging of ultraconfined propagating phonon polaritons (PhPs) on h-BN flakes, yielding not only the polariton dispersion but also the sign of the phase velocity, the latter not being directly accessible by PTE microscopy. To further analyze the impact of liquid on the properties of phonon polaritons, we compare the polariton dispersion in liquid and in air. We further discuss potential applications of PhPs in liquid. In Section 6.4, we finally demonstrate nano-FTIR spectroscopy of ultraconfined phonon polaritons in liquid.

6.2. Experimental details

6.2.1. Sample preparation

We used ^{10}B monoisotopic h-BN [197]. The h-BN crystals were grown by the atmospheric pressure metal flux growth method, which is described in detail in References [198, 199].

For transferring the h-BN flakes onto the top surface of a ZnSe wedges (for details see Chapter 4, Section 4.3.3), we performed mechanical exfoliation of the h-BN crystals using blue Nitto tape (Nitto Europe NV, Genk, Belgium). Large and homogeneous h-BN flakes were isolated. We then performed a second exfoliation of the h-BN flakes from the tape directly onto the ZnSe substrate. Isolated homogeneous h-BN flakes were then used for the work presented in this chapter.

6.2.2. Experimental setup and phase drift correction

A detailed description of the TIR-based s-SNOM and nano-FTIR setups is presented in Chapter 4. For convenience, the experimental setup based on a modified neaSNOM (Neaspec, GmbH) is briefly described here.

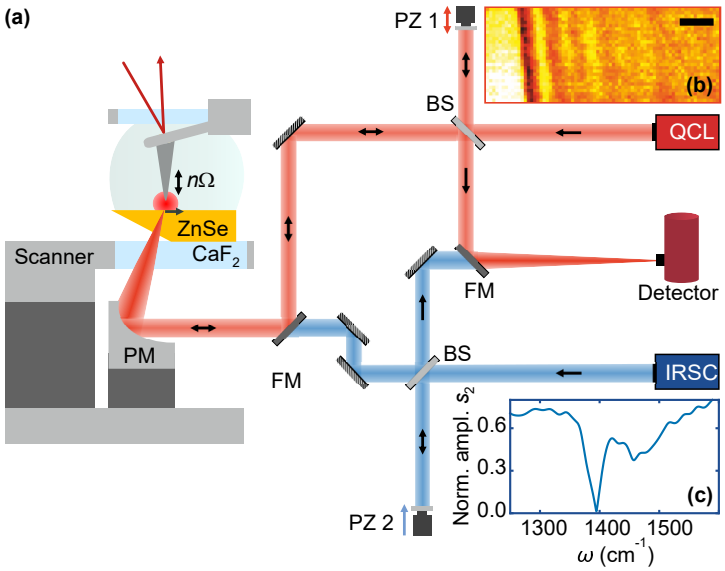

Figure 6.1.: **TIR-based s-SNOM and nano-FTIR setup for imaging and spectroscopy in air and liquid.** (a) Schematic of the setup for nanoimaging (s-SNOM) and nanospectroscopy (nano-FTIR). For s-SNOM, the tip is illuminated with a frequency-tunable QCL. The back-scattered light is demodulated at a higher harmonic of the tip's oscillation frequency, $n\Omega$, and recorded with a pseudo-heterodyne Michelson interferometer (top). BS, beamsplitter; PZ1, piezo actuated vibrating mirror. For nano-FTIR, the tip is illuminated with an infrared supercontinuum (IRSC) broadband laser. The back-scattered light is analyzed using an asymmetric Fourier transform spectrometer (bottom). PZ2, piezo actuated translating mirror; FM, flip mirror. (b) Example of an s-SNOM amplitude image s_3. Scale bar: $500\,\mathrm{nm}$. (c) Example of a nano-FTIR amplitude spectrum.

For nanoimaging (Figure 6.1a, top), the tip is illuminated with a frequency-tunable quantum cascade laser (QCL, Daylight Solutions Inc.). The back-scattered field is recorded with a pseudo-heterodyne Michelson interferometer as a function of the tip position yielding near-field amplitude (shown in Figure 6.1b) and phase images, s_n and ϕ_n, respectively.

Note that scanning the ZnSe wedge in y-direction (see Figure 6.2) yields a constant phase drift, which has been subtracted from all the phase imaged presented in this

chapter. An example of the phase drift correction process is shown in Figure 6.2. A detailed description is provided in Chapter 4, Section 4.5.1.

For nano-FTIR spectroscopy (Figure 6.1a, bottom), the tip is illuminated with the broadband infrared radiation from a difference frequency generated laser supercontinuum (frequency range $= 1200 - 1700\,\mathrm{cm}^{-1}$, average power $= 500\,\mu\mathrm{m}$). The back-scattered light is recorded with an asymmetric Fourier transform spectrometer, yielding amplitude (shown in Figure 6.1c) and phase spectra of the sample, $s_n(\omega)$ and $\phi_n(\omega)$, after normalization to reference spectra recorded on the bare substrate (ZnSe).

As a liquid we used D_2O instead of H_2O, as its absorption within the frequency range of the broadband laser emission ($1200 - 1700\,\mathrm{cm}^{-1}$; required for h-BN polariton mapping) is lower than for H_2O [121, 122]. Stronger absorption leads to faster evaporation of the liquid, causing increased instabilities in the AFM operation.

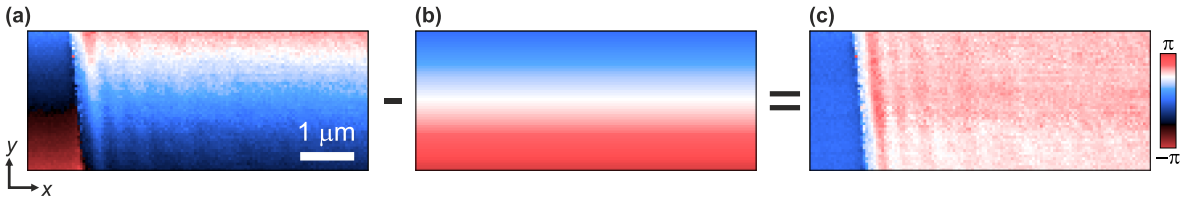

Figure 6.2.: **Phase drift correction.** (a) Near-field phase ϕ_3 image recorded at $1486\,\mathrm{cm}^{-1}$, superimposed by constant phase drift caused by the effective beam path change along the y-direction during imaging. (b) Calculated phase correction $\exp(ik_y y)$, where $k_y = 1.2\,\mu\mathrm{m}^{-1}$. (c) Corrected phase image obtained after subtracting the calculated phase correction in panel b from raw phase image in panel a.

6.3. Infrared nanoimaging of phonon polaritons in a liquid environment

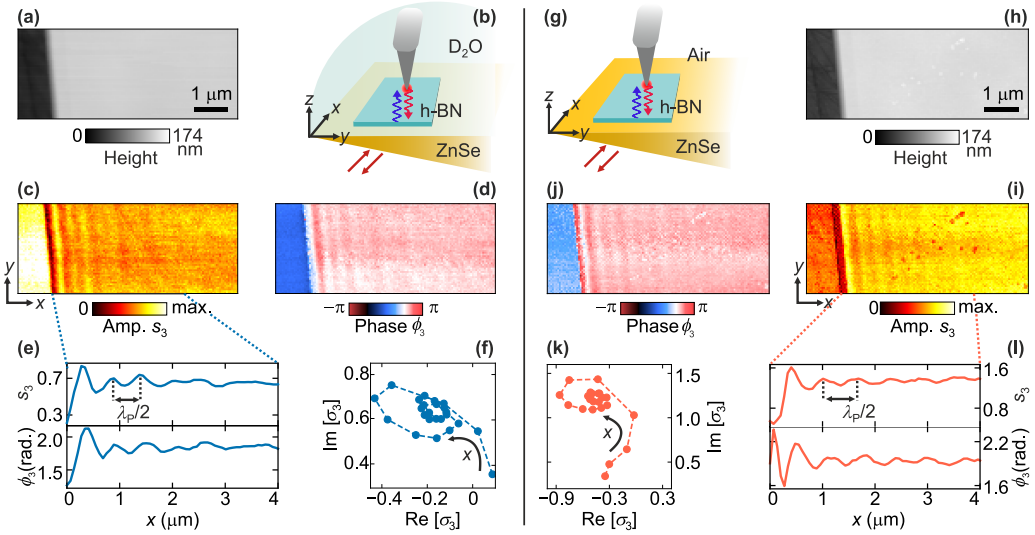

Figure 6.3.: **Amplitude- and phase-resolved imaging of h-BN PhPs in liquid (a–f) and air (g–l).** (a) AFM topography of a 110 nm thick h-BN flake recorded in D_2O. (b) Schematic of s-SNOM in liquid. (c, d) Near-field amplitude and phase images recorded at 1486 cm^{-1} in D_2O, revealing a standing wave pattern caused by the PhP interference. (e) Amplitude and phase line profiles extracted perpendicular to the h-BN edge (averaged over 50 lines), revealing a fringe spacing of $\lambda_P/2$. (f) Phasor diagram of the complex-valued near-field signal $\sigma_3 = s_3 \exp(i\phi_3)$, indicating a positive phase velocity of h-BN PhPs launched in D_2O. (g–l) Same as panels a–f, but probing was done in the air.

We demonstrate the imaging of hyperbolic phonon polaritons (PhPs) in liquid by mapping an isolated h-BN flake on a ZnSe wedge (see Section 6.2.1). The topography image in Figure 6.3a clearly shows the smooth surface of the 110 nm thick h-BN flake with little noise, indicating a stable tapping mode AFM operation in the liquid. In the simultaneously recorded amplitude s_3 and phase ϕ_3 images at 1486 cm^{-1} (Figures 6.3c-d), we observe fringes on the h-BN surface, which are parallel to the h-BN edge, similar to s-SNOM observations of h-BN PhPs in air [32, 200]. The fringes can be explained by the interference of PhPs, as illustrated in Figure 6.3b. Typically, the interference of tip-launched PhPs that reflect at the flake edge yields standing wave patterns, leading to a fringe spacing of $\lambda_P/2$, where λ_P is the wavelength of the phonon polaritons. Importantly, and in contrast to PTE measurements of phonon polaritons in liquid, amplitude and

phase mapping enabled by s-SNOM allows us to directly determine the phase velocity of PhPs in a liquid. To that end, we extract amplitude and phase line profiles (Figure 6.3e) from the images and plot them in the complex plane (phasor diagram, Figure 6.3f). An anticlockwise rotation is observed, corresponding to positive phase velocity with increasing tip edge distance x. For comparison, we imaged the same flake at the same IR frequency in the air (Figures 6.3g-l). The images look similar, but the fringe spacing in the infrared images recorded in the air is slightly larger than in the images recorded in a liquid. This is expected, as D_2O has a higher permittivity compared to air, thus acting as a dielectric load [117]. Dielectric materials are well-known and understood to reduce the polariton wavelength with increasing permittivity [201, 202].

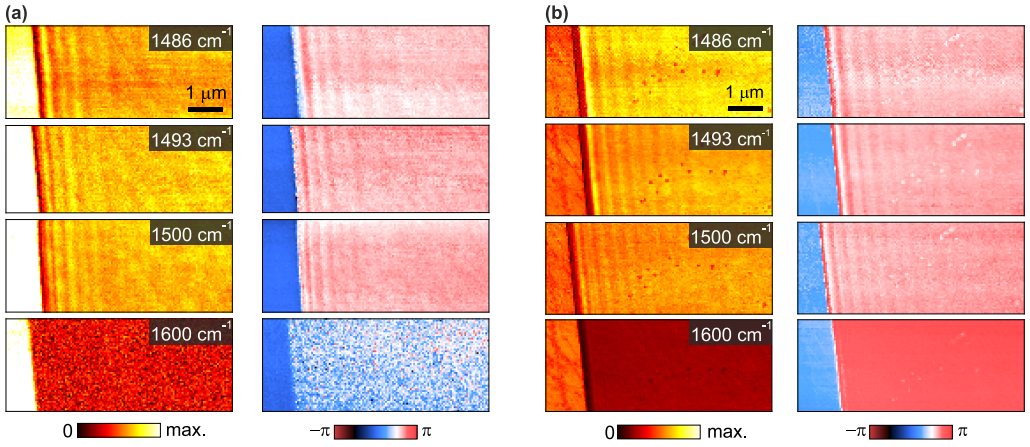

Figure 6.4.: **s-SNOM nanoimaging in liquid and air.** (a) Near-field amplitude (left) and phase (right) images of h-BN PhPs launched at different frequencies in liquid. (b) Images recorded for the same flake at varying frequencies in air.

For a quantitative analysis and comparison of the phonon polariton properties in liquid and air, we imaged the h-BN flake at different frequencies (the amplitude and phase images are shown in Figure 6.4). Figure 6.5a and 6.5c shows amplitude images recorded in air and liquid, respectively. To measure the polariton momentum $q = {}^{2\pi}/_{\lambda_P}$ at each frequency, we extracted line profiles perpendicular to the h-BN edge, and Fourier transformed them. The corresponding PhP momenta are plotted in Figure 6.5b (symbols), clearly showing the systematic shift of the experimental dispersion to higher wavevectors when the h-BN is imaged in a liquid. Between $1500\,\mathrm{cm}^{-1}$ and $1600\,\mathrm{cm}^{-1}$, we did not observe fringes, which we attribute to the low signal-to-noise (S/N) ratio at these frequencies and to the increasing confinement of the PhPs. The latter does not allow for observing polaritons at $1600\,\mathrm{cm}^{-1}$, despite a reasonable S/N ratio. We confirm our observations by calculating (see Appendix B) the dispersion of the fundamental PhP

mode (in literature often denoted M0 [32,33]) of an h-BN flake on ZnSe in either D_2O or air (blue and red curves in Figure 6.5b). The experimental data (symbols) and the calculated dispersion (lines) are in good agreement with each other for an h-BN thickness of 90 nm, which is smaller than the experimental h-BN thickness, which we attribute to uncertainties in the height measurements and permittivities of h-BN and ZnSe.

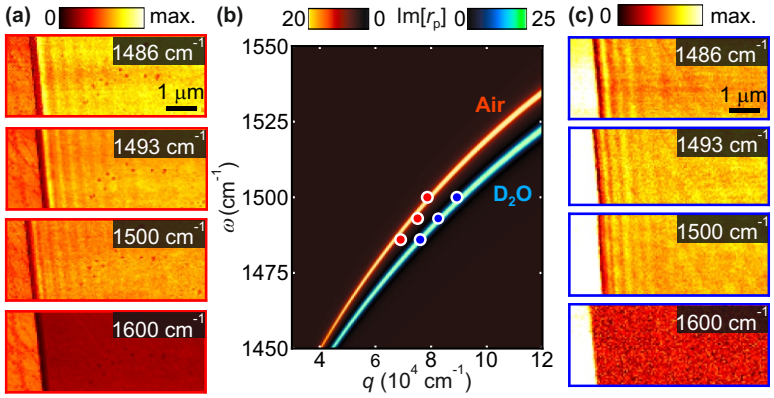

Figure 6.5.: **Dispersion of h-BN PhPs in liquid and air .** (a) Near-field amplitude images s_3 of an h-BN flake in air. (b) Dispersion of h-BN PhPs. Symbols show PhP momenta obtained from line profiles taken from the images shown in panels a and c. The color plot indicates the calculated imaginary part of the momentum- and frequency-dependent Fresnel reflection coefficient, $\mathrm{Im}[r_p]$, of a 90 nm thick h-BN flake on ZnSe in air (red) and D_2O (blue). (c) Near-field amplitude images s_3 of an h-BN flake in a liquid environment.

To further quantify the shift of the polariton momentum, and in turn the wavelength, we calculated λ_P as a function of the dielectric permittivity of the surrounding media, ϵ_m, at $1480\,\mathrm{cm}^{-1}$ (see Appendix B). We observe a significant decrease of λ_P with increasing ϵ_m (Figure 6.6). A change from air ($\epsilon_m = 1$) to a liquid of ($\epsilon_m = 3$) yields a polariton wavelength compression of about 236 nm, corresponding to about 23% and a sensitivity of $(\Delta\lambda_P/\Delta n_m = 323\,\mathrm{nm/RIU})$, where $\Delta\lambda_P$ is the wavelength change upon a refractive index change of Δn_m. Such fluid-control of the polariton wavelength in 2D materials could find interesting application potential for the development of reconfigurable polariton devices. s-SNOM operating in liquid – as demonstrated in this work – in the future can be applied for fundamental studies and for verification of corresponding device concepts.

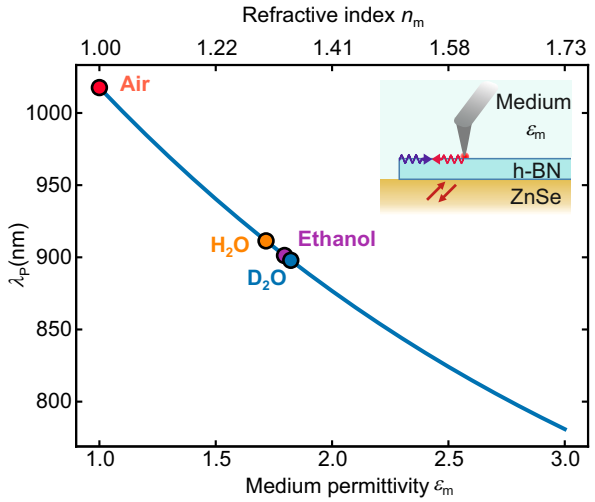

Figure 6.6.: **Fluid control of PhP wavelength .** PhP wavelength λ_P as a function of the dielectric permittivity of the surrounding medium, ϵ_m , calculated for a $90\,nm$ thick h-BN slab on a $ZnSe$ substrate at $1480\,cm^{-1}$. Inset shows the sample sketch. Symbols indicate various liquids (for references, see Appendix B.2).

As an application example, we discuss the use of s-SNOM in liquid for studying vibrational strong coupling (VSC) between molecules and polaritons. Generally, VSC leads to new hybrid polariton modes, whose coherent exchange of energy is faster than the decay rate of the original modes [203,204], and can modify chemical reactions [205,206]. Recently, molecular vibrational strong coupling involving h-BN phonon polaritons was observed by s-SNOM polariton interferometry [207], analogous to Figure 6.8, but in air. In Figure 6.7 we show by calculations how a liquid environment modifies VSC. The inset of Figure 6.7 shows the calculated dispersion (See Appendix B) of the fundamental phonon polariton mode (red dashed lines, $\epsilon_m = 1$) when a $30\,nm$ thick layer of CBP $(4,4' - bis\,(N - carbauolyl) - 1,1' - biphenyl)$ molecules is placed on top of a $30\,nm$ thick h-BN layer. It reveals VSC by a splitting of the phonon polariton mode into an upper and lower polariton branch (red solid lines) [207] at the molecular vibrational frequency $(1450\,cm^{-1})$, marked by horizontal dashed line, associated with the $C - H$ deformation bond of CBP [208]. By adding liquid above the molecular layer, we find that VSC is maintained and even enhanced (blue and green curves in Figure 6.7), as the mode splitting (minimum distance between upper and lower polariton branch) and the coupling strength $g \approx \Omega/2$ increases with increasing permittivity ϵ_m of the liquid. This finding can be explained by the increased polariton momentum in liquid (see Figure 6.5), which is accompanied by an increased field confinement near the h-BN surface. This, in turn, yields a stronger overlap between the phonon polariton mode volume and the

molecule layer, enhancing the light-matter coupling. As, generally, chemical reactions and dynamics often require liquid environment, polariton imaging by s-SNOM in liquid opens up new possibilities for studying VSC involving ultra-confined polaritons.

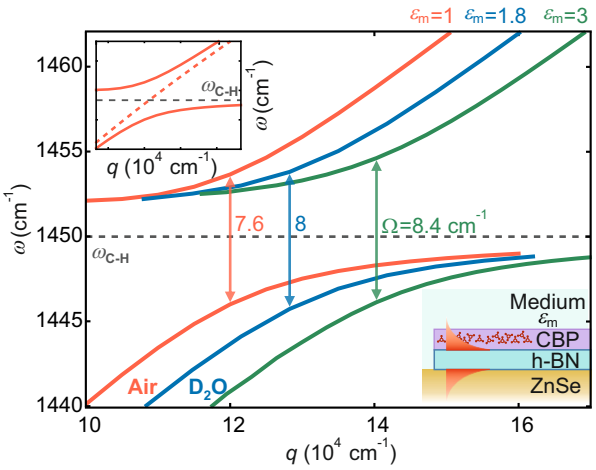

Figure 6.7.: **Fluid control of vibrational strong coupling (VSC) .** Calculated dispersion of the fundamental hybrid polariton mode of a $30\,\mathrm{nm}$ thick h-BN slab covered with a $30\,\mathrm{nm}$ thick layer of CBP molecules, which is covered by liquids of different dielectric permittivities: $\epsilon_\mathrm{m} = 1$ (air, red curves), $\epsilon_\mathrm{m} = 1.82$ (D_2O , blue curves), and $\epsilon_\mathrm{m} = 3$ (green curves). Upper left inset: Comparison of the hybrid polariton mode in the air (red solid curves) with the fundamental phonon polariton mode of an h-BN slab in the air without molecules (red dashed curve). Lower right inset: Sketch of the sample. Gray horizontal dashed lines mark the molecular vibrational frequency $\omega_{\mathrm{C-H}}$. Vertical arrows indicate the mode splitting Ω.

6.4. Nano-FTIR spectral line scan of phonon polaritons in liquid

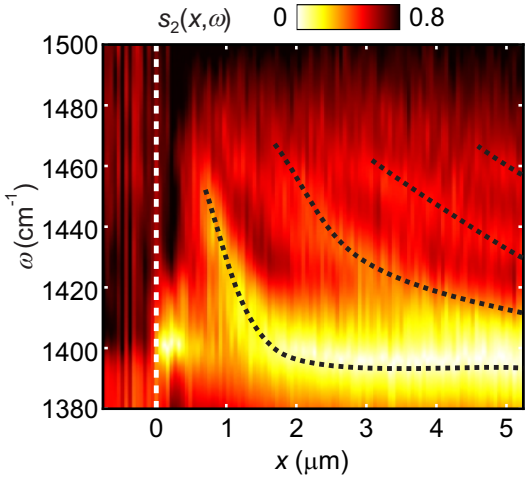

Figure 6.8.: **Nano-FTIR spectral line scan of h-BN in liquid.** (a) Nano-FTIR line scan perpendicular to the h-BN edge (indicated by the dashed vertical line), showing the near-field amplitude signal as a function of frequency, ω, and distance, x, between the tip and the h-BN edge, $s_2(x, \omega)$. Black dashed lines are guides to the eye, tracing the interference fringes. Spectral resolution: $14\,\mathrm{cm}^{-1}$. Total acquisition time: $\sim 1\,\mathrm{h}$ and $20\,\mathrm{min}$.

We finally demonstrate experimentally nano-FTIR spectroscopic imaging in liquid. To that end, we recorded a line scan perpendicular to the edge of the h-BN flake. Figure 6.8 shows the normalized nano-FTIR amplitude spectra as a function of tip position x. We clearly see a horizontal bright feature centered at $1395\,\mathrm{cm}^{-1}$, which corresponds to the h-BN phonon resonance. More interestingly, we observe fringes, which we attribute to a PhP interference pattern, as the fringe spacing $\lambda_P/2$ decreases continuously with increasing frequency. We find a good qualitative agreement to similar data sets recorded in air [32]. Figure 6.8 clearly demonstrates that hyperspectral nano-FTIR imaging of ultraconfined polaritons in a liquid is possible. However, we refrain from a quantitative analysis of this data set, as the required long data acquisition time (1 h and 20 min) and significant sample heating led to strong sample drift during nano-FTIR recording. In future developments and applications, this challenge of sample drift can be tackled by improving the thermal stability of the setup and employing drift correction strategies [182]. Furthermore, the heating of the liquid could be reduced by employing heat sinks or implementing flow cells instead of the simple liquid droplet used in the presented work. We finally note that dielectric (materials) contrasts (e.g., between h-BN

and ZnSe) obtained with our setup in the liquid differ from those in air. Future studies are required to explore this phenomenon, which could be caused by the illumination of the tip by both propagating and evanescent fields due to a non optimal prism geometry (due to space restrictions in our current setup) or enhanced higher mechanical harmonic generation in a liquid.

6.5. Conclusions and outlook

To summarize, we demonstrated the application of TIR-based s-SNOM for nanoimaging and spectroscopy of ultraconfined h-BN phonon polaritons in a liquid, showing that the presence of liquid shifts the PhP dispersion to higher momenta. In the future, one could exploit polariton interferometry in liquid (pure solutions or buffer solutions containing specific molecules) for studying chemical interactions at the interface between the bare or functionalized polaritonic materials. We further envision in-situ studies of vibrational strong coupling between ultraconfined polaritons and molecular vibrations. Finally, we note that the TIR setup could be further optimized for standard s-SNOM and nano-FTIR based chemical mapping and identification of samples that are fully immersed in a liquid environment. The first step in this direction has been previously demonstrated in Chapter 4, Section 4.5. The physical and chemical properties of the liquid should allow for stable AFM operation, and the liquid's infrared absorption should not obscure the near-field response of the sample. Apart from using water-based buffer solutions for biochemical studies, low viscosity ionic liquids could be used for gating 2D materials and for studying phase transitions induced by ionic substitution.

A. Protocol for AFM and s-SNOM operation in liquid

AFM in liquid is a widely utilized technique for high-resolution surface characterization of materials such as polymers, biomolecules, and nanocomposites [57]. However, operating tapping mode AFM in liquid can pose significant challenges. The resolution and sensitivity of AFM in liquid are largely influenced by the tip-sample interaction which depends on both the characteristics of the tip (such as its chemical composition, cantilever dimensions, and force constant) and on the imaging conditions (including the imaging environment, scan parameters like tapping amplitude and feedback parameters) [209]. The presence of liquid can significantly alter the behavior of the oscillating cantilever (Chapter 4, Section 4.3.1). Thus, careful selection of imaging parameters and AFM tips is often essential for stable operation in liquid. Here, we provide a detailed protocol for operating tapping mode AFM (and s-SNOM) in liquid, specifically tailored to the setup used in this work.

A.1. Tool and surface cleaning

To achieve stable and high-resolution imaging in liquid environments, it is crucial to limit contamination of the tip-sample system. This step is vital not only for optimal imaging performance, but also ensures the longevity of both the samples and the AFM tips. Therefore, it is generally recommended to thoroughly clean all tools and surfaces that may come into contact with the tip, sample, or liquid. Additionally, wearing nitrile gloves during the cleaning and sample handling process is essential for minimizing contamination.

1. **Cleaning tweezers:** The tweezers used for handling the cantilevers and the samples were cleaned by soaking them in acetone. After soaking, the tweezers were allowed to either air dry or dry completely under a nitrogen flow.
2. **Cleaning substrates and sample holder:** The base of the substrates (CaF_2 and $ZnSe$), and the windows of the sample and the cantilever holder (CaF_2) (see Figures 4.2, 4.3 in Chapter 4) were cleaned before and after use in liquid. To clean these surfaces, we used a lint-free lens cleaning tissue soaked in isopropyl

alcohol (IPA or isoproponol). Each surface was wiped thoroughly and then dried completely under nitrogen flow to prevent any residue or contamination.

A.2. Cantilever and tip cleaning

Cantilevered AFM tips are often contaminated with organic and inorganic contaminants arising from storage in gel boxes, or from adsorption of contaminants from air [210]. These contaminants can negatively affect tip-sample contact in liquids, as they directly impact the wetting properties of the tip, often rendering AFM tips hydrophobic [211]. Additionally, larger contaminants can cause air bubbles to form on the AFM cantilever (see Figure A.1), distorting the reflection of the deflection laser from the backside of the cantilever impeding AFM operation. Therefore, it is essential to clean all cantilevers before use in liquid.

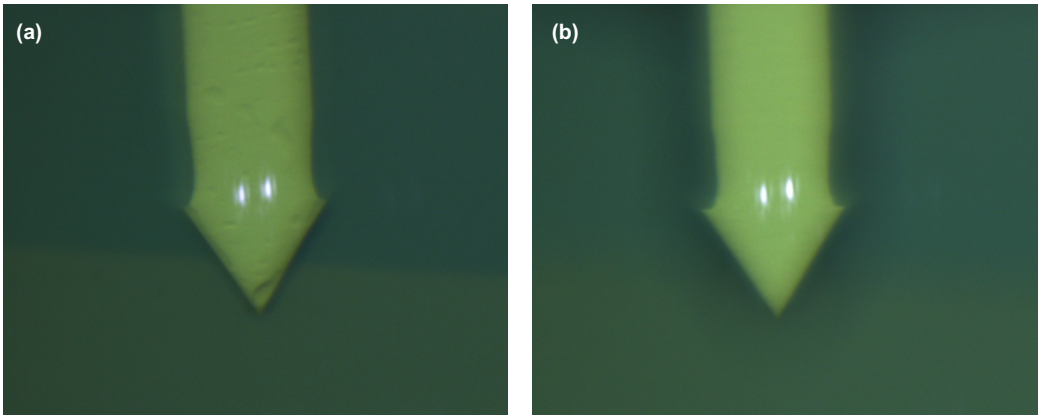

Figure A.1.: **Cantilever cleaning.** Comparison of contaminated AFM cantilever in liquid (a) before and (b) after the cleaning process.

For the work presented in this thesis, the cantilevers were cleaned using the following procedure:

1. The cantilevers were immersed in ethanol for approximately 30-60 seconds, followed by immersion in acetone for another 30-60 seconds. During the immersion, the cantilevers were continuously swirled around using a clean pair of tweezers to ensure thorough cleaning.
2. After cleaning, the cantilevers were immediately transferred to a thick lint free filter paper and were allowed to air dry completely before gluing them onto the cantilever holder. For temporary storage after cleaning, the cantilevers were placed in a clean, covered glass petri dish.

In addition to the method described above, more advanced AFM cantilever cleaning techniques are available that can further enhance image quality and significantly eliminate majority of the contaminants. However, caution is necessary when selecting a cleaning method, as harsher cleaning agents can compromise the integrity of the metallic coating on both the tip and the back of the cantilever. This metallic coating is crucial for optimal AFM and s-SNOM performance.

A.3. Sample mounting and liquid cell preparation

We use an open liquid cell concept (see Figure 4.2 in Chapter 4) for all the results presented in this thesis.

To prepare the setup for operation in liquid, a cleaned cantilever was glued onto the cantilever holder (see Figure 4.3a in Chapter 4). Next, using either a syringe or a micro pipette, a small droplet of liquid (approximately $50 - 100\,\mu\mathrm{L}$) was carefully placed directly on top of the cantilever. This ensures that both the cantilever and the tip are fully submerged in liquid. This step is crucial, as it helps minimize the formation of air bubbles during the sample's approach to the tip, facilitating a smoother approach process (see Section A.4).

Following that, the sample along with the Teflon block was glued onto the $\mathrm{CaF_2}$ window integrated on the sample holder (see Figures 4.2b, 4.3 in Chapter 4). To enable easy refilling of the liquid between measurements, a syringe fitted with a microfluidic tube was attached to the Teflon block. To ensure a steady flow of liquid, it is important to eliminate air bubbles from the tube and the syringe. To this end, before connecting the tube to the Teflon block, a small volume of the liquid was rapidly pushed through the syringe into the tube to displace any trapped air. After this, an additional droplet of liquid was formed on the top surface of the sample using the same syringe.

Due to the refilling mechanism and the hydrophobic nature of the ZnSe wedged substrates used in our experiments, large relative motion between the tip and the sample during quick positioning and approach can cause the droplet to slide off the substrate's surface. To prevent leakages and retain the liquid in place, many AFM systems employ O-rings in open liquid cells. However, due to space limitations and the current design of our setup, we created a barrier at the edges of the substrate using a two-component reprorubber mix. Once dried, this reprorubber acts as a flexible barrier that can be easily peeled off from the substrate with minimal damage or contamination.

A.4. Approach and scanning in liquid

The sample table and the cantilever were prepared and mounted on the setup. To focus the deflection laser on the back side of the cantilever, the cantilever was moved downwards (in the z direction, see Figure A.2e) until a sharp spot from the deflection laser was visible (see Figure A.2f). Note that the focal plane in liquid is significantly lower (closer to sample table) than in air, which requires careful adjustment. The sample table is positioned just above the parabolic mirror to avoid any collisions during the cantilever height adjustment.

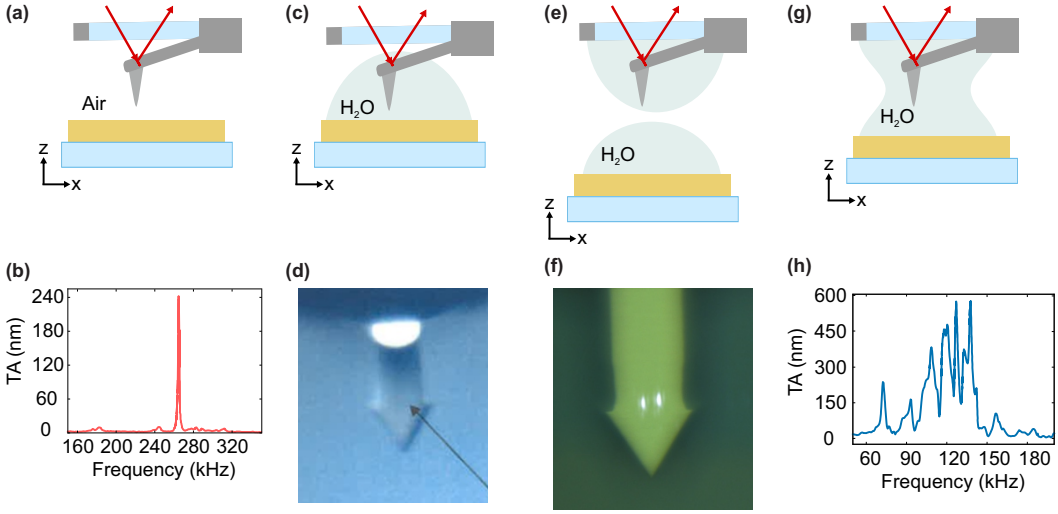

Figure A.2.: **Cantilever tuning and approach in liquid**. (a) Illustration of a cantilevered AFM tip in air. (b) Frequency response spectrum of a commercially available Pt-Ir cantilevered tip recorded in air showing a single pronounced peak corresponding to the cantilever's fundamental resonance frequency. TA, tapping amplitude. (c) Illustration showing the cantilever and sample immersed in liquid, with the CaF_2 window positioned just above the droplet. (d) Absence of the deflection laser spot on the backside of the cantilever for the scenario depicted in panel c. (e) A droplet of liquid is formed on both the cantilever and the top surface of the sample prior to approach, (f) enabling optimal focusing and visibility of the deflection laser spot on the backside of the cantilever. (g) A capillary bridge is created as the sample is brought closer to the tip. (h) Frequency response spectrum of the same tip as in panel b, but in liquid, showing multiple peaks referred to as "forest of peaks".

Once the cantilever was placed in the focus of the deflection laser, the sample table was

raised slowly (in z direction, see Figure A.2e) until a capillary bridge formed between the liquid droplets on the tip and the sample (see Figure A.2g). Once the tip and the sample are in close proximity, the frequency response spectrum of the cantilever was recorded in liquid (see Figure A.2h). The presence of liquid significantly dampens the cantilever oscillation and introduces multiple spurious peaks in its frequency response spectrum (see discussion in Chapter 4 in Section 4.3.1). This complicates the identification of the optimal drive frequency for stable AFM. To navigate the complexities of AFM operation in liquid, the following guidelines are recommended:

1. **Drive voltage:** The resonance frequency of the cantilever in liquid is typically around one-third of the value in air. Generally, a higher drive voltage is essential for optimal tuning of the cantilever resonance (due to increased effective mass of the cantilever in liquid, see Chapter 4 in Section 4.3.1). Initially, a very high drive voltage was applied to identify the correct cantilever resonance frequency before it was lowered to achieve the desired tapping amplitude. For example, for the frequency responses shown in Figures A.2b (air) and A.2h (H_2O) we used drive voltages of approximately $20\,\mathrm{mV}$ in air and $1000\,\mathrm{mV}$ in H_2O to record the cantilever frequency response.

2. **Selection of cantilever resonance:** Due to the presence of multiple peaks in the frequency response spectrum of the cantilever in liquid, identifying the optimal drive frequency often involves a trial-and-error process at first. However, since the cantilever frequency response is dependent on the cantilever properties and the geometry of the liquid cell (see discussion in Chapter 4, Section 4.3.1), once the optimum frequency has been identified for a setup, it can serve as a reference for future measurements. Typically for our setup, a $\mathrm{Pt-Ir}$ (Arrow NCPt, Nanoworld) cantilevered tip operates optimally at frequencies around $105-130\,\mathrm{kHz}$. To identify the optimum drive frequency, a practical approach is to bring the tip close to the sample surface and compare its frequency response with data obtained at a greater distance from the sample. The peaks, whose amplitude remains constant between the two measurements, can be ignored right away. Next focus on the remaining peaks. It is important to note that the tallest peak is not always the best choice for stable operation. Select a peak and gradually approach the tip onto a clean and flat area of the sample while carefully monitoring the mechanical signals until an optimal frequency is identified.

3. **Approach in liquid:** Once a frequency was selected for operation, the setpoint was fixed to approximately 80% of the free oscillation amplitude of the cantilever. Monitoring the mechanical amplitude signal can also help confirm if the selected frequency is optimal. As an example, a trace of the mechanical amplitude signal during approach for two of the peaks (highlighted in the inset to the Figure A.3a and A.3b) in the cantilever frequency spectrum is shown in Figure A.3. Ideally,

the mechanical signal should decrease steadily as the tip slowly approaches the sample until the tip snaps into contact with the sample surface (Figure A.3a). In contrast, when operating at a non-optimum frequency the mechanical signal remains nearly constant until a sudden snap occurs as it contacts the sample (sharp kink before contact in (Figure A.3b)).

4. **Scanning in liquid:** As in air, the most critical parameters for scanning with AFM in liquid are the setpoint and feedback gain.

   a) **Setpoint:** The setpoint value directly correlates to the force applied by the AFM tip onto the sample. Usually a higher setpoint indicates larger tip-sample distance resulting in a lower tip-sample interaction force on the sample. In contrast, a lower setpoint indicates smaller tip-sample distances and consequently higher force on the sample. When measuring soft samples and/or in liquid, setpoint values of $80 - 90\%$ of the free tapping amplitude are a good starting point for scanning to minimize sample damage and tip contamination. While scanning in liquid, it is common to gradually reduce the setpoint to compensate for the steady decrease in the tapping amplitude, which occurs due to the cantilever bending in liquid. This bending is often a result of the variations in the temperature of the liquid. Therefore, it is advisable to perform a few blank scans (i.e., scans over a large topography-free area of the sample) before proceeding to the area of interest.

   b) **Feedback gain**: The feedback gain reflects how quickly the feedback loop responds to changes in topography. The feedback loop (that maintains oscillation amplitude while scanning the sample) can be optimized by adjusting the proportional-integral (PI) gains. The integral gain has the most dramatic effect on the image quality. A high value means faster response time but may introduce instability and electronic noise to the image. We began by setting a low integral gain value and gradually increased it, while scanning until a clear image was observed. After optimizing the integral gain, the proportional gain was fine tuned (start low and increase gradually) until an improvement in the image quality without introducing additional noise was observed. A good approach to fine-tune the PI gains is to monitor the trace and retrace of the mechanical amplitude signals while scanning and adjusting the gains until a high level of correlation is observed between the two curves. Figure A.4, presents an AFM topography image of a polymer (PMMA) layer on a ZnSe substrate in liquid, demonstrating the significance of selecting optimal scan parameters. If scan parameters are poorly chosen, it can lead to instabilities in scanning, potential damage the sample, and tip and liquid contamination leading to complications in interpreting AFM and s-SNOM measurements.

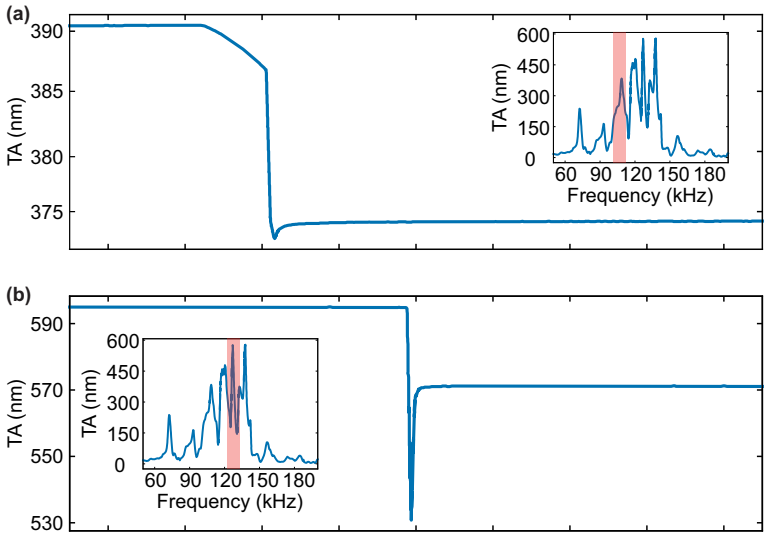

Figure A.3.: **Mechanical amplitude signal trace while the tip approaches the sample.** The mechanical response for two conditions (a) at the optimum peak and (b) at a spurious peak in the cantilever's frequency response. Insets in panels a and b show the frequency response spectrum of a $\mathrm{Pt-Ir}$ (Arrow NCPt, Nanoworld) cantilevered tip in $\mathrm{H_2O}$, with the highlighted regions indicating the selected peaks used for AFM operation. TA, tapping amplitude.

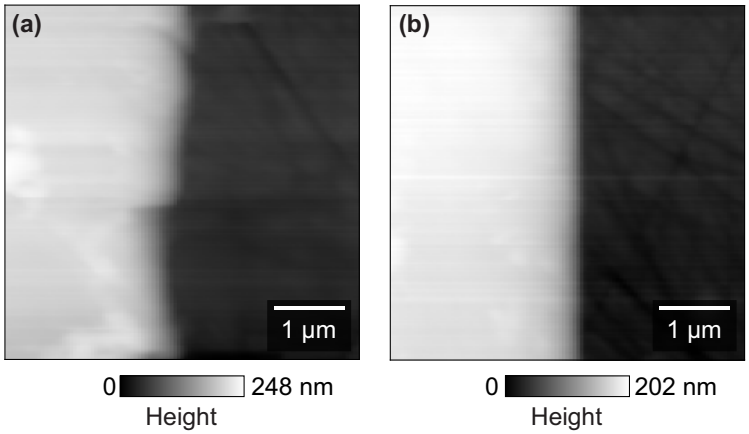

Figure A.4.: **Parameters for scanning in a liquid environment.** (a) Illustration of poorly optimized scanning parameters, resulting in abrupt jumps in AFM topography measurement, as well as potential damage and dragging of the sample by the AFM tip. (b) AFM topography image of the same sample imaged with optimized scanning parameters, demonstrating a clear topography image of a PMMA layer on ZnSe.

B. Phonon polariton wavelength and dispersion calculation

The calculations were performed by Andrei Bylinkin at CIC Nanogune BRTA.

We used the transfer matrix formalism [212] to calculate the Fresnel reflection coefficient r_{p} of the layered sample. The color plot shown in Figure 6.5b in Chapter 6 shows the imaginary part of the Fresnel reflection coefficient, $\mathrm{Im}\,(r_{\mathrm{p}})$, calculated for h-BN layer on ZnSe in either air or $\mathrm{D_2O}$.

The polariton dispersions shown in Figure 6.7 in Chapter 6 were obtained by determining the poles of r_{p}. To determine the poles, we numerically solved the equation $1/\mathrm{Abs}(r_{\mathrm{p}}) = 0$. We considered complex frequencies $\omega - i\gamma$ and real momenta q , i.e., determined the poles of $r_{\mathrm{p}}\,(q, \omega - i\gamma)$, yielding the polariton frequency $\omega(q)$ and the mode splitting Ω.

The polariton wavelengths in Figure 6.6 and the PhP dispersion of the bare h-BN layer in Figure 6.5 b and in the inset to Figure 6.7 (dashed red line) in Chapter 6 were calculated by quasi-normal mode analysis using the COMSOL mode solver, where infinitely extended h-BN layers of a given thickness on top of a ZnSe substrate were considered. We extracted the mode index $\frac{q}{q_0} + {}^{ik}/_{q_0}$, which is the complex-valued wavevector normalized to the photon momentum q_0. The polariton wavelength follows from $\lambda_{\mathrm{P}} = \frac{2\pi}{q}$. The dielectric permittivity of h-BN, CBP, ZnSe and liquids used for the calculations are described below.

B.1. h-BN dielectric function

The dielectric permittivity of $^{10}\mathrm{B}$ monoisotopic h-BN was calculated with a Lorentz model according to

$$\epsilon_{\text{h-BN},j}\,(w) = \epsilon_{\infty,j}\left(\frac{\omega_{\mathrm{LO},j}^2 - \omega^2 - i\omega\Gamma_j}{\omega_{\mathrm{TO},j}^2 - \omega^2 - i\omega\Gamma_j}\right),$$

where $j = \perp, \parallel$ indicate the direction of the tensor with respect to the anisotropy axis. $\omega_{\mathrm{LO},j}^2$ and $\omega_{\mathrm{TO},j}^2$ are the LO and TO phonon frequencies, Γ is the damping constant and $\epsilon_{\infty,j}$ is the high frequency permittivity. The h-BN parameters used for the calculations

were taken from Reference [213]: $\omega_{\mathrm{LO},\perp} = 1650\,\mathrm{cm}^{-1}$, $\omega_{\mathrm{LO},\parallel} = 845\,\mathrm{cm}^{-1}$, $\omega_{\mathrm{TO},\perp} = 1394.5\,\mathrm{cm}^{-1}$, $\omega_{\mathrm{TO},\parallel} = 785\,\mathrm{cm}^{-1}$, $\Gamma_\perp = 1.8\,\mathrm{cm}^{-1}$, $\Gamma_\parallel = 1\,\mathrm{cm}^{-1}$, and $\epsilon_{\infty,\perp} = 4.5$ (instead of 5.1 as in Reference [213]) to better match our experimental results.

B.2. Substrate and liquid dielectric constants

For the dispersion calculations shown in Figure 6.5b and 6.7, as well as for the calculation of the polariton wavelengths in Figure 6.6 in Chapter 6, the following dielectric constants ($\sqrt{\epsilon} = n$) for an incident wavelength of $\lambda \approx 6\,\mu\mathrm{m}$ were used: $\epsilon_{\mathrm{ZnSe}} = 5.76$ (Reference [152]), $\epsilon_{\mathrm{D_2O}} = 1.82$ (Reference [122]), $\epsilon_{\mathrm{H_2O}} = 1.716$ (Reference [122])), $\epsilon_{\mathrm{Ethanol}} = 1.796$ (Reference [214]).

B.3. CBP dielectric function

To extract the dielectric function of CBP $(4,4' - \mathrm{bis}\,(N - \mathrm{carbauolyl}) - 1,1' - \mathrm{biphenyl})$ we followed the approach described in Reference [207], where the so-called Tinkham formula [215] for thin films on a substrate was used to relate the transmission of the CBP film to its complex-valued conductivity and permittivity. To fit the transmission data, we modeled the dielectric function of the CBP molecules with the Drude-Lorentz model assuming 4 oscillators to describe all the dips in the transmission spectra of the CBP layer in the frequency range from 1400 to $1550\,\mathrm{cm}^{-1}$ according to

$$\epsilon_{\mathrm{CBP}}(\omega) = \epsilon_\infty + \sum_k \frac{\omega_{\mathrm{p,k}}^2}{\omega_{0,k}^2 - \omega^2 - i\Gamma_{\mathrm{CBP},k}\omega},$$

$k = 1 - 4$, where ϵ_∞ is the high-frequency dielectric constant. $\omega_{\mathrm{p},k}$, $\omega_{0,k}$, and $\Gamma_{\mathrm{CBP},k}$ represent the plasma frequency, resonance frequency and linewidth of the kth Lorentz oscillator, respectively. For the central frequency and width of the absorption associated with the $\mathrm{C-H}$ deformation bond, which is the CBP vibration used for studying vibrational strong coupling in this work, we obtained $\omega_{0,k} = 1450\,\mathrm{cm}^{-1}$, $\omega_{\mathrm{p},k} = 128\,\mathrm{cm}^{-1}$, and $\Gamma_{\mathrm{CBP},k} = 6.4\,\mathrm{cm}^{-1}$, assuming $\epsilon_\infty = 2.8$ (Reference [208]).

Bibliography

[1] J. M. Chalmers and P. R. Griffiths, *Handbook of vibrational spectroscopy*, vol. 4, Wiley, 2002.

[2] L. P. Keller, S. Bajt, G. A. Baratta, J. Borg, J. P. Bradley, D. E. Brownlee, H. Busemann, J. R. Brucato, M. Burchell, L. Colangeli, and Others, *Infrared spectroscopy of comet 81P/Wild 2 samples returned by Stardust*, Science **314** (2006), no. 5806, 1728–1731.

[3] C. Petibois and G. Déléris, *Chemical mapping of tumor progression by FT-IR imaging: towards molecular histopathology*, TRENDS in Biotechnology **24** (2006), no. 10, 455–462.

[4] A. Barth, *Infrared spectroscopy of proteins*, Biochimica et Biophysica Acta (BBA)-Bioenergetics **1767** (2007), no. 9, 1073–1101.

[5] K. Nishikida, E. Nishio, and R. W. Hannah, *Selected applications of modern FT-IR techniques*, CRC Press, 2019.

[6] M. Born and E. Wolf, *Principles of optics*, 1999.

[7] F. Zenhausern, M. P. O'boyle, and H. K. Wickramasinghe, *Apertureless near-field optical microscope*, Applied Physics Letters **65** (1994), no. 13, 1623–1625.

[8] F. Keilmann and R. Hillenbrand, *Nano-optics and near-field optical microscopy*, Artech House, London, 2008.

[9] A. V. Zayats and D. Richards, *Nano-optics and near-field optical microscopy*, Artech House, 2009.

[10] M. B. Raschke and C. Lienau, *Apertureless near-field optical microscopy: Tip-sample coupling in elastic light scattering*, Applied Physics Letters **83** (2003), no. 24, 5089–5091.

[11] T. Taubner, R. Hillenbrand, and F. Keilmann, *Performance of visible and mid-infrared scattering-type near-field optical microscopes*, Journal of microscopy **210** (2003), no. 3, 311–314.

[12] F. Keilmann, A. J. Huber, and R. Hillenbrand, *Nanoscale Conductivity Contrast by Scattering-Type Near-Field Optical Microscopy in the Visible, Infrared and THz Domains*, Journal of Infrared, Millimeter, and Terahertz Waves **30** (2009), no. 12, 1255–1268.

[13] F. Keilmann and R. Hillenbrand, *Near-field microscopy by elastic light scattering from a tip*, Philosophical Transactions of the Royal Society A: Mathematical, Physical and Engineering Sciences **362** (2004), no. 1817, 787–805.

[14] A. A. Govyadinov, I. Amenabar, F. Huth, P. Scott Carney, and R. Hillenbrand, *Quantitative measurement of local infrared absorption and dielectric function with tip-enhanced near-field microscopy*, Journal of Physical Chemistry Letters **4** (2013), no. 9, 1526–1531.

[15] T. Taubner, R. Hillenbrand, and F. Keilmann, *Nanoscale polymer recognition by spectral signature in scattering infrared near-field microscopy*, Applied Physics Letters **85** (2004), no. 21, 5064–5066.

[16] F. Huth, A. Govyadinov, S. Amarie, W. Nuansing, F. Keilmann, and R. Hillenbrand, *Nano-FTIR absorption spectroscopy of molecular fingerprints at 20 nm spatial resolution*, Nano Letters **12** (2012), no. 8, 3973–3978.

[17] S. Amarie, P. Zaslansky, Y. Kajihara, E. Griesshaber, W. W. Schmahl, and F. Keilmann, *Nano-FTIR chemical mapping of minerals in biological materials*, Beilstein Journal of Nanotechnology **3** (2012), no. 1, 312–323.

[18] F. Huth, M. Schnell, J. Wittborn, N. Ocelic, and R. Hillenbrand, *Infrared-spectroscopic nanoimaging with a thermal source*, Nature Materials **10** (2011), no. 5, 352–356.

[19] H. A. Bechtel, E. A. Muller, R. L. Olmon, M. C. Martin, and M. B. Raschke, *Ultrabroadband infrared nanospectroscopic imaging*, Proceedings of the National Academy of Sciences of the United States of America **111** (2014), no. 20, 7191–7196.

[20] C. Westermeier, A. Cernescu, S. Amarie, C. Liewald, F. Keilmann, and B. Nickel, *Sub-micron phase coexistence in small-molecule organic thin films revealed by infrared nano-imaging*, Nature Communications **5** (2014), 1–6.

[21] M. Brehm, T. Taubner, R. Hillenbrand, and F. Keilmann, *Infrared spectroscopic mapping of single nanoparticles and viruses at nanoscale resolution*, Nano Letters **6** (2006), no. 7, 1307–1310.

[22] I. Amenabar, S. Poly, W. Nuansing, E. H. Hubrich, A. A. Govyadinov, F. Huth, R. Krutokhvostov, L. Zhang, M. Knez, J. Heberle, A. M. Bittner, and R. Hillenbrand, *Structural analysis and mapping of individual protein complexes by infrared nanospectroscopy*, Nature Communications **4** (2013).

[23] A. J. Huber, F. Keilmann, J. Wittborn, J. Aizpurua, and R. Hillenbrand, *Terahertz near-field nanoscopy of mobile carriers in single semiconductor nanodevices*, Nano Letters **8** (2008), no. 11, 3766–3770.

[24] J. M. Stiegler, A. J. Huber, S. L. Diedenhofen, J. Gómez Rivas, R. E. Algra, E. P. Bakkers, and R. Hillenbrand, *Nanoscale free-carrier profiling of individual semiconductor nanowires by infrared near-field nanoscopy*, Nano Letters **10** (2010), no. 4, 1387–1392.

[25] A. C. Jones, R. L. Olmon, S. E. Skrabalak, B. J. Wiley, Y. N. Xia, and M. B. Raschke, *Mid-IR plasmonics: Near-field imaging of coherent plasmon modes of silver nanowires*, Nano Letters **9** (2009), no. 7, 2553–2558.

[26] M. Schnell, A. García-Etxarri, A. J. Huber, K. Crozier, J. Aizpurua, and R. Hillenbrand, *Controlling the near-field oscillations of loaded plasmonic nanoantennas*, Nature Photonics **3** (2009), no. 5, 287–291.

[27] P. Alonso-González, M. Schnell, P. Sarriugarte, H. Sobhani, C. Wu, N. Arju, A. Khanikaev, F. Golmar, P. Albella, L. Arzubiaga, F. Casanova, L. E. Hueso, P. Nordlander, G. Shvets, and R. Hillenbrand, *Real-space mapping of Fano interference in plasmonic metamolecules*, Nano Letters **11** (2011), no. 9, 3922–3926.

[28] P. Alonso-González, P. Albella, M. Schnell, J. Chen, F. Huth, A. García-Etxarri, F. Casanova, F. Golmar, L. Arzubiaga, L. E. Hueso, J. Aizpurua, and R. Hillenbrand, *Resolving the electromagnetic mechanism of surface-enhanced light scattering at single hot spots*, Nature Communications **3** (2012).

[29] V. A. Zenin, R. Malureanu, I. P. Radko, A. V. Lavrinenko, and S. I. Bozhevolnyi, *Near-field characterization of bound plasmonic modes in metal strip waveguides*, Optics Express **24** (2016), no. 5, 4582.

[30] J. Chen, M. Badioli, P. Alonso-González, S. Thongrattanasiri, F. Huth, J. Osmond, M. Spasenović, A. Centeno, A. Pesquera, P. Godignon, A. Zurutuza Elorza, N. Camara, F. J. García, R. Hillenbrand, and F. H. Koppens, *Optical nano-imaging of gate-tunable graphene plasmons*, Nature **487** (2012), no. 7405, 77–81.

[31] Z. Fei, A. S. Rodin, G. O. Andreev, W. Bao, A. S. McLeod, M. Wagner, L. M. Zhang, Z. Zhao, M. Thiemens, G. Dominguez, M. M. Fogler, a. H. C. Neto, C. N. Lau, F. Keilmann, D. N. Basov, A. H. Castro Neto, C. N. Lau, F. Keilmann, and D. N. Basov, *Gate-tuning of graphene plasmons revealed by infrared nano-imaging*, Nature **487** (2012), no. 7405, 82–85.

[32] S. Dai, Z. Fei, Q. Ma, A. S. Rodin, M. Wagner, A. S. McLeod, M. K. Liu, W. Gannett, W. Regan, K. Watanabe, T. Taniguchi, M. Thiemens, G. Dominguez, A. H. Castro Neto, A. Zettl, F. Keilmann, P. Jarillo-Herrero, M. M. Fogler, and D. N. Basov, *Tunable phonon polaritons in atomically thin van der Waals crystals of boron nitride*, Science **343** (2014), no. 6175, 1125–1129.

[33] E. Yoxall, M. Schnell, A. Y. Nikitin, O. Txoperena, A. Woessner, M. B. Lundeberg, F. Casanova, L. E. Hueso, F. H. Koppens, and R. Hillenbrand, *Direct observation*

of ultraslow hyperbolic polariton propagation with negative phase velocity, Nature Photonics **9** (2015), no. 10, 674–678.

[34] D. N. Basov, M. M. Fogler, and F. J. García De Abajo, *Polaritons in van der Waals materials*, Science **354** (2016), no. 6309.

[35] O. Khatib, J. D. Wood, A. S. McLeod, M. D. Goldflam, M. Wagner, G. L. Damhorst, J. C. Koepke, G. P. Doidge, A. Rangarajan, R. Bashir, E. Pop, J. W. Lyding, M. H. Thiemens, F. Keilmann, and D. N. Basov, *Graphene-based platform for infrared near-field nanospectroscopy of water and biological materials in an aqueous environment*, ACS Nano **9** (2015), no. 8, 7968–7975.

[36] Y. H. Lu, J. M. Larson, A. Baskin, X. Zhao, P. D. Ashby, D. Prendergast, H. A. Bechtel, R. Kostecki, and M. Salmeron, *Infrared Nanospectroscopy at the Graphene-Electrolyte Interface*, Nano Letters **19** (2019), no. 8, 5388–5393.

[37] L. M. Meireles, I. D. Barcelos, G. A. Ferrari, P. A. A. Paulo Alexandre, R. O. Freitas, and R. G. Lacerda, *Synchrotron infrared nanospectroscopy on a graphene chip*, Lab on a Chip **19** (2019), no. 21, 3678–3684.

[38] K. J. Kaltenecker, T. Gölz, E. Bau, and F. Keilmann, *Infrared-spectroscopic, dynamic near-field microscopy of living cells and nanoparticles in water*, Scientific Reports **11** (2021), no. 1, 1–12.

[39] E. Baù, T. Gölz, M. Benoit, A. Tittl, and F. Keilmann, *Nanoscale Mechanical Manipulation of Ultrathin SiN Membranes Enabling Infrared Near-Field Microscopy of Liquid-Immersed samples*, Small **2402568** (2024), 1–10.

[40] T. Gölz, E. Baù, J. Zhang, K. Kaltenecker, D. Trauner, S. A. Maier, F. Keilmann, T. Lohmüller, and A. Tittl, *Transient infrared nanoscopy resolves the millisecond photoswitching dynamics of single lipid vesicles in water*, arXiv preprint arXiv:2406.02513 (2024).

[41] B. T. O'Callahan, K. D. Park, I. V. Novikova, T. Jian, C. L. Chen, E. A. Muller, P. Z. El-Khoury, M. B. Raschke, and A. S. Lea, *In Liquid Infrared Scattering Scanning Near-Field Optical Microscopy for Chemical and Biological Nanoimaging*, Nano Letters **20** (2020), no. 6, 4497–4504.

[42] J. Heberle and E. Pfitzner, *Infrared scattering-type scanning near-field optical microscopy of biomembranes in water*, Journal of Physical Chemistry Letters **11** (2020), no. 19, 8183–8188.

[43] J. Mertz, *Introduction to optical microscopy*, Cambridge University Press, 2019.

[44] B. Herman and J. J. Lemasters, *Optical microscopy: emerging methods and applications*, Elsevier, 2012.

[45] P. R. Griffiths and J. A. De Haseth, *Fourier transform infrared spectrometry*, vol. 171, John Wiley & Sons, 2007.

[46] B. Schrader, *Infrared and Raman spectroscopy: methods and applications*, John Wiley & Sons, 2008.

[47] L. Novotny and B. Hecht, *Principles of nano-optics*, Cambridge university press, 2012.

[48] E. Abbe, *Beiträge zur Theorie des Mikroskops und der mikroskopischen Wahrnehmung*, Archiv für Mikroskopische Anatomie **9** (1873), no. 1, 413–468.

[49] E. Meyer, H. J. Hug, and R. Bennewitz, *Scanning probe microscopy*, vol. 4, Springer, New York, 2003.

[50] G. Binnig, C. F. Quate, and C. Gerber, *Atomic Force Microscope*, Physical Review Letters **56** (1986), no. 9, 930–933.

[51] O. Sahin, S. Magonov, C. Su, C. F. Quate, and O. Solgaard, *An atomic force microscope tip designed to measure time-varying nanomechanical forces*, Nature Nanotechnology **2** (2007), no. 8, 507–514.

[52] F. Rico, C. Su, and S. Scheuring, *Mechanical mapping of single membrane proteins at submolecular resolution*, Nano Letters **11** (2011), no. 9, 3983–3986.

[53] E. T. Herruzo, A. P. Perrino, and R. Garcia, *Fast nanomechanical spectroscopy of soft matter*, Nature Communications **5** (2014), no. 1.

[54] A. Majumdar, *SCANNING THERMAL MICROSCOPY*, Annual Review of Materials Science **29** (1999), no. 1, 505–585.

[55] R. A. Oliver, *Advances in AFM for the electrical characterization of semiconductors*, Reports on Progress in Physics **71** (2008), no. 7.

[56] R. García and R. Perez, *Dynamic atomic force microscopy methods*, Surface Science Reports **47** (2002), no. 6-8, 197–301.

[57] P. Eaton and P. West, *Atomic force microscopy*, Oxford university press, 2010.

[58] B. Drake, C. B. Prater, A. L. Weisenhorn, S. A. Gould, T. R. Albrecht, C. F. Quate, D. S. Cannell, H. G. Hansma, and P. K. Hansma, *Imaging crystals, polymers, and processes in water with the atomic force microscope*, Science **243** (1989), no. 4898, 1586–1589.

[59] F. Moreno-Herrero, J. Colchero, J. Gómez-Herrero, and A. M. Baro, *Atomic force microscopy contact, tapping, and jumping modes for imaging biological samples in liquids*, Physical Review E - Statistical, Nonlinear, and Soft Matter Physics **69** (2004), no. 3 1, 1–9.

[60] Y. Gan, *Atomic and subnanometer resolution in ambient conditions by atomic force microscopy*, Surface Science Reports **64** (2009), no. 3, 99–121.

[61] F. J. Giessibl, *Surface by Atomic Force Microscopy*, Science **267** (1995), no. 13, 68.

[62] Y. Sugawara, M. Ohta, H. Ueyama, and S. Morita, *Defect motion on an InP(110) surface observed with noncontact atomic force microscopy*, Science **270** (1995), no. 5242, 1646–1648.

[63] F. J. Giessibl, S. Hembacher, H. Bielefeldt, and J. Mannhart, *Subatomic features on the silicon (111)-(7x7) surface observed by atomic force microscopy*, Science **289** (2000), no. 5478, 422–425.

[64] A. Dazzi, F. Glotin, and R. Carminati, *Theory of infrared nanospectroscopy by photothermal induced resonance*, Journal of Applied Physics **107** (2010), no. 12.

[65] A. Dazzi, C. B. Prater, Q. Hu, D. B. Chase, J. F. Rabolt, and C. Marcott, *AFM-IR: Combining atomic force microscopy and infrared spectroscopy for nanoscale chemical characterization*, Applied Spectroscopy **66** (2012), no. 12, 1365–1384.

[66] F. Lu, M. Jin, and M. A. Belkin, *Tip-enhanced infrared nanospectroscopy via molecular expansion force detection*, Nature Photonics **8** (2014), no. 4, 307–312.

[67] D. Nowak, W. Morrison, H. K. Wickramasinghe, J. Jahng, E. Potma, L. Wan, R. Ruiz, T. R. Albrecht, K. Schmidt, J. Frommer, D. P. Sanders, and S. Park, *Nanoscale chemical imaging by photoinduced force microscopy*, Science Advances **2** (2016), no. 3.

[68] A. A. Michelson, *XXVIII. Visibility of interference-fringes in the focus of a telescope*, The London, Edinburgh, and Dublin Philosophical Magazine and Journal of Science **31** (1891), no. 190, 256–259.

[69] A. A. Michelson, *Light waves and their uses*, vol. 2, University of Chicago Press, 1903.

[70] A. A. Govyadinov, S. Mastel, F. Golmar, A. Chuvilin, P. S. Carney, and R. Hillenbrand, *Recovery of permittivity and depth from near-field data as a step toward infrared nanotomography*, ACS Nano **8** (2014), no. 7, 6911–6921.

[71] M. Wagner, A. S. McLeod, S. J. Maddox, Z. Fei, M. Liu, R. D. Averitt, M. M. Fogler, S. R. Bank, F. Keilmann, and D. N. Basov, *Ultrafast dynamics of surface plasmons in InAs by time-resolved infrared nanospectroscopy*, Nano Letters **14** (2014), no. 8, 4529–4534.

[72] M. Eisele, T. L. Cocker, M. A. Huber, M. Plankl, L. Viti, D. Ercolani, L. Sorba, M. S. Vitiello, and R. Huber, *Ultrafast multi-terahertz nano-spectroscopy with sub-cycle temporal resolution*, Nature Photonics **8** (2014), no. 11, 841–845.

[73] P. Hermann, A. Hoehl, P. Patoka, F. Huth, E. Rühl, and G. Ulm, *Near-field imaging and nano-Fourier-transform infrared spectroscopy using broadband synchrotron radiation*, Optics Express **21** (2013), no. 3, 2913.

[74] S. C. Kehr, M. Cebula, O. Mieth, T. Härtling, J. Seidel, S. Grafström, L. M. Eng, S. Winnerl, D. Stehr, and M. Helm, *Anisotropy contrast in phonon-enhanced apertureless near-field microscopy using a free-electron laser*, Physical Review Letters **100** (2008), no. 25, 1–4.

[75] Y. F. Dufrêne, T. Ando, R. Garcia, D. Alsteens, D. Martinez-Martin, A. Engel, C. Gerber, and D. J. Müller, *Imaging modes of atomic force microscopy for application in molecular and cell biology*, Nature Nanotechnology **12** (2017), no. 4, 295–307.

[76] D. G. Yablon, A. Gannepalli, R. Proksch, J. Killgore, D. C. Hurley, J. Grabowski, and A. H. Tsou, *Quantitative viscoelastic mapping of polyolefin blends with contact resonance atomic force microscopy*, Macromolecules **45** (2012), no. 10, 4363–4370.

[77] E.-C. Spitzner, C. Riesch, and R. Magerle, *Subsurface imaging of soft polymeric materials with nanoscale resolution*, Acs Nano **5** (2011), no. 1, 315–320.

[78] N. Balke, S. Jesse, A. N. Morozovska, E. Eliseev, D. W. Chung, Y. Kim, L. Adamczyk, R. E. Garcia, N. Dudney, and S. V. Kalinin, *Nanoscale mapping of ion diffusion in a lithium-ion battery cathode*, Nature nanotechnology **5** (2010), no. 10, 749–754.

[79] M. Stark, C. Möller, D. J. Müller, and R. Guckenberger, *From images to interactions: High-resolution phase imaging in tapping-mode atomic force microscopy*, Biophysical Journal **80** (2001), no. 6, 3009–3018.

[80] A. F. Payam, J. R. Ramos, and R. Garcia, *Molecular and nanoscale compositional contrast of soft matter in liquid: Interplay between elastic and dissipative interactions*, ACS Nano **6** (2012), no. 6, 4663–4670.

[81] A. M. Baró and R. G. Reifenberger, *Atomic force microscopy in liquid: biological applications*, John Wiley & Sons, 2012.

[82] P. K. Hansma, J. P. Cleveland, M. Radmacher, D. A. Walters, P. E. Hillner, M. Bezanilla, M. Fritz, D. Vie, H. G. Hansma, C. B. Prater, J. Massie, L. Fukunaga, J. Gurley, and V. Elings, *Tapping mode atomic force microscopy in liquids*, Applied Physics Letters **64** (1994), no. 13, 1738–1740.

[83] C. A. Putman, K. O. Van Der Werf, B. G. De Grooth, N. F. Van Hulst, and J. Greve, *Tapping mode atomic force microscopy in liquid*, Applied Physics Letters **64** (1994), no. 18, 2454–2456.

[84] M. Salerno, J. R. Krenn, B. Lamprecht, G. Schider, H. Ditlbacher, N. Félidj, A. Leitner, and F. R. Aussenegg, *Plasmon polaritons in metal nanostructures: the optoelectronic route to nanotechnology*, Optoelectronics Review **3** (2002), 217–224.

[85] J. R. Krenn and J.-C. Weeber, *Surface plasmon polaritons in metal stripes and wires*, Philosophical Transactions of the Royal Society of London. Series A: Mathematical, Physical and Engineering Sciences **362** (2004), no. 1817, 739–756.

[86] A. D. Rakić, A. B. Djurišić, J. M. Elazar, and M. L. Majewski, *Optical properties of metallic films for vertical-cavity optoelectronic devices*, Applied optics **37** (1998), no. 22, 5271–5283.

[87] R. Hillenbrand and F. Keilmann, *Complex optical constants on a subwavelength scale*, Physical Review Letters **85** (2000), no. 14, 3029–3032.

[88] B. Knoll and F. Keilmann, *Enhanced dielectric contrast in scattering-type scanning near-field optical microscopy*, Optics communications **182** (2000), no. 4-6, 321–328.

[89] C. F. Bohren and D. R. Huffman, *Absorption and scattering of light by small particles*, John Wiley & Sons, 2008.

[90] A. Cvitkovic, N. Ocelic, and R. Hillenbrand, *Analytical model for quantitative prediction of material contrasts in scattering-type near-field optical microscopy*, Optics Express **15** (2007), no. 14, 8550.

[91] N. Ocelic, *Quantitative near-field phonon-polariton spectroscopy*, Ph.D. thesis, Technische Universität München, 2007.

[92] B. Hauer, A. P. Engelhardt, and T. Taubner, *Quasi-analytical model for scattering infrared near-field microscopy on layered systems*, Optics Express **20** (2012), no. 12, 13173.

[93] J. N. Walford, J. A. Porto, R. Carminati, J.-J. Greffet, P.-M. Adam, S. Hudlet, J.-L. Bijeon, A. Stashkevich, and P. Royer, *Influence of tip modulation on image formation in scanning near-field optical microscopy*, Journal of Applied Physics **89** (2001), no. 9, 5159–5169.

[94] R. Fikri, D. Barchiesi, F. H'Dhili, R. Bachelot, A. Vial, and P. Royer, *Modeling recent experiments of apertureless near-field optical microscopy using 2D finite element method*, Optics Communications **221** (2003), no. 1-3, 13–22.

[95] X. Chen, C. F. B. Lo, W. Zheng, H. Hu, Q. Dai, and M. Liu, *Rigorous numerical modeling of scattering-type scanning near-field optical microscopy and spectroscopy*, Applied Physics Letters **111** (2017), no. 22, 223110.

[96] N. Ocelic, A. Huber, and R. Hillenbrand, *Pseudoheterodyne detection for background-free near-field spectroscopy*, Applied Physics Letters **89** (2006), no. 10, 1–4.

[97] D. Gabor, *Microscopy by reconstructed wave-fronts*, Proceedings of the Royal Society of London. Series A. Mathematical and Physical Sciences **197** (1949), no. 1051, 454–487.

[98] P. Hariharan, *Basics of holography*, Cambridge university press, 2002.

[99] U. Schnars and W. Jüptner, *Direct recording of holograms by a CCD target and numerical reconstruction*, Appl. Opt. **33** (1994), no. 2, 179–181.

[100] T.-C. Poon, *Digital holography and three-dimensional display: Principles and Applications*, Springer Science & Business Media, 2006.

[101] T. Zhang and I. Yamaguchi, *Three-dimensional microscopy with phase-shifting digital holography*, Opt. Lett. **23** (1998), no. 15, 1221–1223.

[102] T.-C. Poon and T. Kim, *Optical image recognition of three-dimensional objects*, Appl. Opt. **38** (1999), no. 2, 370–381.

[103] B. Rappaz, P. Marquet, E. Cuche, Y. Emery, C. Depeursinge, and P. J. Magistretti, *Measurement of the integral refractive index and dynamic cell morphometry of living cells with digital holographic microscopy*, Opt. Express **13** (2005), no. 23, 9361–9373.

[104] C. J. Mann, L. Yu, C.-M. Lo, and M. K. Kim, *High-resolution quantitative phase-contrast microscopy by digital holography*, Opt. Express **13** (2005), no. 22, 8693–8698.

[105] M. Schnell, P. S. Carney, and R. Hillenbrand, *Synthetic optical holography for rapid nanoimaging*, Nature Communications **5** (2014), 1–10.

[106] E. A. Muller, B. Pollard, and M. B. Raschke, *Infrared chemical nano-imaging: Accessing structure, coupling, and dynamics on molecular length scales*, Journal of Physical Chemistry Letters **6** (2015), no. 7, 1275–1284.

[107] M. B. Raschke, L. Molina, T. Elsaesser, D. H. Kim, W. Knoll, and K. Hinrichs, *Apertureless near-field vibrational imaging of block-copolymer nanostructures with ultrahigh spatial resolution*, ChemPhysChem **6** (2005), no. 10, 2197–2203.

[108] F. Huth, *Nanoscale Infrared Near-Field Spectroscopy*, Ph.D. thesis, Euskal Herriko Unibertsitatea-Universidad del País Vasco, 2015.

[109] S. Amarie, T. Ganz, and F. Keilmann, *Mid-infrared near-field spectroscopy*, Optics Express **17** (2009), no. 24, 21794.

[110] S. Mastel, A. A. Govyadinov, T. V. De Oliveira, I. Amenabar, and R. Hillenbrand, *Nanoscale-resolved chemical identification of thin organic films using infrared near-field spectroscopy and standard Fourier transform infrared references*, Applied Physics Letters **106** (2015), no. 2, 1–6.

[111] F. J. Alfaro-Mozaz, P. Alonso-González, S. Vélez, I. Dolado, M. Autore, S. Mastel, F. Casanova, L. E. Hueso, P. Li, A. Y. Nikitin, and R. Hillenbrand, *Nanoimaging of resonating hyperbolic polaritons in linear boron nitride antennas*, Nature Communications **8** (2017).

[112] D. Virmani, A. Bylinkin, I. Dolado, E. Janzen, J. H. Edgar, and R. Hillenbrand, *Amplitude- and phase-resolved infrared nanoimaging and nanospectroscopy of polaritons in a liquid environment*, Nano Letters **21** (2021), no. 3, 1360–1367.

[113] J. Wood, *Large-scale growth, fluorination, clean transfer, and layering of graphene and related nanomaterials*, Ph.D. thesis, University of Illinois at Urbana-Champaign, 2014.

[114] G. Algara-Siller, O. Lehtinen, F. C. Wang, R. R. Nair, U. Kaiser, H. A. Wu, A. K. Geim, and I. V. Grigorieva, *Square ice in graphene nanocapillaries*, Nature **519** (2015), no. 7544, 443–445.

[115] M. Jin, F. Lu, and M. A. Belkin, *High-sensitivity infrared vibrational nanospectroscopy in water*, Light: Science & Applications **6** (2017), no. 7, e17096–e17096.

[116] G. Ramer, F. S. Ruggeri, A. Levin, T. P. Knowles, and A. Centrone, *Determination of Polypeptide Conformation with Nanoscale Resolution in Water*, ACS Nano **12** (2018), no. 7, 6612–6619.

[117] H. Wang, E. Janzen, L. Wang, J. H. Edgar, and X. G. Xu, *Probing mid-infrared phonon polaritons in the aqueous phase*, Nano Letters **20** (2020), no. 5, 3986–3991.

[118] H. Wang, J. M. González-Fialkowski, W. Li, Q. Xie, Y. Yu, and X. G. Xu, *Liquid-Phase Peak Force Infrared Microscopy for Chemical Nanoimaging and Spectroscopy*, Analytical Chemistry **93** (2021), no. 7, 3567–3575.

[119] E. Bonaccurso, F. Schönfeld, and H. J. Butt, *Electrostatic forces acting on tip and cantilever in atomic force microscopy*, Physical Review B - Condensed Matter and Materials Physics **74** (2006), no. 8, 1–8.

[120] J. E. Stern, B. D. Terris, H. J. Mamin, and D. Rugar, *Deposition and imaging of localized charge on insulator surfaces using a force microscope*, Applied Physics Letters **53** (1988), no. 26, 2717–2719.

[121] H. Liu, Y. Wang, and J. M. Bowman, *Quantum Local Monomer IR Spectrum of Liquid D2O at 300 K from 0 to 4000 cm-1 Is in Near-Quantitative Agreement with Experiment*, Journal of Physical Chemistry B **120** (2016), no. 10, 2824–2828.

[122] J. J. Max and C. Chapados, *Isotope effects in liquid water by infrared spectroscopy. III. H 2O and D2O spectra from 6000 to 0 cm-1*, Journal of Chemical Physics **131** (2009), no. 18.

[123] T. E. Schäffer, J. P. Cleveland, F. Ohnesorge, D. A. Walters, and P. K. Hansma, *Studies of vibrating atomic force microscope cantilevers in liquid*, Journal of Applied Physics **80** (1996), no. 7, 3622–3627.

[124] C. A. Putman, K. O. Van Der Werf, B. G. De Grooth, N. F. Van Hulst, and J. Greve, *Tapping mode atomic force microscopy in liquid*, Applied Physics Letters **64** (1994), no. 18, 2454–2456.

[125] G. Y. Chen, R. J. Warmack, T. Thundat, D. P. Allison, and A. Huang, *Resonance response of scanning force microscopy cantilevers*, Review of Scientific Instruments **65** (1994), no. 8, 2532–2537.

[126] J. Tamayo, *Energy dissipation in tapping-mode scanning force microscopy with low quality factors*, Applied Physics Letters **75** (1999), no. 22, 3569–3571.

[127] J. Tamayo, A. D. Humphris, R. J. Owen, and M. J. Miles, *High-Q dynamic force microscopy in liquid and its application to living cells*, Biophysical Journal **81** (2001), no. 1, 526–537.

[128] H. Hölscher and U. D. Schwarz, *Q-controlled amplitude modulation atomic force microscopy in liquids: An analysis*, Applied Physics Letters **89** (2006), no. 7, 22–25.

[129] W. Han, S. M. Lindsay, and T. Jing, *A magnetically driven oscillating probe microscope for operation in liquids*, Applied Physics Letters **69** (1996), no. 26, 4111–4113.

[130] M. Schnell, A. Garcia-Etxarri, A. J. Huber, K. B. Crozier, A. Borisov, J. Aizpurua, and R. Hillenbrand, *Amplitude- and phase-resolved near-field mapping of infrared antenna modes by transmission-mode scattering-type near-field microscopy*, Journal of Physical Chemistry C **114** (2010), no. 16, 7341–7345.

[131] O. J. Martin and C. Girard, *Controlling and tuning strong optical field gradients at a local probe microscope tip apex*, Applied Physics Letters **70** (1997), no. 6, 705–707.

[132] B. Knoll and F. Keilmann, *Mid-infrared scanning near-field optical microscope resolves 30 nm*, Journal of Microscopy **194** (1999), no. 2-3, 512–515.

[133] A. García-Etxarri, I. Romero, F. J. G. D. Abajo, R. Hillenbrand, and J. Aizpurua, *Influence of the tip in near-field imaging of nanoparticle plasmonic modes : Weak and strong coupling regimes*, **79** (2009), no. 12, 125439.

[134] F. Neubrech, A. Pucci, T. W. Cornelius, S. Karim, A. García-Etxarri, and J. Aizpurua, *Resonant plasmonic and vibrational coupling in a tailored nanoantenna for infrared detection*, Physical Review Letters **101** (2008), no. 15, 2–5.

[135] T. Neuman, P. Alonso-González, A. Garcia-Etxarri, M. Schnell, R. Hillenbrand, and J. Aizpurua, *Mapping the near fields of plasmonic nanoantennas by scattering-type scanning near-field optical microscopy*, Laser and Photonics Reviews **9** (2015), no. 6, 637–649.

[136] R. Adato and H. Altug, *In-situ ultra-sensitive infrared absorption spectroscopy of biomolecule interactions in real time with plasmonic nanoantennas*, Nature Communications **4** (2013).

[137] O. Limaj, D. Etezadi, N. J. Wittenberg, D. Rodrigo, D. Yoo, S. H. Oh, and H. Altug, *Infrared Plasmonic Biosensor for Real-Time and Label-Free Monitoring of Lipid Membranes*, Nano Letters **16** (2016), no. 2, 1502–1508.

[138] F. Neubrech, C. Huck, K. Weber, A. Pucci, and H. Giessen, *Surface-enhanced infrared spectroscopy using resonant nanoantennas*, Chemical Reviews **117** (2017), no. 7, 5110–5145.

[139] R. Blanchard, S. V. Boriskina, P. Genevet, M. A. Kats, J.-P. Tetienne, N. Yu, M. O. Scully, L. Dal Negro, and F. Capasso, *Multi-wavelength mid-infrared plasmonic antennas with single nanoscale focal point*, optics express **19** (2011), no. 22, 22113–22124.

[140] R. Esteban, R. Vogelgesang, J. Dorfmüller, A. Dmitriev, C. Rockstuhl, C. Etrich, and K. Kern, *Direct near-field optical imaging of higher order plasmonic resonances*, Nano letters **8** (2008), no. 10, 3155–3159.

[141] M. Rang, A. C. Jones, Z. Fei, Z. Y. Li, B. J. Wiley, X. Younan, and M. B. Raschke, *Optical Near-Field Mapping of Plasmonic Nanoprisms*, Nano Letters **8** (2008), no. 10, 3357–3363.

[142] J. Dorfmüller, R. Vogelgesang, R. T. Weitz, C. Rockstuhl, C. Etrich, T. Pertsch, F. Lederer, and K. Kern, *Fabry-Pérot Resonances in One-Dimensional Plasmonic*, Nano letters **9** (2009), no. 6, 2372–7.

[143] M. Paulite, Z. Fakhraai, I. T. Li, N. Gunari, A. E. Tanur, and G. C. Walker, *Imaging secondary structure of individual amyloid fibrils of a β2-microglobulin fragment using near-field infrared spectroscopy*, Journal of the American Chemical Society **133** (2011), no. 19, 7376–7383.

[144] A. R. Hind, S. K. Bhargava, and A. McKinnon, *At the solid/liquid interface: FTIR/ATR - The tool of choice*, Advances in Colloid and Interface Science **93** (2001), no. 1-3, 91–114.

[145] S. G. Kazarian and K. L. A. Chan, *Applications of ATR-FTIR spectroscopic imaging to biomedical samples*, Biochimica et Biophysica Acta - Biomembranes **1758** (2006), no. 7, 858–867.

[146] D. A. Woods and C. D. Bain, *Total internal reflection spectroscopy for studying soft matter*, Soft Matter **10** (2014), no. 8, 1071–1096.

[147] S. E. Glassford, B. Byrne, and S. G. Kazarian, *Recent applications of ATR FTIR spectroscopy and imaging to proteins*, Biochimica et Biophysica Acta - Proteins and Proteomics **1834** (2013), no. 12, 2849–2858.

[148] D. Axelrod, *Total Internal Reflection Fluorescence Microscopy*, Encyclopedia of Cell Biology: Volume 1-6, Second Edition **2** (2022), no. 2, 73–85.

[149] A. L. Mattheyses, S. M. Simon, and J. Z. Rappoport, *Imaging with total internal reflection fluorescence microscopy for the cell biologist*, Journal of Cell Science **123** (2010), no. 21, 3621–3628.

[150] R. Iwamoto, M. Miya, K. Ohta, and S. Mima, *Total internal reflection Raman spectroscopy*, The Journal of Chemical Physics **74** (1981), no. 9, 4780–4790.

[151] D. A. Woods and C. D. Bain, *Total internal reflection Raman spectroscopy*, Analyst **137** (2012), no. 1, 35–48.

[152] M. R. Querry, *Optical constants of minerals and other materials from the millimeter to the ultraviolet*, Chemical Research, Development & Engineering Center, US Army Armament Munitions Chemical Command, 1987.

[153] X. G. Xu, M. Rang, I. M. Craig, and M. B. Raschke, *Pushing the sample-size limit of infrared vibrational nanospectroscopy: From monolayer toward single molecule sensitivity*, Journal of Physical Chemistry Letters **3** (2012), no. 13, 1836–1841.

[154] S. Tsuda, S. Yamaguchi, Y. Kanamori, and H. Yugami, *Spectral and angular shaping of infrared radiation in a polymer resonator with molecular vibrational modes*, Optics Express **26** (2018), no. 6, 6899.

[155] B. H. Stuart, *Infrared spectroscopy: fundamentals and applications*, John Wiley & Sons, 2004.

[156] C. F. Wang, B. Kafle, T. E. Tesema, H. Kookhaee, and T. G. Habteyes, *Molecular Sensitivity of Near-Field Vibrational Infrared Imaging*, Journal of Physical Chemistry C **124** (2020), no. 38, 21018–21026.

[157] I. Niehues, L. Mester, E. Vicentini, D. Wigger, M. Schnell, and R. Hillenbrand, *Identification of weak molecular absorption in single-wavelength s-SNOM images*, Optics Express **31** (2023), no. 4, 7012.

[158] A. S. McLeod, A. Wieteska, G. Chiriaco, B. Foutty, Y. Wang, Y. Yuan, F. Xue, V. Gopalan, L. Q. Chen, Z. Q. Mao, A. J. Millis, A. N. Pasupathy, and D. N. Basov, *Nano-imaging of strain-tuned stripe textures in a Mott crystal*, npj Quantum Materials **6** (2021), no. 1.

[159] L. Mester, A. A. Govyadinov, and R. Hillenbrand, *High-fidelity nano-FTIR spectroscopy by on-pixel normalization of signal harmonics*, Nanophotonics **11** (2022), no. 2, 377–390.

[160] B. T. O'Callahan, M. Hentschel, M. B. Raschke, P. Z. El-Khoury, and A. S. Lea, *Ultrasensitive Tip- and Antenna-Enhanced Infrared Nanoscopy of Protein Complexes*, Journal of Physical Chemistry C **123** (2019), no. 28, 17505–17509.

[161] E. A. Muller, B. Pollard, H. A. Bechtel, R. Adato, D. Etezadi, H. Altug, and M. B. Raschke, *Nanoimaging and Control of Molecular Vibrations through Electromagnetically*

Induced Scattering Reaching the Strong Coupling Regime, ACS Photonics **5** (2018), no. 9, 3594–3600.

[162] D. Virmani, C. Maciel-Escudero, R. Hillenbrand, and M. Schnell, *Experimental verification of field-enhanced molecular vibrational scattering at single infrared antennas*, Nature Communications **15** (2024), no. 1, 6760.

[163] K. B. Crozier, A. Sundaramurthy, G. S. Kino, and C. F. Quate, *Optical antennas: Resonators for local field enhancement*, Journal of Applied Physics **94** (2003), no. 7, 4632–4642.

[164] P. Mühlschlegel, H. J. Eisler, O. J. Martin, B. Hecht, and D. W. Pohl, *Applied physics: Resonant optical antennas*, Science **308** (2005), no. 5728, 1607–1609.

[165] P. J. Schuck, D. P. Fromm, A. Sundaramurthy, G. S. Kino, and W. E. Moerner, *Improving the Mismatch between Light and Nanoscale Objects with Gold Bowtie Nanoantennas*, Phys. Rev. Lett. **94** (2005), no. 1, 17402.

[166] F. Neubrech, T. Kolb, R. Lovrincic, G. Fahsold, A. Pucci, J. Aizpurua, T. W. Cornelius, M. E. Toimil-Molares, R. Neumann, and S. Karim, *Resonances of individual metal nanowires in the infrared*, Applied Physics Letters **89** (2006), no. 25, 1–3.

[167] S. S. Aćimović, M. P. Kreuzer, M. U. González, and R. Quidant, *Plasmon near-field coupling in metal dimers as a step toward single-molecule sensing*, ACS Nano **3** (2009), no. 5, 1231–1237.

[168] N. Liu, M. L. Tang, M. Hentschel, H. Giessen, and A. P. Alivisatos, *Nanoantenna-enhanced gas sensing in a single tailored nanofocus*, Nature Materials **10** (2011), no. 8, 631–636.

[169] C. K. Chen, M. H. Chang, H. T. Wu, Y. C. Lee, and T. J. Yen, *Enhanced vibrational spectroscopy, intracellular refractive indexing for label-free biosensing and bioimaging by multiband plasmonic-antenna array*, Biosensors and Bioelectronics **60** (2014), 343–350.

[170] K. Weber, M. L. Nesterov, T. Weiss, M. Scherer, M. Hentschel, J. Vogt, C. Huck, W. Li, M. Dressel, H. Giessen, and F. Neubrech, *Wavelength scaling in antenna-enhanced infrared spectroscopy: Toward the far-IR and THz region*, ACS Photonics **4** (2017), no. 1, 45–51.

[171] E. Ozbay, *Plasmonics: Merging photonics and electronics at nanoscale dimensions*, Science **311** (2006), no. 5758, 189–193.

[172] J.-S. Huang, T. Feichtner, P. Biagioni, and B. Hecht, *Impedance Matching and Emission Properties of Nanoantennas in an Optical Nanocircuit*, Nano Letters **9** (2009), no. 5, 1897–1902.

[173] A. Alù and N. Engheta, *Wireless at the nanoscale: Optical interconnects using matched nanoantennas*, Physical Review Letters **104** (2010), no. 21, 1–4.

[174] L. Tang, S. E. Kocabas, S. Latif, A. K. Okyay, D. S. Ly-Gagnon, K. C. Saraswat, and D. A. Miller, *Nanometre-scale germanium photodetector enhanced by a near-infrared dipole antenna*, Nature Photonics **2** (2008), no. 4, 226–229.

[175] M. W. Knight, H. Sobhani, P. Nordlander, and N. J. Halas, *Photodetection with Active Optical Antennas*, Science **332** (2011), no. 6030, 702–704.

[176] Z. H. Kim and S. R. Leone, *Polarization-selective mapping of near-field intensity and phase around gold nanoparticles using apertureless near-field microscopy*, Optics Express **16** (2008), no. 3, 1733.

[177] R. L. Olmon, P. M. Krenz, A. C. Jones, G. D. Boreman, and M. B. Raschke, *Near-field imaging of optical antenna modes in the mid-infrared*, Optics Express **16** (2008), no. 25, 20295.

[178] T. Neuman, P. Alonso-González, A. Garcia-Etxarri, M. Schnell, R. Hillenbrand, and J. Aizpurua, *Mapping the near fields of plasmonic nanoantennas by scattering-type scanning near-field optical microscopy*, Laser and Photonics Reviews **9** (2015), no. 6, 637–649.

[179] P. B. Johnson and R. W. Christy, *Optical Constants of the Noble Metals*, Phys. Rev. B **6** (1972), no. 12, 4370–4379.

[180] G. M. Hale and M. R. Querry, *Optical Constants of Water in the 200-nm to 200-μm Wavelength Region*, Applied Optics **12** (1973), no. 3, 555.

[181] E. Palik, *Handbook of optical constants of solids*, Academic Press, 1985.

[182] I. Amenabar, S. Poly, M. Goikoetxea, W. Nuansing, P. Lasch, and R. Hillenbrand, *Hyperspectral infrared nanoimaging of organic samples based on Fourier transform infrared nanospectroscopy*, Nature Communications **8** (2017).

[183] G. Fornaro, G. Franceschetti, R. Lanari, and E. Sansosti, *Robust phase-unwrapping techniques: a comparison*, JOSA A **13** (1996), no. 12, 2355–2366.

[184] L. Novotny, *Effective wavelength scaling for optical antennas*, Physical Review Letters **98** (2007), no. 26, 1–4.

[185] J. Aizpurua, G. W. Bryant, L. J. Richter, F. J. García De Abajo, B. K. Kelley, and T. Mallouk, *Optical properties of coupled metallic nanorods for field-enhanced spectroscopy*, Physical Review B - Condensed Matter and Materials Physics **71** (2005), no. 23, 1–13.

[186] G. W. Bryant, F. J. García De Abajo, and J. Aizpurua, *Mapping the plasmon resonances of metallic nanoantennas*, Nano Letters **8** (2008), no. 2, 631–636.

[187] L. Kühner, M. Hentschel, U. Zschieschang, H. Klauk, J. Vogt, C. Huck, H. Giessen, and F. Neubrech, *Nanoantenna-Enhanced Infrared Spectroscopic Chemical Imaging*, ACS Sensors **2** (2017), no. 5, 655–662.

[188] F. Zhang, X. Tang, and L. Li, *Origins of Baseline Drift and Distortion in Fourier Transform Spectra*, Molecules **27** (2022), no. 13.

[189] W. L. Barnes, A. Dereux, and T. W. Ebbesen, *Surface plasmon subwavelength optics*, Nature **424** (2003), no. 6950, 824–830.

[190] B. Neuner, D. Korobkin, C. Fietz, D. Carole, G. Ferro, and G. Shvets, *Midinfrared index sensing of pL-scale analytes based on surface phonon polaritons in silicon carbide*, Journal of Physical Chemistry C **114** (2010), no. 16, 7489–7491.

[191] W. Ma, P. Alonso-González, S. Li, A. Y. Nikitin, J. Yuan, J. Martín-Sánchez, J. Taboada-Gutiérrez, I. Amenabar, P. Li, S. Vélez, C. Tollan, Z. Dai, Y. Zhang, S. Sriram, K. Kalantar-Zadeh, S. T. Lee, R. Hillenbrand, and Q. Bao, *In-plane anisotropic and ultra-low-loss polaritons in a natural van der Waals crystal*, Nature **562** (2018), no. 7728, 557–562.

[192] D. Rodrigo, O. Limaj, D. Janner, D. Etezadi, F. J. García De Abajo, V. Pruneri, and H. Altug, *Mid-infrared plasmonic biosensing with graphene*, Science **349** (2015), no. 6244, 165–168.

[193] A. Marini, I. Silveiro, and F. J. García De Abajo, *Molecular sensing with tunable graphene plasmons*, ACS Photonics **2** (2015), no. 7, 876–882.

[194] Y. Francescato, V. Giannini, J. Yang, M. Huang, and S. A. Maier, *Graphene sandwiches as a platform for broadband molecular spectroscopy*, ACS Photonics **1** (2014), no. 5, 437–443.

[195] M. Autore, P. Li, I. Dolado, F. J. Alfaro-Mozaz, R. Esteban, A. Atxabal, F. Casanova, L. E. Hueso, P. Alonso-González, J. Aizpurua, A. Y. Nikitin, S. Vélez, and R. Hillenbrand, *Boron nitride nanoresonators for Phonon-Enhanced molecular vibrational spectroscopy at the strong coupling limit*, Light: Science and Applications **7** (2018), no. 4, 17172–17178.

[196] J. Li, J. Pang, Z.-d. Yan, J. Jahng, J. Li, W. Morrison, J. Liang, Q.-Y. Zhang, and X.-H. Xia, *Antenna Enhanced Infrared Photoinduced Force Imaging in Aqueous Environment with Super-Resolution and Hypersensitivity*, CCS Chemistry **4** (2022), no. 8, 2738–2747.

[197] T. Q. Vuong, S. Liu, A. Van Der Lee, R. Cuscó, L. Artús, T. Michel, P. Valvin, J. H. Edgar, G. Cassabois, and B. Gil, *Isotope engineering of van der Waals interactions in hexagonal boron nitride*, Nature Materials **17** (2018), no. 2, 152–158.

[198] S. Liu, R. He, L. Xue, J. Li, B. Liu, and J. H. Edgar, *Single Crystal Growth of Millimeter-Sized Monoisotopic Hexagonal Boron Nitride*, Chemistry of Materials **30** (2018), no. 18, 6222–6225.

[199] J. Li, C. Elias, G. Ye, D. Evans, S. Liu, R. He, G. Cassabois, B. Gil, P. Valvin, B. Liu, and J. H. Edgar, *Single crystal growth of monoisotopic hexagonal boron nitride from a Fe-Cr flux*, Journal of Materials Chemistry C **8** (2020), no. 29, 9931–9935.

[200] Z. Shi, H. A. Bechtel, S. Berweger, Y. Sun, B. Zeng, C. Jin, H. Chang, M. C. Martin, M. B. Raschke, and F. Wang, *Amplitude- and phase-resolved nanospectral imaging of phonon polaritons in hexagonal boron nitride*, ACS Photonics **2** (2015), no. 7, 790–796.

[201] A. Fali, S. T. White, T. G. Folland, M. He, N. A. Aghamiri, S. Liu, J. H. Edgar, J. D. Caldwell, R. F. Haglund, and Y. Abate, *Refractive index-based control of hyperbolic phonon-polariton propagation*, Nano Letters **19** (2019), no. 11, 7725–7734.

[202] K. S. Kim, D. Trajanoski, K. Ho, L. Gilburd, A. Maiti, L. Van Der Velden, S. De Beer, and G. C. Walker, *The effect of adjacent materials on the propagation of phonon polaritons in hexagonal boron nitride*, Journal of Physical Chemistry Letters **8** (2017), no. 13, 2902–2908.

[203] D. S. Dovzhenko, S. V. Ryabchuk, Y. P. Rakovich, and I. R. Nabiev, *Light-matter interaction in the strong coupling regime: Configurations, conditions, and applications*, Nanoscale **10** (2018), no. 8, 3589–3605.

[204] J. Flick, N. Rivera, and P. Narang, *Strong light-matter coupling in quantum chemistry and quantum photonics*, Nanophotonics **7** (2018), no. 9, 1479–1501.

[205] A. Thomas, L. Lethuillier-Karl, K. Nagarajan, R. M. Vergauwe, J. George, T. Chervy, A. Shalabney, E. Devaux, C. Genet, J. Moran, and T. W. Ebbesen, *Tilting a ground-state reactivity landscape by vibrational strong coupling*, Science **363** (2019), no. 6427, 615–619.

[206] J. A. Hutchison, T. Schwartz, C. Genet, E. Devaux, and T. W. Ebbesen, *Modifying chemical landscapes by coupling to vacuum fields*, Angewandte Chemie International Edition **51** (2012), no. 7, 1592–1596.

[207] A. Bylinkin, M. Schnell, M. Autore, F. Calavalle, P. Li, J. Taboada-Gutièrrez, S. Liu, J. H. Edgar, F. Casanova, L. E. Hueso, P. Alonso-Gonzalez, A. Y. Nikitin, and R. Hillenbrand, *Real-space observation of vibrational strong coupling between propagating phonon polaritons and organic molecules*, Nature Photonics **15** (2021), no. 3, 197–202.

[208] T. Glaser, S. Beck, B. Lunkenheimer, D. Donhauser, A. Köhn, M. Kröger, and A. Pucci, *Infrared study of the MoO3 doping efficiency in 4,4′-bis(N-carbazolyl)-1,1′-biphenyl (CBP)*, Organic Electronics **14** (2013), no. 2, 575–583.

[209] R. García, *Amplitude modulation atomic force microscopy*, John Wiley & Sons, 2011.

[210] Y.-s. Lo, N. D. Huefner, W. S. Chan, P. Dryden, B. Hagenhoff, and T. P. Beebe, *Organic and Inorganic Contamination on Commercial AFM Cantilevers*, Langmuir **15** (1999), no. 19, 6522–6526.

[211] L. Sirghi, O. Kylián, D. Gilliland, G. Ceccone, and F. Rossi, *Cleaning and hydrophilization of atomic force microscopy silicon probes*, Journal of Physical Chemistry B **110** (2006), no. 51, 25975–25981.

[212] N. C. Passler and A. Paarmann, *Generalized 4*4 matrix formalism for light propagation in anisotropic stratified media: study of surface phonon polaritons in polar dielectric heterostructures*, Journal of the Optical Society of America B **34** (2017), no. 10, 2128.

[213] A. J. Giles, S. Dai, I. Vurgaftman, T. Hoffman, S. Liu, L. Lindsay, C. T. Ellis, N. Assefa, I. Chatzakis, T. L. Reinecke, J. G. Tischler, M. M. Fogler, J. H. Edgar, D. N. Basov, and J. D. Caldwell, *Ultralow-loss polaritons in isotopically pure boron nitride*, Nature Materials **17** (2018), no. 2, 134–139.

[214] T. L. Myers, R. G. Tonkyn, T. O. Danby, M. S. Taubman, B. E. Bernacki, J. C. Birnbaum, S. W. Sharpe, and T. J. Johnson, *Accurate measurement of the optical constants n and k for a series of 57 inorganic and organic liquids for optical modeling and detection*, Appl. Spectrosc. **72** (2018), no. 4, 535–550.

[215] R. E. Glover and M. Tinkham, *Conductivity of superconducting films for photon energies between 0.3 and 40kTc*, Physical Review **108** (1957), no. 2, 243–256.

List of publications

This thesis is based on the following publications:

1. Divya Virmani, Andrei Bylinkin, Irene Dolado, Eli Janzen, James H. Edgar, and Rainer Hillenbrand. *Amplitude-and Phase-Resolved Infrared Nanoimaging and Nanospectroscopy of Polaritons in a Liquid Environment.* Nano Letters **21**(3), 1360-1367(2021).
2. Divya Virmani, Carlos Maciel-Escudero, Rainer Hillenbrand, and Martin Schnell. *Experimental verification of field-enhanced molecular vibrational scattering at single infrared antennas.* Nature Communications **15**(1), 6760(2024).

Acknowledgments

I want to express my gratitude towards my supervisor Prof. Rainer Hillenbrand, group leader of the nano-optics group at CIC nanoGUNE BRTA, for giving me the opportunity to join his group, for always being open for discussions and for his support and patience throughout my PhD.

I would like to thank all the present and past members of the nano-optics group at CIC nanoGUNE, for providing me with a great atmosphere, scientific and non-scientific discussions, collaborations and support. In particular, I would like to thank Martin Schnell for his support with the transflection nano-FTIR setup, Irene Dolado for help in making many samples over the course of my research, Andrei Bylinkin for helping out with the calculations and always motivating me, and Alexander A. Govyadinov for all the discussions regarding the liquid cell and the bottom illumination s-SNOM. I would like to specially thank Carlos Crespo, for providing constant support in the lab during the instrumentation process. I would like to specially thank Monika Goikoetxea (CIC nanoGUNE) for her continuous support and help in both the scientific and administrative aspect of the research. I would also like to thank Stefan Mastel and Iban Amenabar for introducing me to the nano-optics labs, and Lars Mester for the coffee breaks.

I am thankful to Prof. Txema Pitarke, director of CIC nanoGUNE BRTA, for giving me the opportunity to conduct my research work in the Basque country at CIC nanoGUNE BRTA. I would also like to express my gratitude towards Miguel Odriozola Braconier for his constant support with residence permit requests and walking me through most of the administrative processes. I would also like to take this opportunity to thank all the employees specially fellow PhD's at nanoGUNE for creating a great working environment. I am also thankful to Angel Alegría Loinaz for his support with the thesis submission process.

I would like to acknowledge Neaspec GmbH (Haar, Germany) for supporting the development of the transflection beam path and liquid cell, Keysight Technologies GmbH (Linz, Austria), particularly Ivan Alić, for helping with the improvement of the refilling mechanism of the liquid cell.

I also want to thank all the collaborators and members of the SPM2.0 network for many scientific discussions and collaborations, for hosting me at their institutes and for the after meeting get together.

I further thank everyone involved in our interdisciplinary Tuesday, Thursday or Friday PhD reunions. Special thanks goes to my family especially my parents (Satpal and Veena Virmani) and my brother (Dheeraj Virmani) and friends for their continuous support. Special thanks to Heino Soo for always being there for me and Johan Briones for helping me with the Spanish summary.

This work has received funding from the European Union's Horizon 2020 research and innovation program under the Marie Skłodowska Curie grant agreement no. 721874 (SPM2.0). The authors further acknowledge financial support from the Spanish Ministry of Science, Innovation, and Universities (national project RTI2018-094830-B-100 and the project MDM-2016- 0618 of the Marie de Maeztu Units of Excellence Program), and the Basque Government (grant no. IT1164-19).